INFRARED INDUCED DYNAMICS OF LOOSELY BOUND MOLECULES

The dynamical process of vibrational state to continuum coupling for trans-1, 2-dichloroethylene (DCE) using infrared spectroscopy

MASTER OF SCIENCE

in

Physics

at

Massey University, [Albany], New Zealand.

by

Fatimah N. Alrsheedi

Supervisor:

Associate Professor John A. Harrison

5th July 2019

Massey University

Master of Science (Physics)

July 5, 2019

ACKNOWLEDGEMENTS

First, I would like to thank God for his graces and for helping me and giving me the strength to complete this work.

I would like to express my sincere gratitude to my supervisor Dr John Harrison for his patience, immense knowledge, feedback, guidance and support during the learning process of my thesis in spite of his many other academic and professional responsibilities. He provided me with the tools needed to choose the right path and complete my thesis successfully.

Along with my supervisor, I would also like to thank everyone who contributed in completing this thesis in some way. I am grateful to my professors who taught me at Massey University: Dr Fu-Guang Cao, Pro Tony Signal, Dr Patrick Bowman, Dr Elke Pahl and Dr Alona Ben-Tal. I am indebted to my colleague Erin Moffet for her very valuable assistance, thank you so much. Additionally, I am profoundly grateful to Saudi Arabia Government and The Custodian of The Two Holy Mosques' Overseas Scholarship Program for their invaluable help throughout my studies in New Zealand.

No one was more important to me in pursuing this project than my family members. I wish to express my deep gratitude to my father, my husband, my sisters, my brothers and my daughter Lama who have given their time to support and encourage me.

Finally, I dedicate this work to the spirit of my mother, who passed away last year, who spared no effort to educate and guide me. I would like to say her: "You give me

everything in life, you bore me, raised me, supported me, educated me and loved me. I am very proud to dedicate this work for your pure soul, and I did it for you".

Fatimah Naef Alrsheedi.

Contents

Figures

Tables

Abstract

The infrared absorption spectrum of crystalline trans-1, 2-dichloroethylene has been measured down to 50 K using a specially designed and constructed infrared (IR) cell, using a Nicolet iS50R FT-IR. The IR scans show the absorbance of trans-1, 2-dichloroethylene molecules at b_u CH stretch (ν_9), b_u CH bend (ν_{10}), a_u CH bend (ν_6) and b_u CCl stretch (ν_{11}) are changed at different temperature conditions. In the solid phase, the absorption spectra of crystalline trans -1, 2-dichloroethylene at different temperatures demonstrates a dramatic change in some of the peak shapes for b_u CH stretch (ν_9), b_u CH bend (ν_{10}), a_u CH bend (ν_6) and b_u CCl stretch (ν_{11}). Instead of a symmetric lineshape that would generally be expected for the excitations of these modes, the spectra clearly showed asymmetric lineshape in some of the peaks as result of the presence of Fano resonance which is not commonly seen in infrared spectroscopy. Although asymmetric peaks are often attributed to interference from reflected rays due to refractive index changes at boundary surfaces the observation, in some cases, of complete peak inversion allows for an unambiguous identification of Fano interference as the source of the asymmetry. The origin of this effect refers to quantum interference on the optical absorption through the coupling between the discrete and continuum states in which the excited eigenstates are mixtures of the discrete and continuum states, as the excitation of trans -1, 2-dichloroethylene occurring simultaneously with the continuum background transitions. In this thesis, we report IR spectroscopic observations that show interference between the vibrational states of the molecules of trans -1, 2-dichloroethylene with the continuum background states. The background continuum arises from the overlapping of many other resonances due to the overtone/ combination bands and coupling of other vibrational states, including the bulk optical phonons, providing essentially a broad continuum. Individual resonances are conspicuous at low temperature and continuously reduce with increasing temperature. Additionally, the IR bands for the

fundamental modes have been observed and discussed in this work. Further, the overtone and combination bands are also assigned on the basis of (gas phase) anharmonic calculations as the analysis of anharmonic and harmonic frequencies shows that the anharmonic frequencies are close and correspond better with the experiment than those acquired using a harmonic approximation.

Chapter 1: Introduction

The aim of this thesis is to investigate the dynamic process of vibrational coupling to produce a continuum for trans-1, 2-dichloroethylene (tDCE) using infrared spectroscopy. This is will be measured in a specially designed and constructed cell, using Nicolet iS50R FT-IR.

"The spectroscopy of light absorption is an essential tool for uncovering the microscopic structure of a material. The observed spectral line positions reveal the energy levels of the excited quantum states, whereas the lineshapes are determined by how the material relaxes after light is absorbed" (Lin & Chu, 2013, p. 694).

The concept of resonance due to wave interference is fundamental to physics, and its observed effects are very important for experimental investigations. In this experiment, we found resonance and anti-resonance lineshapes, which corresponded to reduced absorption in the tDCE system (Li et al., 2012). Instead of the symmetrical lineshape that would be expected for the excitations of these modes, the spectra clearly presented an asymmetrical lineshape. They were particularly evident in the infrared spectra around 3090 and 1200 cm^{-1}, which corresponded to the CH stretch and CH bend (ν_9 and ν_{10} modes, respectively) of tDCE.

Quantum mechanics causes an asymmetrical lineshape originating from the so-called configuration interaction due to the interference of the excitation of a discrete state with an underlying background continuum of states. Lineshapes related to such interference-based excitations have been described by the Fano profile, named after Ugo Fano, who provided a theoretical understanding of the origins of this resonance (Bianconi, 2003). Fano (1961) showed that resonance profiles with characteristic asymmetrical lineshapes can generally be described using the following equation:

$$(\varepsilon + q)^2 / (\varepsilon^2 + 1) \quad (1)$$

Where the reduced energy defined by E_r, the peak position, and Γ, the width of the resonance, is as follows:

$$\varepsilon = (E - E_r) / \Gamma/2 \quad (2)$$

These resonances exist in the transmissions of two barrier heterostructures due to wave interference in different channels. As Joe, Satanin, and Kim (2006, p. 295) stated, “So now it is clear that Fano interference is a worldwide phenomenon, because the interference does not depend on the matter and the equations–why are Fano interference phenomena so interesting in different topics of physics?” According to Katsumoto (2007), Fano treated the scattering problem associated with the incident wave as coherently scattered through the localised state with finite coupling to the continuum. To extract the effect of resonance between a localised state ϕ and those of the continuum $\varphi(E)$ with new energy E, Fano wrote the Hamiltonian for hybrid systems, which is defined as follows:

$$\langle\phi|H|\phi\rangle = E_0, \langle\varphi(E)|H|\varphi(E)\rangle = E, \ \langle\varphi(E)|H|\phi\rangle = V_E \quad (3)$$

The hybridised states of the new energy with new coefficients were as follows:

$$\psi(\epsilon) = a(\epsilon)\phi + \int \mathrm{d}E \, b(\epsilon, E)\varphi(E) \quad (4)$$

Further, $b(\epsilon, E)$ was correctly presented as follows:

$$b(\epsilon, E) = \left[\mathrm{P}\frac{1}{\epsilon - E} + z(\epsilon)\delta(\epsilon - E)\right] V_E a(\epsilon) \quad (5)$$

Generally, in scattering problems, $z = i\pi$, but here, it can be real as long as time reversal symmetry and it is represented as follows:

$$z(\epsilon) = \frac{1}{|V_\epsilon|^2}\left[\epsilon - E_0 - \mathrm{P}\int \mathrm{d}E \, \frac{|V_E|^2}{\epsilon - E}\right] = -\frac{\pi}{\tan\Delta\theta}, \quad (6)$$

As a result of the phase shift due to coupling, the transition to the external state can be written as follows:

$$\langle\psi_\epsilon|T|\xi_i\rangle = \frac{1}{\pi V_\epsilon^*}\,\langle\Phi|T|\xi_i\rangle\,\sin\Delta\theta - \,\langle\psi_\epsilon|T|\xi_i\rangle\,\cos\Delta\theta \qquad (7)$$

Where the localised state modified by the coupling to the continuum of states can be indicated as follows:

$$\Phi = \phi + P\int dE\,\frac{V_\epsilon\varphi(E)}{\epsilon - E} \qquad (8)$$

The probability of a transition to an unperturbed continuum can be written as follows:

$$F(\epsilon') \propto \frac{(\epsilon' - q)^2}{\epsilon'^2 + 1} \qquad (9)$$

Further, the energy is shifted and renormalised as follows:

$$\epsilon' = -\cos\Delta\theta = \frac{2}{\Gamma}\left[\epsilon - E_o - \mathrm{P}\int dE\,\frac{|V_E|^2}{\epsilon' - E}\right] \qquad (10)$$

Where, the width of the localised state is as follows:

$$\Gamma = \pi|V_{\epsilon'}|^2 \qquad (11)$$

The Fano parameter, *q*, is defined as follows:

$$q = \frac{\langle\Phi|T|\varphi_i\rangle}{\pi\, V_{\epsilon'}\,\langle\psi_{\epsilon'}|T|\varphi_i\rangle} \qquad (12)$$

Figure 1 : Energy dependence of the cross section demonstrating lineshapes originating from Fano interference with various *q* values. From (Misochko et al., 2015)

Fano introduced the asymmetry parameter, *q*, as a ratio of the probabilities of transition to the mixed state and the continuum (Miroshnichenko, Flach, & Kivshar, 2010).

$$\frac{1}{2}\pi q^2 = |(\Phi|T|i)|^2 \,/\, |(\psi_E|T|i)|^2\Gamma \qquad (13)$$

This parameter is very important and has great experimental implications, as it defines how experimental data fits the Fano profile (Liang Huang, Lai, Luo, & Grebogi, 2015). In the limit $q \to \infty$, the transition to the continuum is very weak, and the lineshape can be described by the normal Lorentzian profile of a Breit-Wigner resonance. This situation is determined exclusively by the transition through the discrete state. When the asymmetry parameter $q = 1$, both the continuum and discrete transitions are of the same strength, resulting in an asymmetrical profile and leading to a symmetrical dip, as the resonance lineshape for the zero

asymmetry parameter $q = 0$, as shown in Figure 1 (Miroshnichenko et al., 2010). Despite its intense sensitivity for the shifting of both geometry and environment modifications, which is the foundation of effective sensors, this makes a theoretical understanding of Fano-based systems more challenging (Zangeneh-Nejad & Fleury, 2019).

The asymmetrical lineshapes displayed in some spectra are commonly encountered in Raman scattering due to Stokes and anti-Stokes excitations. They are also seen in molecular spectroscopy and the infrared absorption reflection. In optical absorption experiments with noble gases, they generally arise due to the excitation of the optically bright discrete state coupling with a dark continuum of states (Meierott, Hotz, Néel, & Kröger, 2016)

Recently, Fano resonance has attracted much attention due to the development of photonics, which deals with matters that have multiple resonances. For example, under the weak coupling rule, Fano resonance occurs due to coupling between two different oscillators with very different damping rates, which lead to narrow and broad spectra lines. However, in a strong-coupling regime, oscillators exchange their energy much faster than they lose it, causing two coupled eigenmodes to form, the frequencies of which split from those of non-interacting oscillators (Limonov, Rybin, Poddubny, & Kivshar, 2017). Babić & de Dood (2010) suggested that the resonant coupling of light to leaky modes of a photonic crystal slab leads to the presence of Fano lineshapes. They also appear in different applications. In few-layer graphene, Fano resonance occurs due to coupling within the discrete state, as phonons vibrate and electrons transition via continuum states (Li et al., 2012). Details of the Fano parameter (q), as a reversal of Fano lineshape asymmetry, have been connected to the ability to tune an interaction, and therefore, the coherence between two channels, bringing the Fano parameter to its most basic form, in which the quantum interference of two alternative excitation path ways occurs (Meierott, Hotz, Néel, & Kröger, 2016; Babić & de Dood, 2010).

There have been no previously reported observations of Fano profiles in molecular IR absorption spectra arising from interactions between molecular vibrations and continuum transitions in molecular crystals. In this study, we have provided evidence for interference between the vibrational states of tDCE and background continuum transitions. The continuum arose due to resonances for overtone/combination bands and coupling between other vibrational states, including with optical phonons. It also arose due to combinations of delocalised vibrations, where molecular inversion symmetry was broken. These were particularly apparent in Fano lineshapes for the b_u CH stretch (ν_9) and b_u CH bend for crystalline tDCE. The intensity of the a_u CH bend (ν_6) and b_u CCl stretch (ν_{11}) also demonstrated complex lineshapes, but analysis of these peaks was difficult. This was due to a large baseline drift caused by the temperature dependent absorption of window materials near their transmission cut-offs at low frequencies, particularly at low temperatures. Asymmetry in the underlying continuum shape became noticeable at low temperatures, and peak heights continually decreased with increasing temperature to around the melting point due to the loss of sample through IR heating. Measurements were made using a specially designed and constructed cell to ensure the sample was under equilibrium temperature and pressure. This was located in the sample chamber of a Nicolet iS50R FT-IR.

This thesis has been organised as follows. In Chapter 2, details of the experimental procedures have been described, including the method of absorption spectroscopy (IR) and information about tDCE vibrational modes. Details of the experiment have been given in Chapter 3. In Chapter 4, results have been discussed and analysed, including their fit with the Fano profile, and simulated spectra for tDCE absorption have been explored. In addition, Argon matrix isolated DCE molecules have been examined. Results have been summarised in Chapter 5.

Chapter 2: Infrared Cell Design

The cell was constructed from a solid copper block (7.5mm x 6.8mm x 4.5mm) with three windows; two of them parallel for IR and UV analysis with path length 0.65 cm and the other at the front to allow the fluorescence analysis. The barium fluoride windows had a thickness of 6 mm and diameter of 25mm and were fastened by a copper retaining ring and six hex stainless steel screws with spring washers. The third window also had a diameter of 25mm and thickness of six millimetres but was made of quartz. All windows were sealed onto the copper block using indium foil gaskets and a thin Teflon gasket was placed outside the window before the compression flange to help prevent the windows from cracking because of being unevenly stressed. The spring washers were necessary to compensate for the difference in thermal contraction between the copper and stainless screws. The cry cooler CH-204-N coldhead was attached to a HC-4E1 compressor (Sumitomo Heavy Industries Inc.), which was attached to the copper cell block by three stainless steel hex screws and using Apiezon N high vacuum grease between the two pieces of copper to provide good thermal conductivity. The gas lines were connected to the cell by 1/8” stainless steel Swagelok tube and 1/8” male National Pipe Thread (NPT) to 1/8” Swagelok adapter. Additionally, the Lake Shore 325 temperature controller was used with a 2W heating rod fixed in the centre of the copper heat transfer rod and the temperature was checked using a thermal sensor DT-670-BO silicon diode connected to the top front corner of cell.

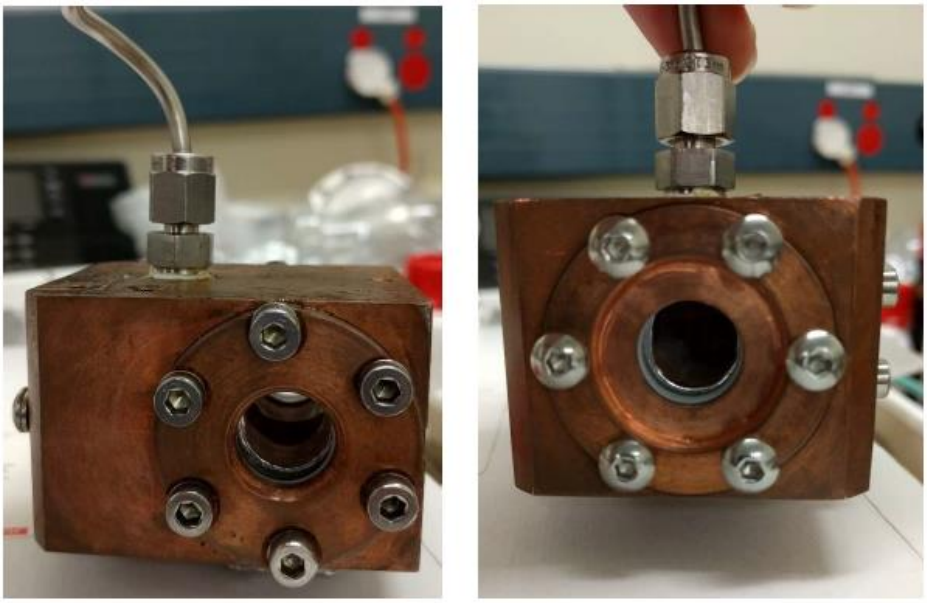

Figure 2 : Photo of side view of IR cell and in the right photo of the front view of IR cell viewing third window to allow for fluorescence

For the high pressure, the cell was monitored with a 3000 psi MKS baratron (750C33PCE2GA) and MKS PDR2000 Dual Capacitance Manometer readout. For the low pressure, a 1000 torr MKS baratron (622A13TBE) was used with a multifunctional long gauge controller Model 1GC100 by Stanford Research System.

Figure 3 : Photo of the top view of cell showing three connection points to connect to cryo-cooler and the 1/8” gas inlet tube

The entire cell was enclosed in an aluminium vacuum casing with eight external window options. For this analysis, the external barium fluoride of 25mm diameter by 2 mm windows was used. The windows are sealed onto the vacuum housing using O-ring seals. The casing is attached to the main cooler vacuum system using a NW160 O-ring that allowed the casing to be rotated under vacuum. External vacuum was created by a Edwards RV5 backing oil pump and a Oerlikon Leybold vacuum turbo drive TD400 turbo pump controlled by a Leybold Turbo control 300. The backing pressure was monitored using an Edward’s PRM10 pirani gauge and Edwards’s controller 1101 Iong with an Ion gauge controlled by a Leybold-Heraeus IONVAC IM 210.

The cell arrangement was connected to a rolling frame to allow the movement of the cell to either be pushed into the Nicolet iS50R FT-IR or pulled out and twisted to the side to access the unit away from the instruments. The Thermo-Fisher Nicolet iS50R FT-IR was equipped with a liquid nitrogen cooled mercury cadmium telluride detector (MCT). The wavelength range of the spectrum with low energy was limited by the BaF2 windows of the

cell and the vacuum housing at around 800 cm^{-1} and the high energy of the spectrum to detector limited at 7000 cm^{-1}.

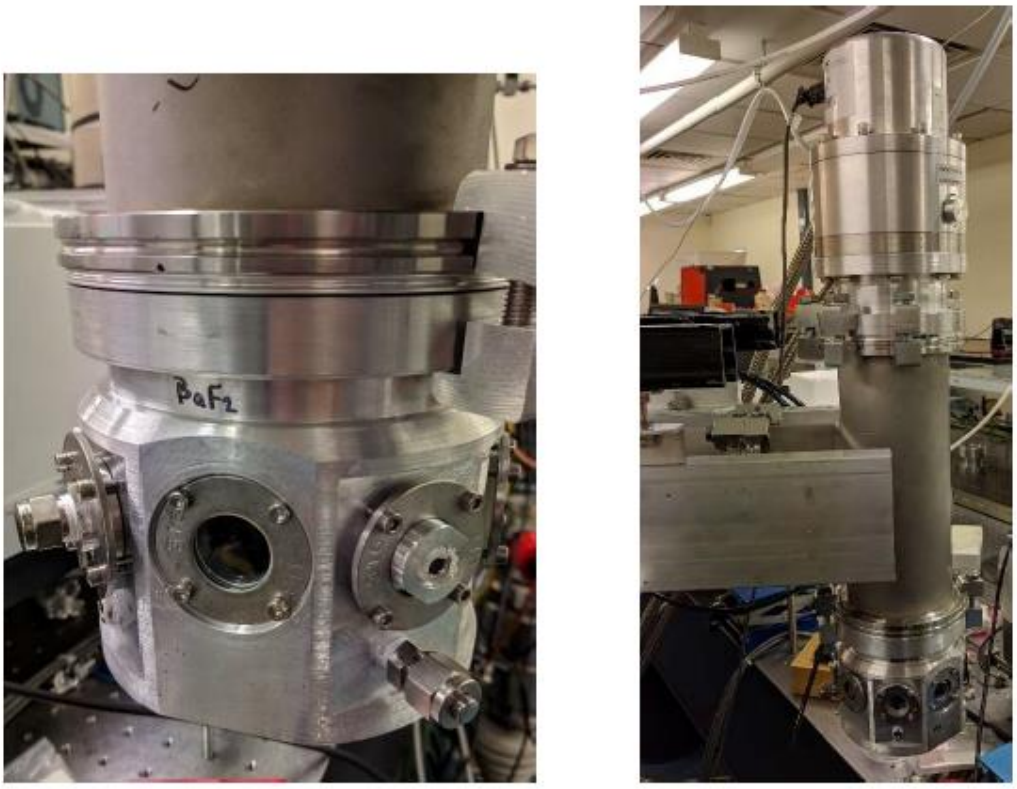

Figure 4 : left, photograph of the external vacuum casing showing one of the external windows. Right, photograph of cryo-cooler attached to the external window casing.

2.1. IR theory

Investigation of dynamic processes using methods based on infrared spectroscopy (IR), especially fingerprint spectra, can provide knowledge for understanding absorbance and transmitted spectra associated with its molecular structure (Huang et al., 2017). There are various ways to collect information on molecular structure and on the interaction of molecules with their surroundings using specttroscopy; these can be derived by the absorption or emission of electromagnetic radiation interacting with matter (Demtröder, 2013).

In spectroscopy, the advantage of the symmetry of the molecule refer to the first principles of energy levels calculation of the system and define which transitions are forbidden and which are allowed (Sathyanarayana, 2015) Fourier transform infrared spectrometer is a technique based on the determination of interaction between matter and electromagnetic field in the IR region At room temperature, when the molecules absorb IR radiation at different frequencies, the IR spectrum is dominated by the transitions occurring from the ground vibrational state $\nu = 0$ to an excited vibrational state $\nu = 1$; these are referred to as fundamental vibrations. For the molecules to be IR active, there must be a change in the dipole moment. The absorptions occur at resonant frequencies which are characteristic to the molecule's structure and are usually described as stretching, bending, rocking, scissoring, wagging and twisting vibrational modes.

As stated by Holmes (2016), for the vibrational motion of a molecule with quantized vibrational energy levels, the harmonic oscillator represent a good approximation with energy given by the following equation:

$$E_\nu\ (\ cm^{-1}) = \left(\nu + \frac{1}{2}\right)\omega_e \qquad (14)$$

However, the potential energy function of molecule large than R_e (internuclear separation) is no longer well described by a harmonic due to the molecule dissociates (ETH Zurich, n.d.). More accurate explanation of these vibrational energies is provided by anharmonic Morse oscillator with energy:

$$E_\nu\ (cm^{-1}) = \omega_e\left(\nu + \frac{1}{2}\right) - \omega_e x_e\left(\nu + \frac{1}{2}\right)^2 + \omega_e y_e\left(\nu + \frac{1}{2}\right)^2 + \ldots (15)$$

The potential energy function for Morse potential with its vibrational level as compared to those of a harmonic potential is shown in Figure 5. Because of the anharmonicity, this level converges with increasing quantum numbers and the higher

vibrational states deviate from their perfect shape and the overtones can occur. The most commonly occurring transitions are the fundamental transitions, $\nu=\pm1$, and the probability of overtones rapidly decreases with increasing $\nu=\pm n$. (Holmes, 2016).

Figure 5 : Comparison between vibrational eigenstates for both Morse and a harmonic potential. From (ETH Zurich, n.d.)

The overtones occur when a vibrational mode is excited from $\nu = 0$ to $\nu = 2$ which is called first overtone, and from $\nu = 0$ to $\nu = 3$ is called second overtone.

Some molecules have a significant population of the $\nu = 1$ state and transitions from this excited state are known as hot bands. Based on Boltzmann distribution law, ground state is highly populated at room temperature and KT corresponds to 200 cm^{-1} (Sathyanarayana, 2015). These transitions are temperature dependent with lower intensity at low temperature and become higher with increased temperature. This is one of the reasons of decreasing the energy level by increasing vibrational levels in anharmunic approximation. Generally, they take place at lower frequencies than the fundamentals.

Furthermore, if more than one vibration is excited by a photon absorbance, the combination bands can correspond, and the total energy of these bands is the product of the sum of individual transitions. They observed that two or more fundamental vibrations are excited simultaneously. One reason that combination bands might occur is that a fundamental vibration does not occur because of symmetry. When two vibrational bands have nearly the same energy and symmetry in both Raman and IR spectroscopies, it leads to splitting of these vibrations and that effect known as Fermi Resonance (Kondratyuk, 2005). They are usually formed by fundamental and overtone or fundamental vibration with a combination band. As a result of anharmonic oscillator approximation, the wavefunctions of these two resonant vibrations are mixed. Thus, a shift in these frequencies and changing in their spectrum intensity, followed by appearance of two strong bands instead of strong and weak bands (Sathyanarayana, 2015) indicates that if the symmetry are reached and then foundational mode and overtone or combination bands have same or similar energy, the coupling or the mixing occurs, and the overtone borrows the intensity from the foundational vibration. This increases the splitting of energy levels (Kondratyuk, 2005). When the width of these bands is non-negligible, Fermi resonance of localised levels cannot be applied, and the breadth of the spectrum can be produced by many alternatives, such as intermolecular interaction (hydrogen bounding molecules) and short lifetimes of the excited states or even the interaction between phonons and vibrational modes (Kondratyuk, 2005).

2.2. Trans-1, 2-dichloroethylene (DCE) vibrational modes

Before examining the dynamic coupling, processes associated with trans-1, 2-DCE vibrational modes, it is important to demonstrate the impact of the molecular symmetry on the vibrational spectra of trans-1, 2-DCE states.

The tDCE molecule is a non-linear molecule which has (3N-6) degrees of freedom. It contains six atoms as shown in Figure 6, and for gas phase trans-1, 2-DCE will be $3\times6-6=12$

normal modes of vibration with three additional degrees each for translational and rotational motion.

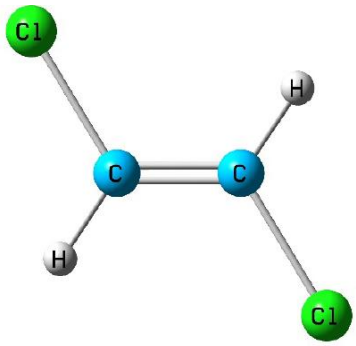

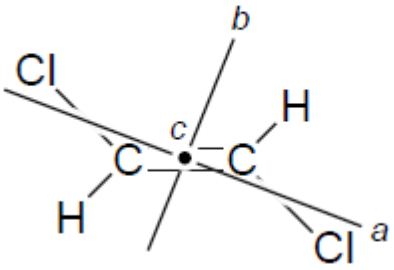

Figure 6 : The geometry of the isolated tDCE molecule from (L Huang et al., 2017).

Figure 7 : Structures of trans 1, 2-dichloroethyene and the approximate relationships of a, b and c rotation with the plane of the molecule, from (Craig & Lacuesta, 2004).

Trans-1, 2-DCE belongs to the C_{2h} symmetry group and contains four types of symmetry elements: the identity (E), 2-fold rotation axis (C_2), mirror plane through the plane of the molecule (σ_h) and inversion through the centre of symmetry (i) (Craig & Lacuesta, 2004). The locations of the principle rotational axes for tDCE structure is shown in the Figure 7 with axes a, b and c passing through its mass centre. An axis is for the least moment of inertia passing through the centre of the symmetry and is near the chlorine atoms. Similarly, b axis lies in the plane of the molecules, and c is the vertical axis to this plane. For gas-phase IR spectrum, the mode of a_u symmetry species that is antisymmetric to the plane (σ_h) and the center (i) elements, the band takes the c type that correspond to dipole moment accord along the c axis. The mode of b_u symmetry species will have the dipole mechanisms along a and b axes and thus be hybrids of sum A and B- type bands (Craig et al., 1998). Due to the hydrogen interactions and smaller B and C rotational constants that leads to increasing the positive charge for H and negative charge for Cl atom and decreasing the charge of C atom (Merkel et al., 2008).

Figure 8 Infrared energy levels: (Shimanouchi, 1972).

Figure 8 shows the infrared energies and corresponding state symmetries of molecular trans-1, 2-DCE and their IR intensities as (ia IR inactive, VS very strong, S strong, M medium and W weak). In order for a vibrational mode in a sample to be IR active, it must be associated with changes in the dipole moment. There are four strong or very strong infrared transitions of trans-1, 2-DCE in the gas phase from the b_u CH stretch (ν_9), b_u CH bend (ν_{10}), a_u CH bend (ν_6) and b_u CCl stretch (ν_{11}) and six actives in the Raman spectrum in the liquid

phase. The vibration frequencies for tDCE molecules are increased with both increasing of the bond strength and also with a decrease in the reduced mass so the lightest mass makes the important role for this contribution. The high frequencies are related to CH stretching which involves light hydrogen atoms. However, the double bond in C=C provides the stretching mode higher frequency despite involving heavy atoms. Though the CH bending is lower and has half the value as stretching modes, generally, bending out of plane is easier than in plane which has a low frequency because the atoms do not affect the exterior of the plane. Further, due to weak CCl bond and the added mass of chlorine atoms, the frequencies of stretching mode for CCl is low. However, due to the selection rules associated with having a centre version, the six modes that were inactive in the Raman are active in IR and vice versa. There are six infrared active absorptions and six which are not infrared active due to the absence of change in the dipole moments because individual bond dipole moments are equal in magnitude and opposite in direction; as a result, they cancel and there is no net dipole moment change. During symmetry breaking, a significant occurrence of 37 and 35 isotopes of chlorine no longer had a centre of inversion. Thus, all modes were allowed, but because the masses were almost the same as the intensities of other modes (Craig et al., 1998), ones that were forbidden for 37,37 and 35,35 isotopologues were low.

Chapter 3: The Experiment

In this experiment, trans-1, 2- DCE (tDCE) obtained from Sigma Aldrich, D62209 was introduced into the cell by the gas line system. The system cell and lines were pumped out to less than 5 mTorr to remove any contaminants by an Edwards E2M2 mechanical pump. The Nicolet iS50R FT-IR was purged with oxygen-free grade nitrogen gas (BOC) via an external nitrogen gas line fed from a cylinder to reduce the IR absorption from H_2O and CO_2 in the atmosphere at room temperature. Eight millilitres of the DCE sample were placed into a sample reservoir which was then cooled with liquid nitrogen. The frozen tDCE was then pumped on to remove any non-condensable gases before being warmed up to room temperature. The freeze pump thaw cycles were repeated three times. The sample was then distilled from the reservoir into the cryocell after the cell had been pre-cooled, generally to around 250 K. Scans were performed using 0.125 cm^{-1} resolution and a data spacing of 0.015 cm^{-1} with KBr beam splitter and mercury cadmium telluride detector (MCT) in the IR range 800-7000 cm^{-1}. The spectra were recorded with 64 scans for the atmosphere at room temperature and 32 scans for the empty cell at 250 K as the cell was cooled before adding the DCE to the system. All data collection and analysis were conducted using OMNIC software (version 9.7.43). The temperature was monitored by a Lakeview 325 temperature controller connected to a Lakeshore T-670 silicon diode sensor using a 4-wire connection scheme. The sensor was mounted on the external surface of the cryocell with thermal contact ensured by the addition of a layer of Apiezon ‘N’ grease between the sensor and the cell. The sensor was also covered with a small radiation shroud to prevent radiative heating from the room temperature vacuum case. The cryogenic wire led to the DT-670 where heat sank onto the external surface of the cryocell. Once the sample had been purified and the gas cell had reached the required temperature, the sample vessel was opened and the vapour of the tDCE was introduced to the cell through the gas line. The cell was then cooled down to 230 K and a

delay of 30 minutes was used to ensure all the DCE filled the cell and everything was at thermal equilibrium. The infrared scans indicated both the liquid and gas phases were present during this time. In this experiment, we used Argon (BOC, Zero grade with further purification through a Restek triple filter 22020). Around eight atmospheres of Argon were used to flush the DCE vapour into the cell; it also assisted to study the behaviour of the crystalline phase by reducing the amount of material lost from the windows from sublimation as a result of heating from the IR beam. The Argon pressure was monitored by an MKS PDR2000 Dual Capacitance Manometer readout and was slowly increased to eight atmospheres using a needle valve. The absorbance spectra of the crystalline tDCE was recorded as the sample was cooled. To record the general conditions, the initial spectrum was noted at 200 K and then 190 K, 180 K, 170 K, 160 K, 150 K, 140 K, 130 K and 120 K with Argon present and 117 K after the Argon had been pumped away. For high temperature, the cell was recorded as the sample was warmed by series of temperatures with 1–2 K spacing to around 223 K which was observed as the melting point for the crystalline tDCE at the used pressure. Further, the experiment was repeated under different conditions and the sample of DCE was able to undergo a phase change with either cooling or warming temperature cycles with the cell heater off or on. In one case, the cell was left cold overnight to allow slower formation of the DCE crystals. An additional spectrum was taken using matrix isolation in Argon at 20 K, which was used as a reference to compare isolated DCE in a condensed phase with calculated spectra and with the solid phase crystalline spectra.

3.1. Temperature dependence. The temperature dependence of the IR absorbance of the crystalline tDCE was measured. As the temperature was increased, the increase in the absorption from the underlying optical continuum over the whole frequency range was measured. The exact origin of the continuum is unclear, but it could be assumed that it is related to the coupling of optical phonon modes with local molecular modes of the DCE as

well as the delocalised molecular modes themselves. The optical phonon dynamics originated from the crystal modes involving translations of molecules in the unit cell (Dlott, 1986).

3.2. Low Temperature with no equilibrium. The absorbance spectra of the crystalline of tDCE were recorded with 16 scans at 0.125 cm-1 as the sample or the cell was cooled without the Argon bath gas present. The tDCE vapour was introduced into the cell at 230 K then cooled at the maximum rate to allow the formation of the sample on the window. The initial spectrum was at 214 K, which was then lowered with data measured at every 2 K or 3 K till 117 K. The spectra were collected over a finite temperature drop under non-equilibrium thermal conditions.

3.3. Low Temperature with thermal equilibrium. The absorbance spectra of crystalline tDCE were recorded from 800 cm^{-1}–7000 cm^{-1} as the cell was cooled. Argon bath gas was added as the tDCE vapour was introduced to the cell at 230 K then cooled down to allow the formation of the sample on the window. Data was collected from 200 K to 50 K in 10 K intervals between scans.

3.4. High Temperature. To record its behaviour at high temperature, crystalline tDCE was deposited on the window as the sample cooled to 180 K and then warmed the cell with a temperature interval of 1 K–2 K to around the melting point for the crystalline tDCE, which is around 223 K.

The spectra are dominated by four infrared transitions for tDCE at different temperatures: the peak for b_u CH stretch (ν_9), b_u CH bend (ν_{10}), a_u CH bend (ν_6) and b_u CCl stretch (ν_{11}), the assignments for which are shown in the next sections.

Chapter 4: Discussion and Analysis

4.1. Infrared spectra for Trans 1, 2-dichloroethylene

The experiment was repeated with various temperature intervals and rates of heating/cooling, and the conditions were varied to control the dynamic processes of the clusters of molecules and the influence of surface temperature on the continuum quantum state distribution due to structural changes. Due to the high vapour pressure of DCE, Argon was used to flush the DCE vapour in the gas line into the cell which assisted in depositing the DCE on the windows for studying the behaviour of the crystals that formed. Despite the Nicolet iS50R FT-IR being purged with nitrogen gas, it was not possible to reduce the water background sufficiently to remove all of the interferences in the strongest absorbing regions of water because there was little spectral overlap between the background gas absorptions and the DCE absorptions, which was not a limiting factor. This system was susceptible to small changes in the alignment of the cell which provided additional baseline drifts greater than that expected. Due to the contraction with the temperature of copper used in construction of both the coldhead and the cryocell and the background spectrum being collected with an empty room temperature cell, the spectrum at low temperatures clearly showed a drop in the baseline at 800 cm^{-1} to 900 cm^{-1} and change of the absorbance of the window materials near these energies.

The infrared scans showed clear peak shifts and transition through multiple physical states of the tDCE for the CH stretch and CH bend (Table 1) and the peak shapes, as expected, changed under different temperature conditions.

a_u	ν_6	CH bend	899.8 cm^{-1}
b_u	ν_9	CH stretch	3090 cm^{-1}
b_u	ν_{10}	CH bend	1200 cm^{-1}
b_u	ν_{11}	CCl stretch	828 cm^{-1}

Table 1: Infrared transitions for tDCE appear in IR scan.

In figures 9, 10, 11 and 12, the absorbance spectra of the tDCE were recorded as the sample was cooled and the tDCE was deposited by passing 1–2 atmospheres of Argon through the sample container by depositing the tDCE vapour on the cell windows.

An initial spectrum (Green in figures 9–12) was measured at 230 K without Argon, showing the mixture of liquid and gas in the cell as we can see in figures 9–12, which show the b_u CH stretch (ν_9), b_u CH bend (ν_{10}), a_u CH bend (ν_6) and b_u CCl stretch (ν_{11}) modes, respectively, as they change with temperature. Absorbance represents intensity of the associated peak due to bonding vibration of the covalent bonds, while the wavenumber value represents the infrared energy absorbed by bonds during analysis, the FTIR spectra correlate absorbance versus wavenumber cm^{-1}.

After warming the cell, from 216 K to 221 K, the pink scan showed the absorption spectra and the ro-vibrational transitions of the molecules were partially resolved particularly for the a_u CH bend (ν_6). The b_u CCl stretch (ν_{11}) is broad as the state distribution of the molecule of the DCE increased with increase in the temperature and the absorption of these molecules reduced with a decrease in temperature. Moroever, in the low frequency region the spectra were noisy not only because of the reduced transmittance of the cell due to the window materials but also because of the very intense CCl stretch absorption (as evident from the offscale absorptions). The background was collected with an empty cell and at room temperature though that led to a curved drop in the baseline approximately 800 cm^{-1} to 900 cm^{-1} at low temperatures due to the changing absorbance of the window materials near their

spectral cutoff. The blue scan shows the spectrum after turning off the cryocooler and introducing Argon at 222 K. With the heater and cryocooler off, the temperature rise was significantly slower than the scan time due to the large thermal mass of the cell. The red scan was collected after cooling the cell to 180 K.

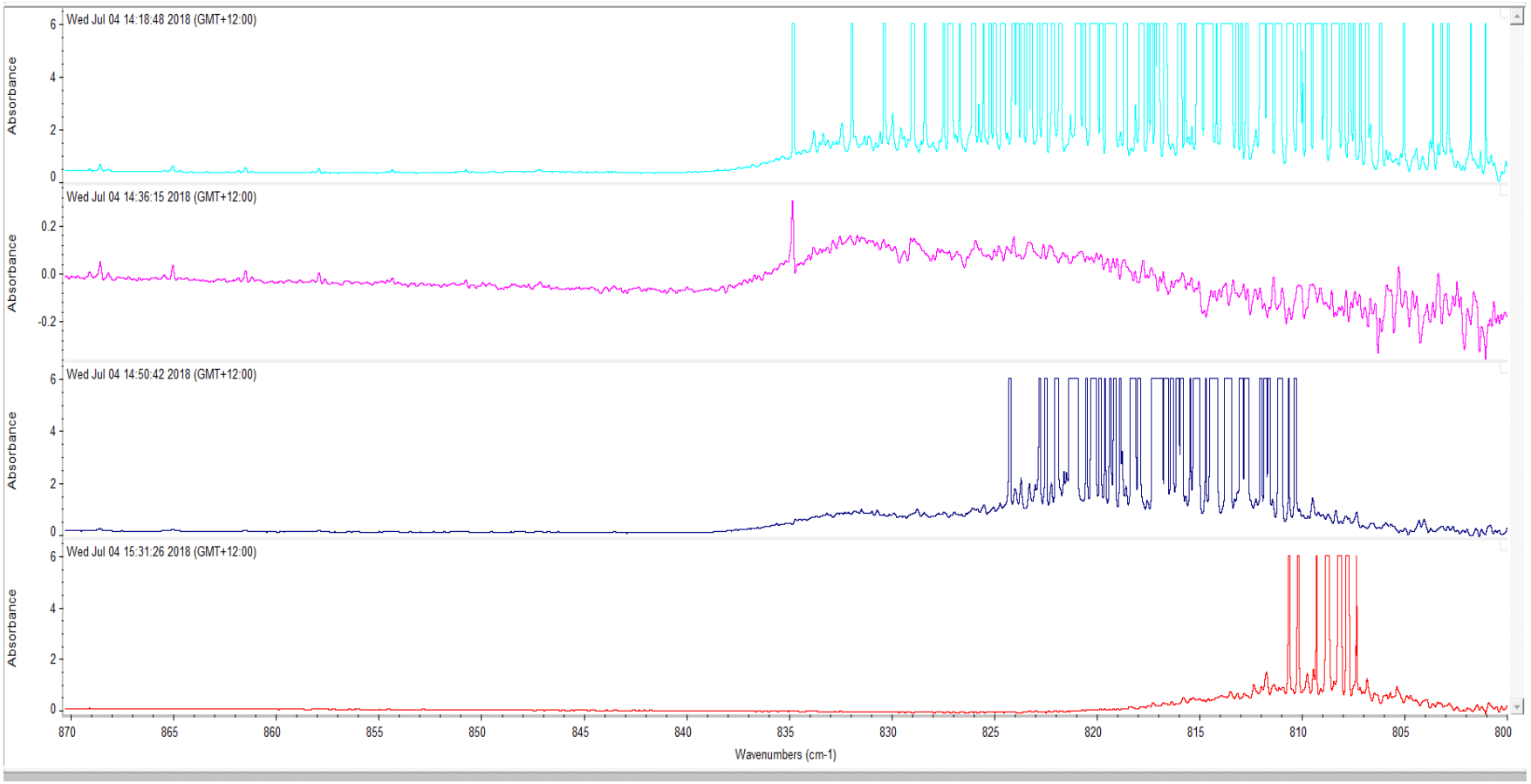

Figure 9 : IR scan for DCE showing the process at b_u CCl stretch (ν_{11}) before and add 1Atm of Argon, scan showing very intense CCl stretch absorption green at 230 K, Pink shows the DCE vapour under heating from 216 to 221 K with reduced transmittance of the cell due to the window materials, Blue shows the mixture with introducing Ar with cooler off at 222 K, Red showing after cooling to 180 K.

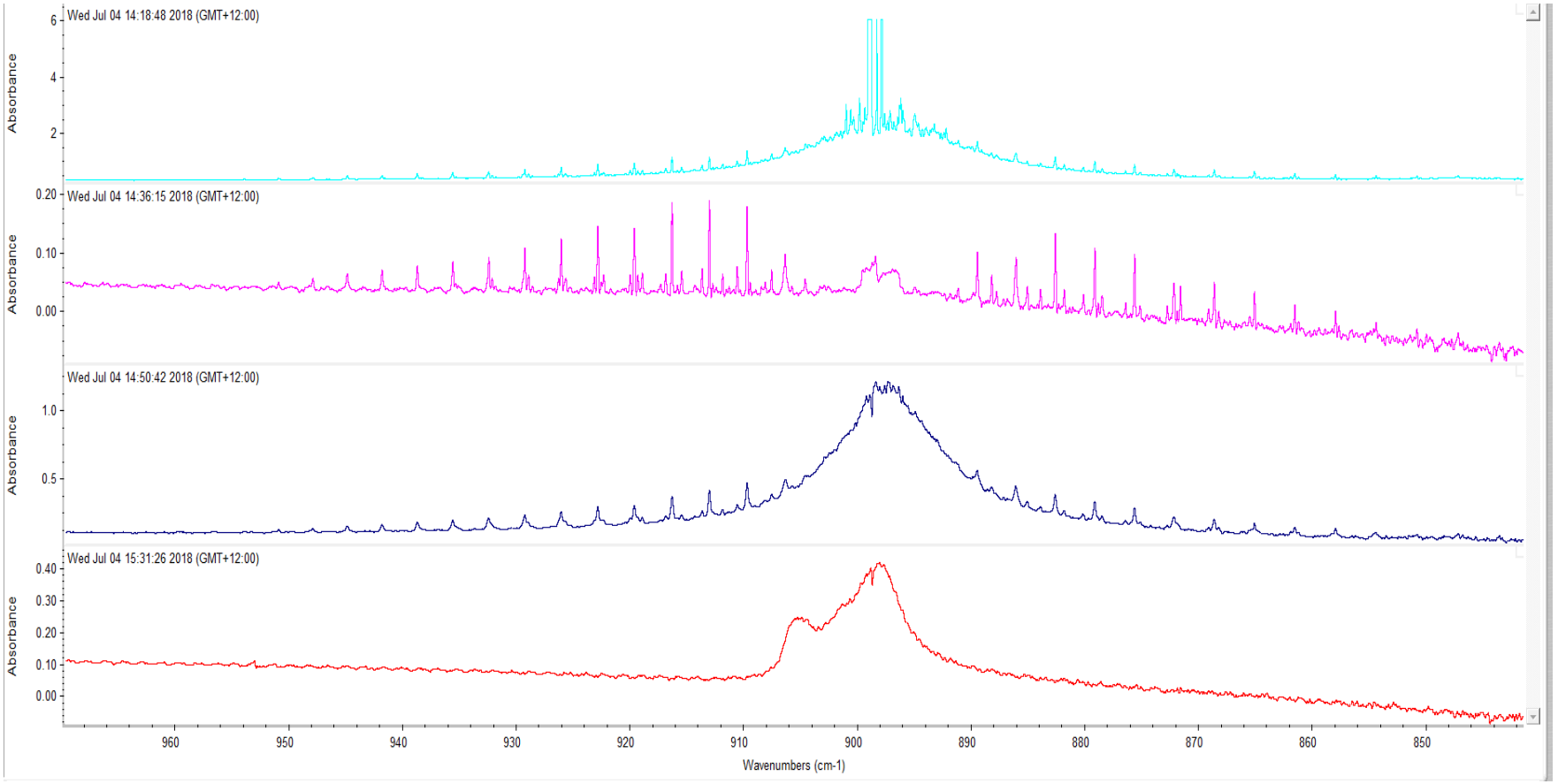

Figure 10 : IR scan for DCE showing the process at a_u CH bend (ν_6) before and after add 1 Atm of Argon. The DCE vapour are strongly absorbing (Green at 230 K), (Pink, under heating from 216 to 221 K) shows intense partially rotationally resolved data for DCE in the vapour state. (Blue) mixture with introducing Ar with cooler off at 222 K and (Red solid phase) after cooling to 180 K.

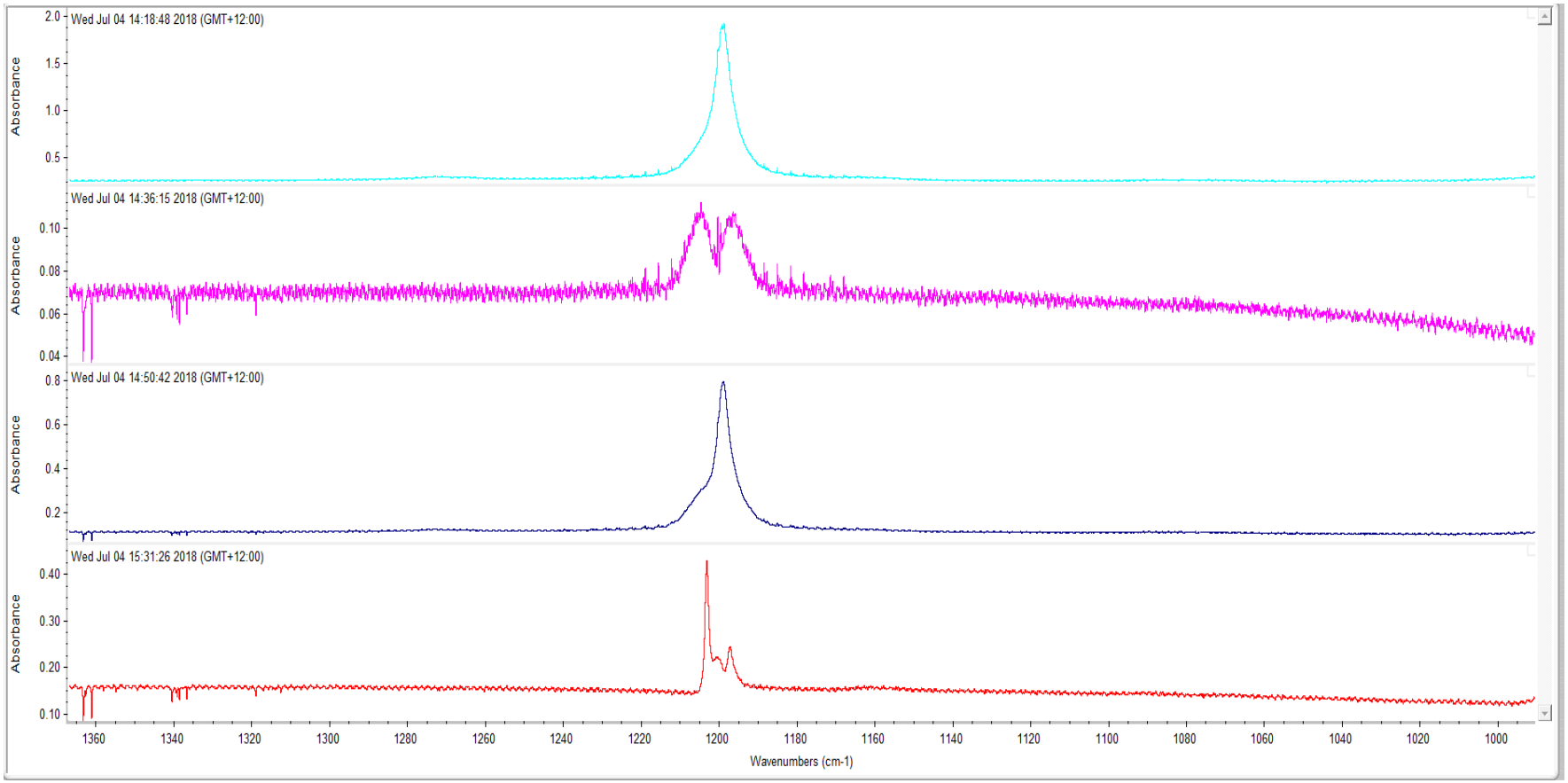

Figure 11 : IR scan for DCE showing the process at bu CH bend (ν_{10}) before and after add 1 Atm of Argon. Green scan is 230 K showing a narrow peak in liquid with small presence of DCE vapour, pink show the DCE vapour under heating from 116 to 221 K, Blue is DCE is with Argon at 222 K and Red is 180 K showing asymmetric line shape, the peak shift to opposite direction partially resolved to three peaks suggests isotope splitting due to the 37 and 35 isotopes of chlorine

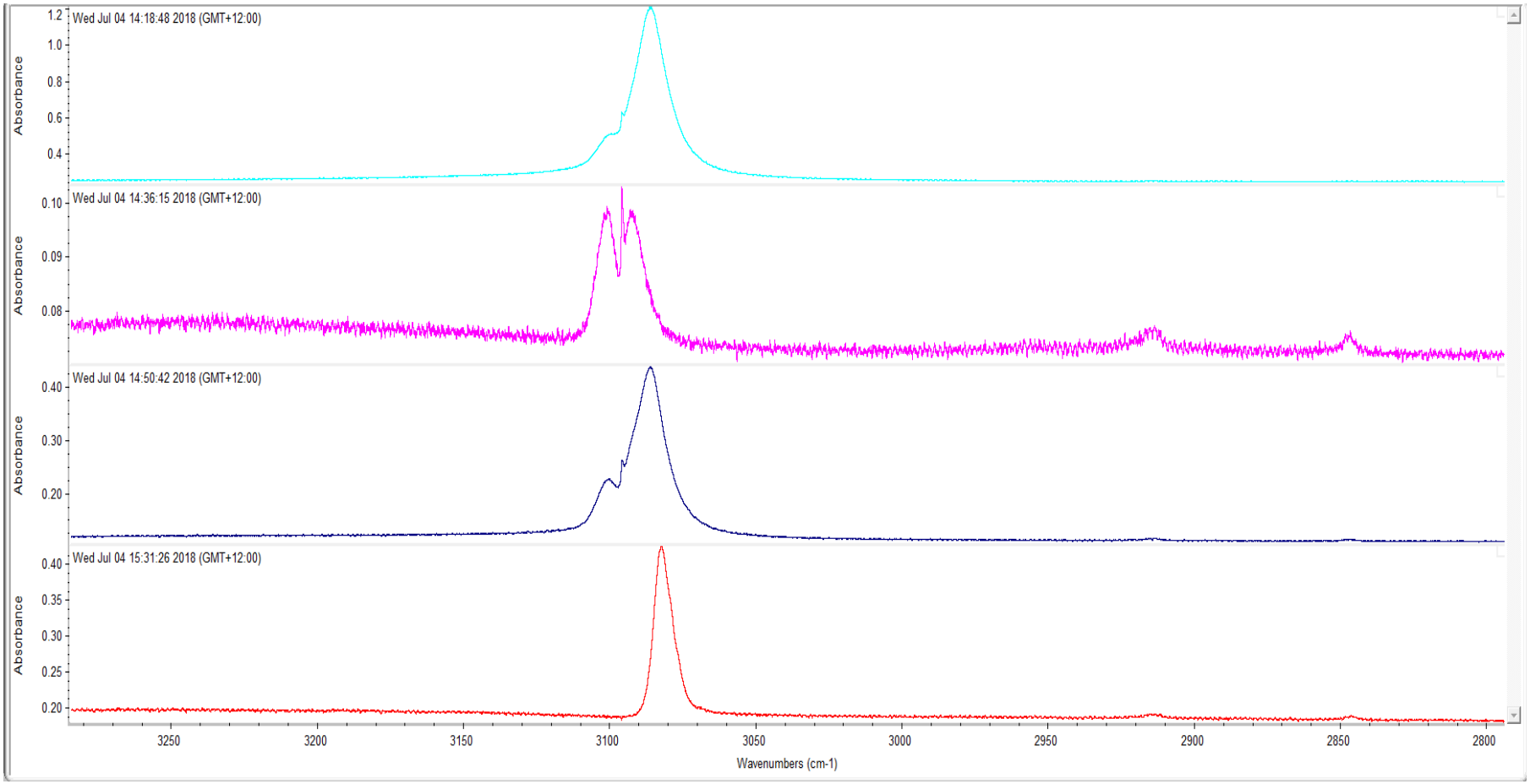

Figure 12 : IR scan for DCE showing the process at b_u CH stretch (ν_9) before and after add 1 Atm of Argon. Green scan is 230 K, shows the mixture of liquid and gas, Pink is DCE vapour with sharp middle peak under heating from 116 to 221 K, Blue scan with 8 Atm of Argon at 222 K shows loss of gas phase and Red scan shows the peak shift with asymmetric line shape at 180 K.

The energy of the resonances at a_u CH bend (ν_6) and b_u CCl stretch (ν_{11}) at b_u CH stretch (ν_9) and b_u CH bend (ν_{10}) is affected by the mass of the atoms and the shape of the molecular potential energy surfaces and their vibrational coupling. However, instead of the symmetric peak at b_u CH bend (ν_{10}), which corresponds to increased absorption that relates to the excitation of this mode in this mode, the asymmetric lineshapes displayed at b_u CH stretch (ν_9), b_u CH bend (ν_{10}) and with the peak corresponding to the b_u CH bend (ν_{10}) partially resolved to three peaks suggesting isotope splitting due to the 37 and 35 isotopes of chlorine. Consequently, the calculations indicate that the b_u CH bend (ν_{10}) may also be affected due to Fermi resonance which has been discussed in later sections.

The experiment was repeated by increasing the pressure of Argon to 8 Atm. The absorbance of tDCE decreased with a decrease in temperature, and by increasing Argon to more than one atmosphere, it was possible to maintain significant absorbance even to the melting point near 223 K. Below the freezing point at 200 K, the structure with increased absorption over the whole range of the spectrum presented new evident bands probably due to the presence of phonon modes, overtones, combination bands, and symmetry breaking dynamics in the crystalline phase. Possible band assignments will be discussed later in summary of results section.

The crystalline tDCE formed on the window, as visible in the figures 13,14 and 15, the increased absorbance at a_u CH bend (ν_6) and b_u CH bend (ν_{10}) peaks a decreased at b_u CH stretch (ν_9) with new weak absorption bands is also evident. The interactions between tDCE molecules are relatively weak due to the absence of any permanent dipole in it and only weak interactions between H and Cl on adjacent molecules.

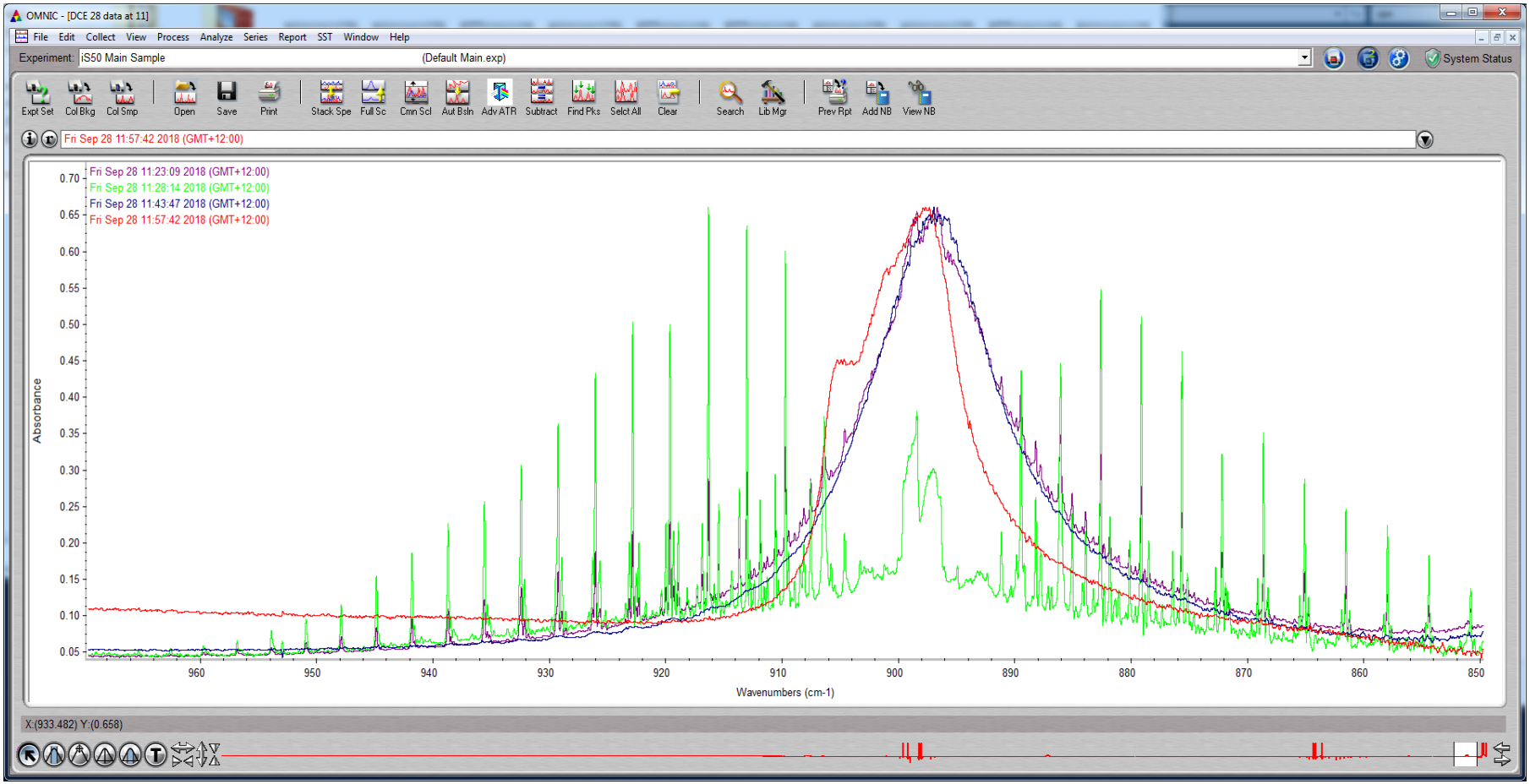

Figure 13 : IR scan showing different phases at a_u CH bend (ν_6) and the crystalline DCE after adding 8 Atm of Argon. Purple scan at T=231 K, shows the mixture of liquid and gas phase, Green is DCE vapour with present of rotational peaks at 224 K, Blue scan is 213 K after adding 8 Atm of Argon showing the liquid with loss of gas phase and Red scan shows the peak of solid phase at 199 K.

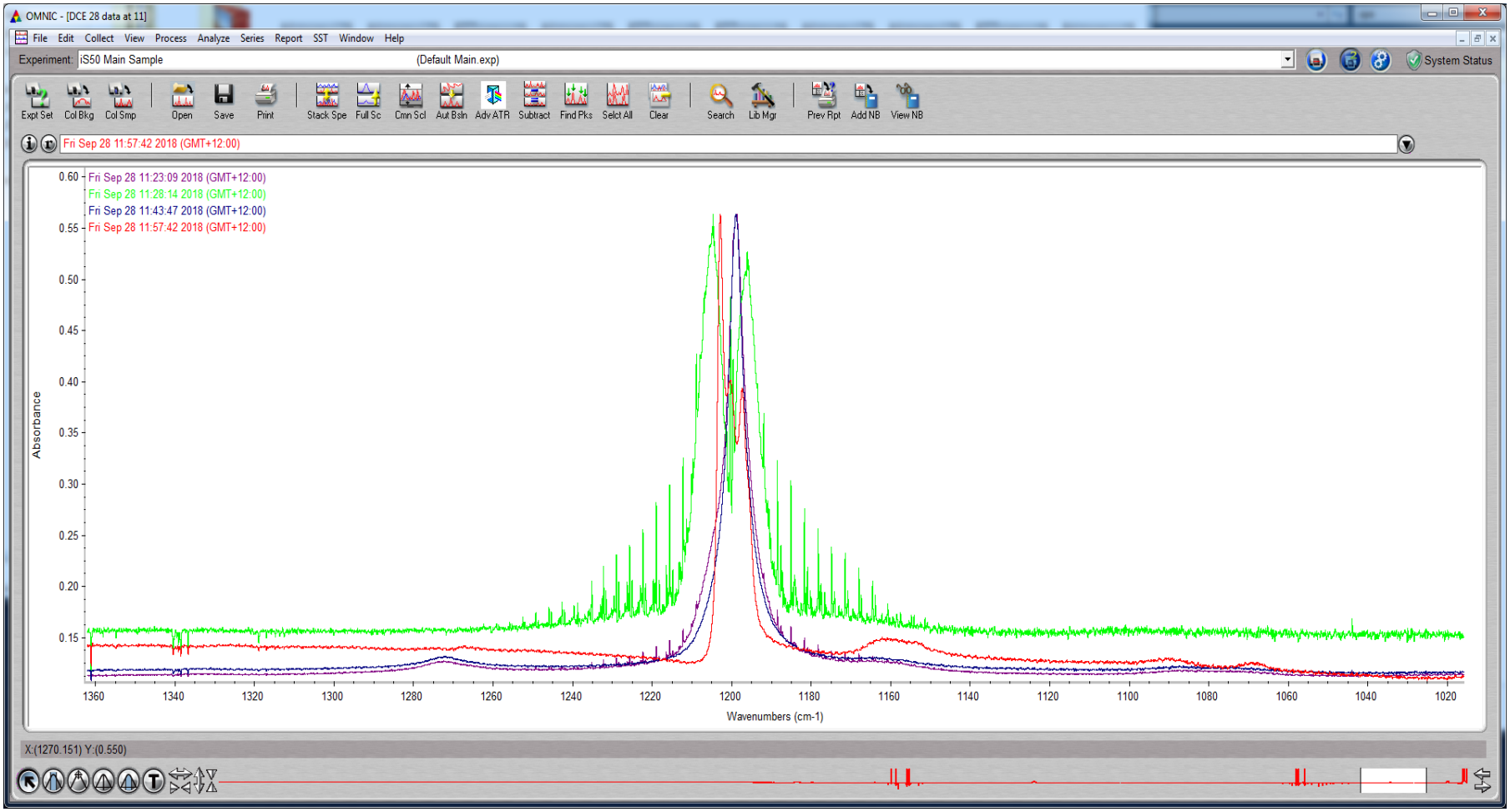

Figure 14 : IR scan showing different phases at b_u CH bend (ν_{10}) and the crystalline DCE after adding 8 Atm of Argon. Purple scan is 231 K showing a narrow peak in liquid with small presence of DCE vapour, Green is 224 K showing the DCE vapour with sharp middle peak with presence of rotational peaks, Blue is 213 K with 8 Atm of Argon, showing DCE liquid with loss of gas phase and Red scan showing the peak shift with resolved to three peaks in solid phase at 199 K.

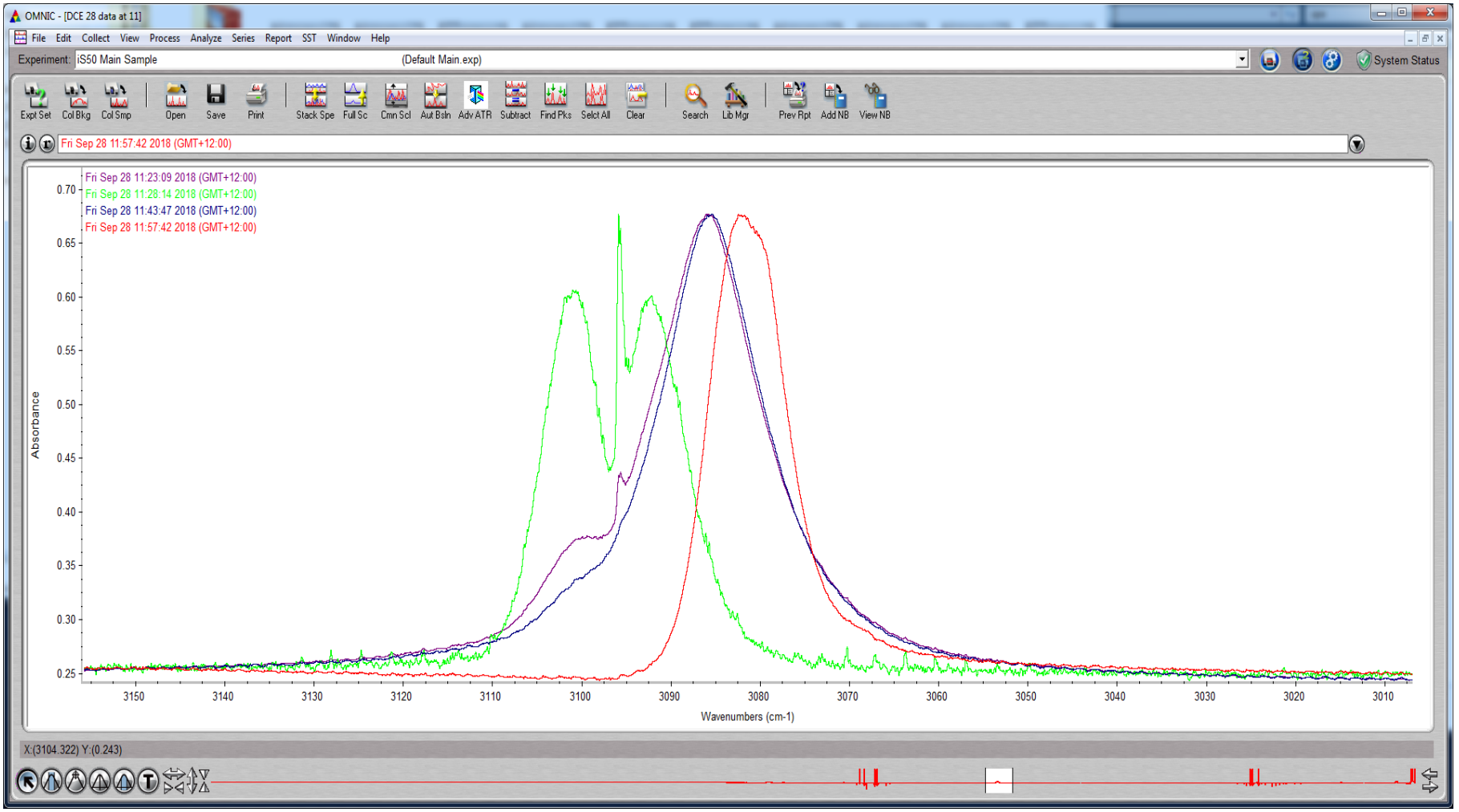

Figure 15 : IR scan showing different phases at bu CH stretch (ν_9) and the crystalline DCE after adding 8 Atm of Argon. Purple scan at 231 K, shows the mixture of liquid and gas, Green is DCE vapour with sharp middle peak with present of rotational peaks at 224 K, Blue scan with 8 Atm of Argon at 213 K shows the liquid with loss of gas phase and Red scan shows the peak shift in solid phase at 199 K.

As shown in figures 13,14 and 15, the deposited sample on the windows was able to switch between liquid and crystalline phases repeatedly under temperature cycles but was subject to loss of molecules due to evaporation or sublimation due to absorbing IR and the resulting local heating. This effect depends upon the original thickness of the solid (Pavithraa et al., 2017)

4.2. The absorbance spectra of the crystalline of trans-1, 2-dichlorothylen DCE

4.2.1. Low Temperature without thermal equilibrium. The importance of temperature on the crystal spectra and the sensitivity in temperature of the peak widths and intensities of many materials has been identified in numerous studies (Waters, 2009). Cooling tends to shift peak positions towards shorter wavelengths because of the contribution of crystal contraction and the linewidth reduces due to the phonon state density which decreases at low temperatures. While the widths of the phonon modes decrease with decreasing temperature, the broadening on the spectrum is also affected by disorder in the structure, crystal orientation and anharmonicity (Chen, Tanner, & Nino, 2005). In this work, we will discuss the relationship between the appearance of Fano resonances and the behaviour at low temperatures and how that affects the crystal spectra. The figures 16, 17, 18 and 19 show the experimental IR spectra of tDCE absorptions at different phases and in crystalline phase at 117 K. The spectra were recorded with 16 scans at 0.125 cm^{-1} resolution as the cell was cooled with no Argon. The tDCE vapour was introduced to the cell at 230 K and then cooled down to below the freezing point of the DCE followed by the spectra being acquired in steps of -2 K or 3 K to 117 K. This allowed the sample to form on the window.

The scans of tDCE vapour at 228 K in the figures 16,17,18 and 19 demonstrate the peak of the b_u CH stretch (ν_9) and of the b_u CH bend (ν_{10}), the CH bend (ν_6) and b_u CCl

stretch (ν_{11}) in the gas phase. The CH bend (ν_6) and b_u CCl stretch (ν_{11}) strongly absorb and show intense partially rotationally resolved data for DCE in the vapour state.

The (ν_9) and (ν_{10}) peaks demonstrated the most significant change in shape and position as conditions changed; the peak wavenumbers have been summarised in Table 2.

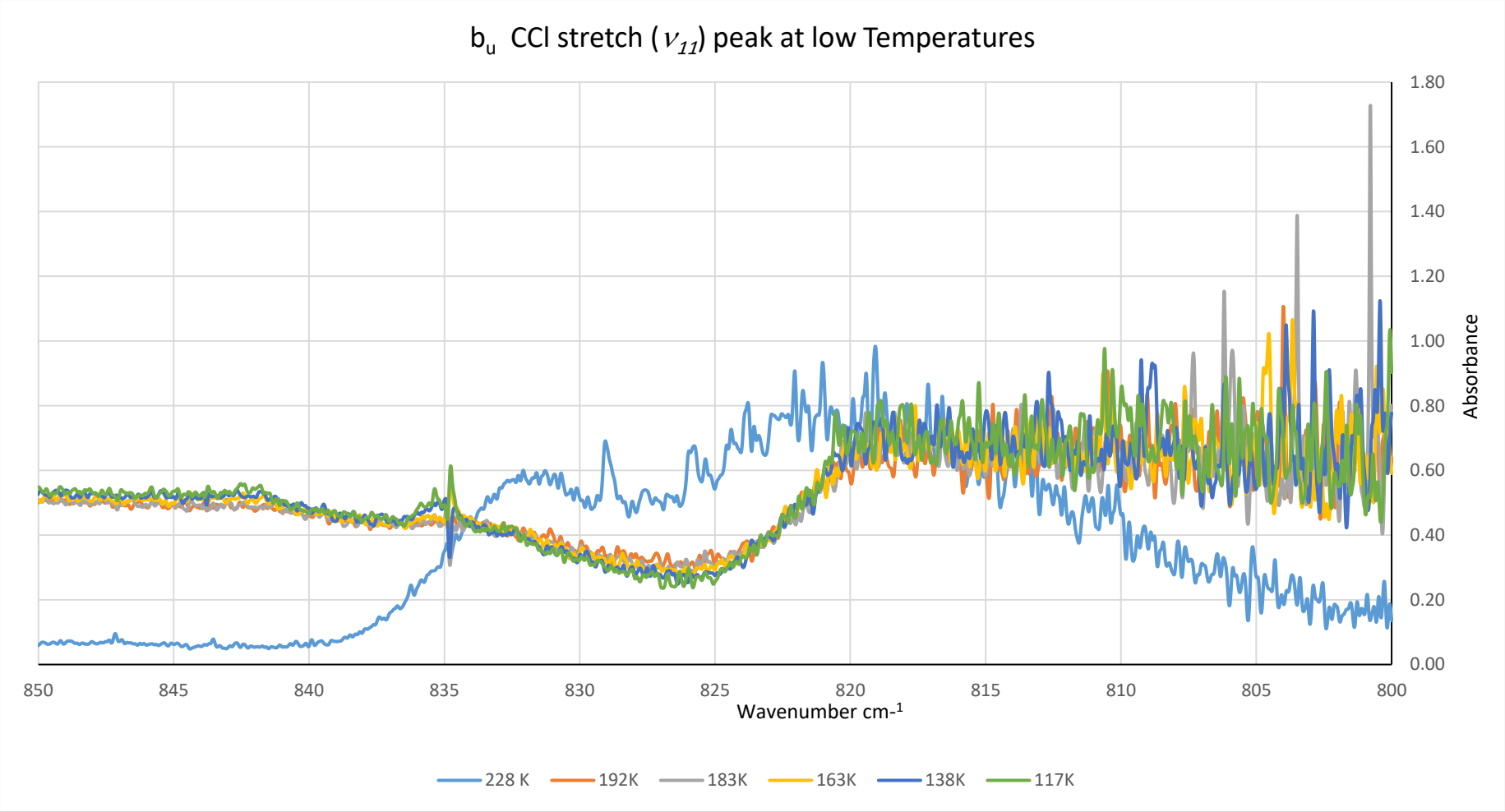

Figure 16 : IR scan for DCE showing the process with no Ar at b_u CCl stretch (ν_{11}). Blue scan is broadened DCE vapour at 228 K, other 192,182,163,138 and 117 K sowing the complicated line shape in solid phase.

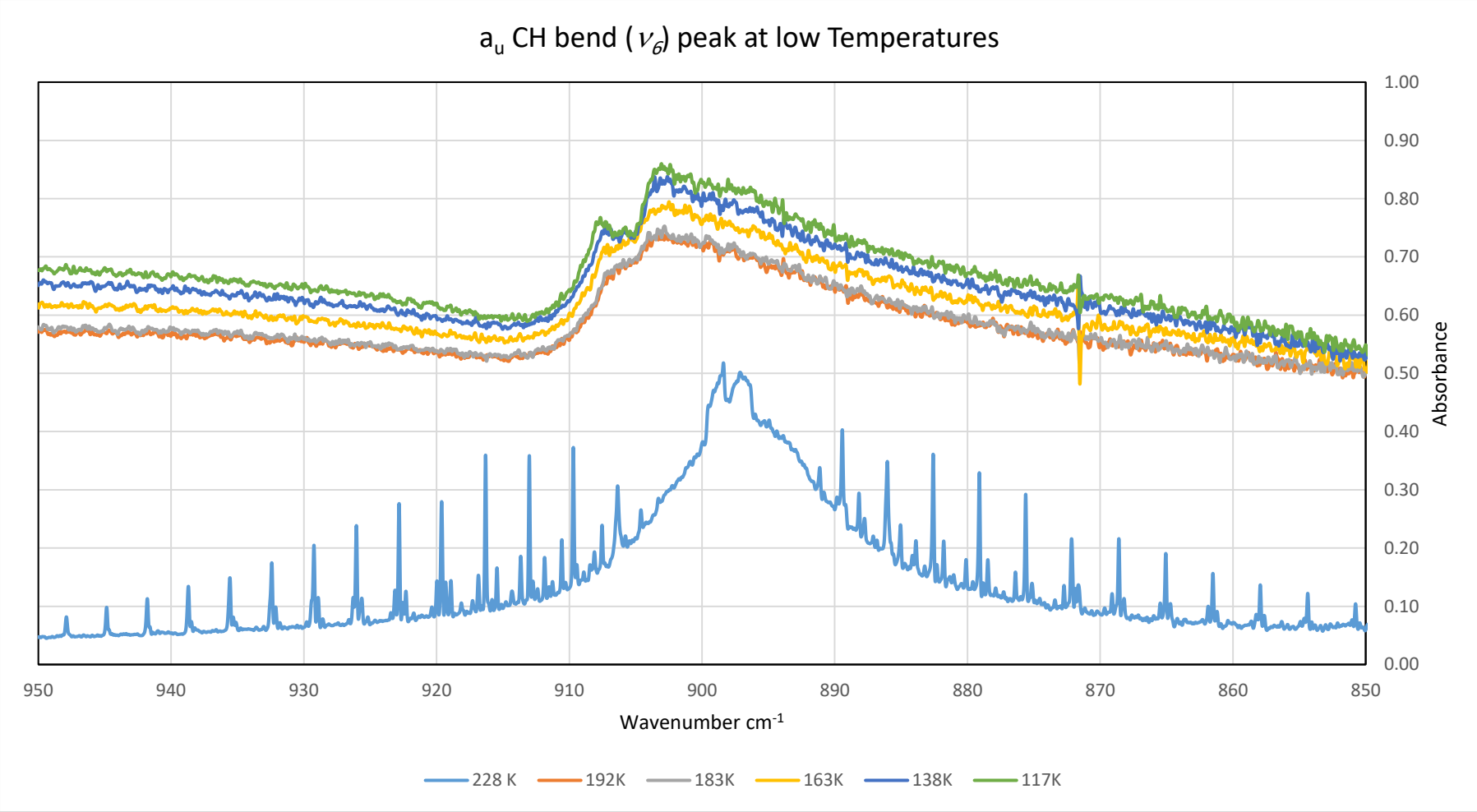

Figure 17 : IR scan for DCE showing the process with no Ar at CH bend (ν_6). Blue scan shows the peak is strongly absorbing and showed intense partially rotationally resolved data for DCE in the vapour state. The scan at 192,183,163,138 and 117 K in solid phase with presence of asymmetric lineshape (Fano resonance) with resolves to three peaks but the analysis of these peaks was difficult due to a large baseline drift.

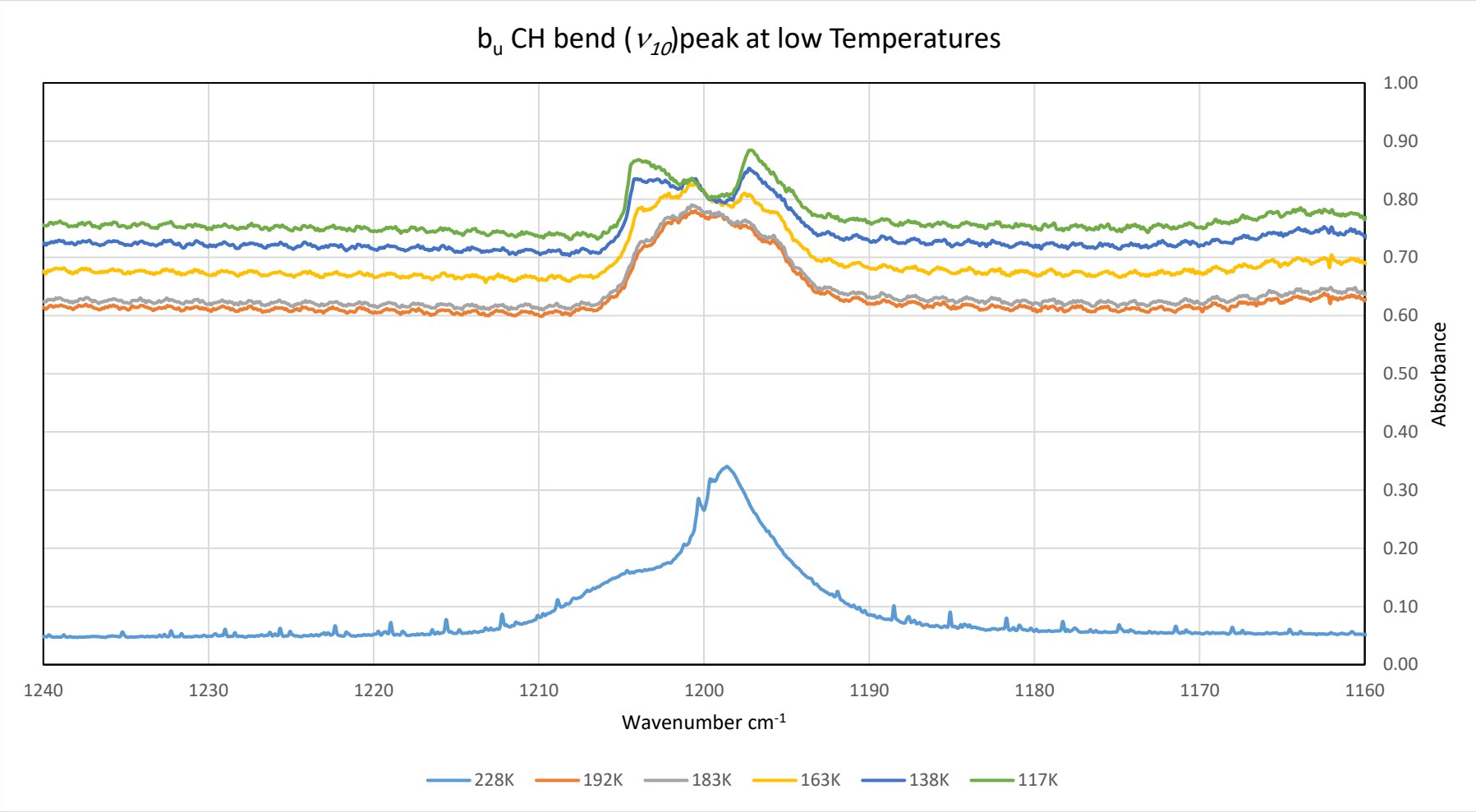

Figure 18: IR scan for DCE showing the process with no Ar at b_u CH bend (ν_{10}). Blue scan shows the peak of DCE in liquid phase with smaller present of rotational peaks of the vapour state. The scan at 192,183 and 163 K showing the peak with asymmetric lineshape in solid phase and 138 K and 117 K with presence of asymmetric lineshape (Fano resonance) with resolves three peaks with shift to high frequencies but the analysis of these peaks was difficult due to smaller amplitude.

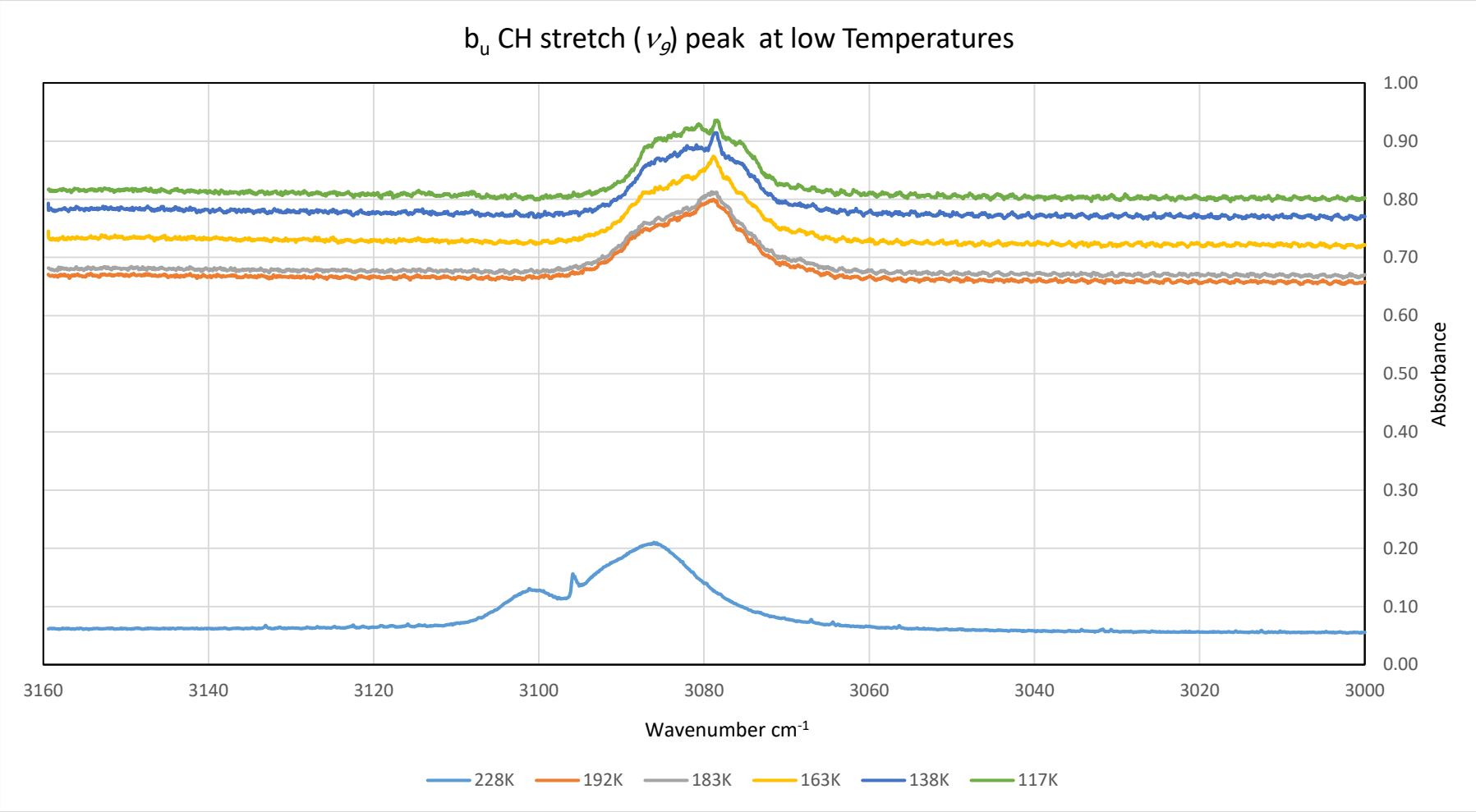

Figure 19 : IR scan for DCE showing the different phases at b_u CH stretch (ν_9) with no Ar. Blue scan shows the broadened of DCE vapour compare to the other scans with peaks shift to low frequencies in solid phase.

Temperature	Position peak			
Kelvin	NIST	NIST	NIST	NIST
	a_u CH bend (ν_6) cm^{-1} 899.8 VS Gas phase	b_u CH stretch (ν_9) cm^{-1} 3090 S Gas phase	b_u CH bend (ν_{10}) cm^{-1} 1200 S Gas phase	b_u CCl stretch (ν_{11}) cm^{-1} 828 VS Gas phase
DCE with no Argon				
230	897.51 Gas 898.54 Gas	3100.77 Liquid 3095.95 Gas 3086.26 Liquid	1198.98 Liquid 1199.69 Gas 1200.39 Gas	819.14 (!) 829.12 (!) 831.47 (!)
214	898.62 Solid 897.16 Solid	3101.33 Solid 3095.96 Solid 3083.07Solid	1199.24 Solid 1200.45 Solid 1202.25 Solid	820.49 (!)
192	901.53 Solid	3079.44 Solid	1201.47 Solid	825.68 (!)
183	903.46 Solid	3080.34 Solid	1199.93 Solid	825.80 (!)
163	903.52 Solid	3079.19 Solid 3086.62 Solid	1202.68 Solid 1201.11 Solid 1197.78 Solid	826.36 (!)
138	903.38 Solid 906.18 Solid 907.36 Solid	3081.33 Solid 3078.88 Solid	1204.30 Solid 1201.03 Solid 1197.55 Solid	820.74(!)
117	903.89 Solid 906.70 Solid 908.05 Solid	3081.35 Solid 3078.76 Solid	1204.45 Solid 1201.03 Solid 1197.55 Solid	820.65(!)

Table 2: Due to no much change in peak positions with large data between 2 and 3 K, summary of observed peaks of DCE at different period at low Temperature with no Argon. (!) Uncertainty due to noisy baseline with present of asymmetric line shape.

4.2.2. Low Temperature with thermal equilibrium. The absorbance spectra of crystalline tDCE was measured as the cell was cooled, with approximately 10 Atm of Argon. Crystals on the cell windows were obtained after the vapour was introduced into the cell at 230 K then cooled down to allow the formation of solid DCE on the window. The IR bands and their intensities of the spectrum at 120 K are presented in (Appendix 4) and have been discussed in summary of results section. The energies of the resonances of the a_u CH bend (ν_6), b_u CCl stretch (ν_{11}), b_u CH stretch (ν_9) and b_u CH bend (ν_{10}) are affected by the isotopic mass of the atoms and the shape of the molecular potential energy surfaces and their vibrational coupling. As compared to 4.2.1, where thermal equilibrium has not been established, the atoms of the molecules in crystal vibrate about their equilibrium positions, while the appearance of new bands in the 117 K spectrum are attributed to the anharmonic interaction between the neighbouring configurations of other molecules coupled via the weak interactions between the molecules. However, instead of the expected identical peak shape for both temperatures, the Fano resonance is clearly different for the asymmetric peaks at b_u CH bend (ν_{10}), b_u CH stretch (ν_9), a_u CH bend (ν_6) and b_u CCl stretch (ν_{11}). This behaviour could be due to a change in the crystal size or morphology with corresponding different phonon interactions as the widths of these modes are temperature dependent. The relative absorbance due to phonon/continuum modes is clearly different in the two scans, which implies that disorder plays an important role in the presence and shape of Fano resonances. All observed behaviour will be reviewed in this thesis.

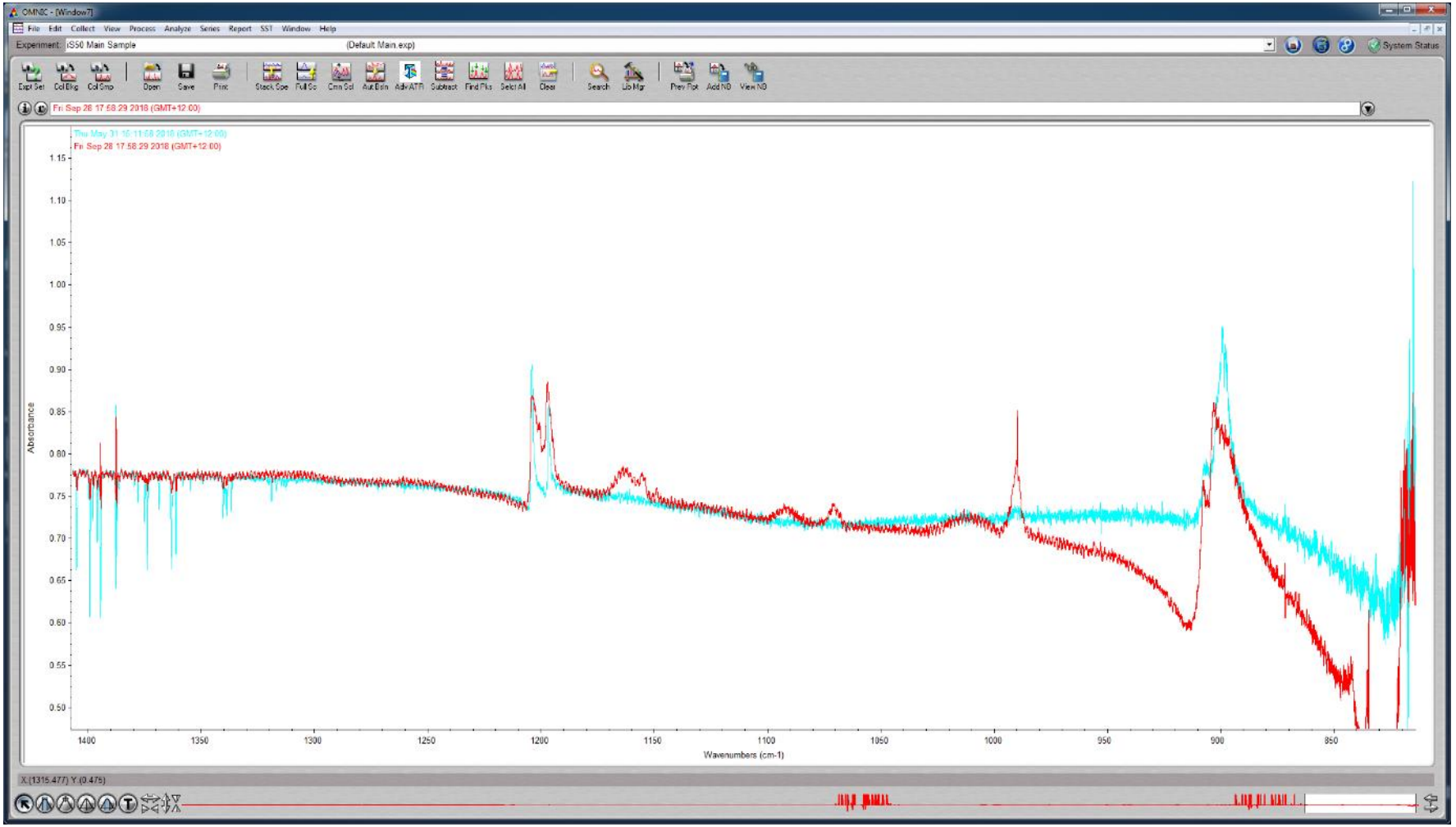

Figure 20 : The crystalline DCE spectra at 800-1400 region, presenting different behaviour at two low temperatures: Red 117 K & Blue 120 K.

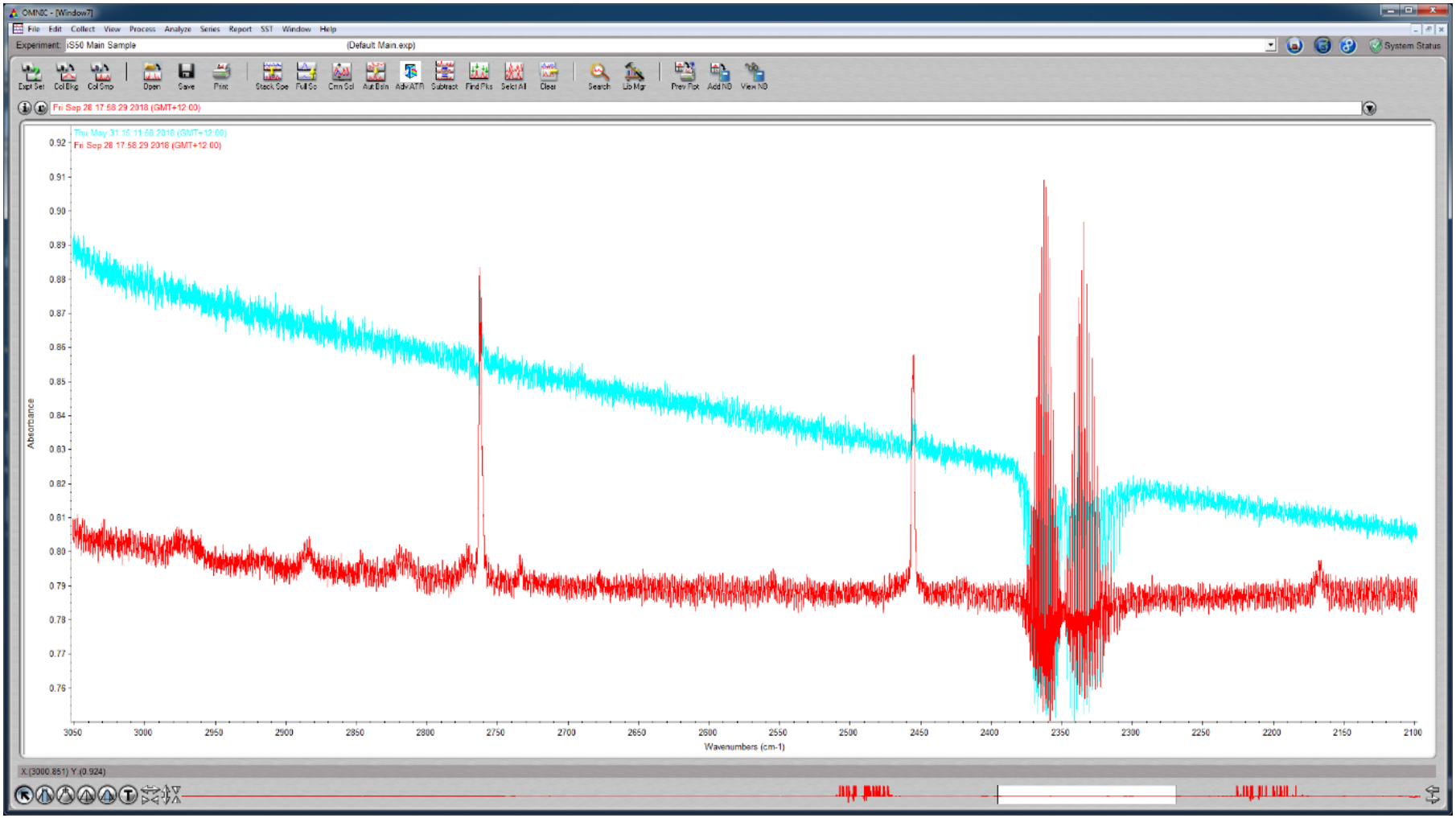

Figure 21: The crystalline DCE spectra at 2000-3000 region, presenting two different behaviours at low temperatures: Red 117 K & Blue 120 K.

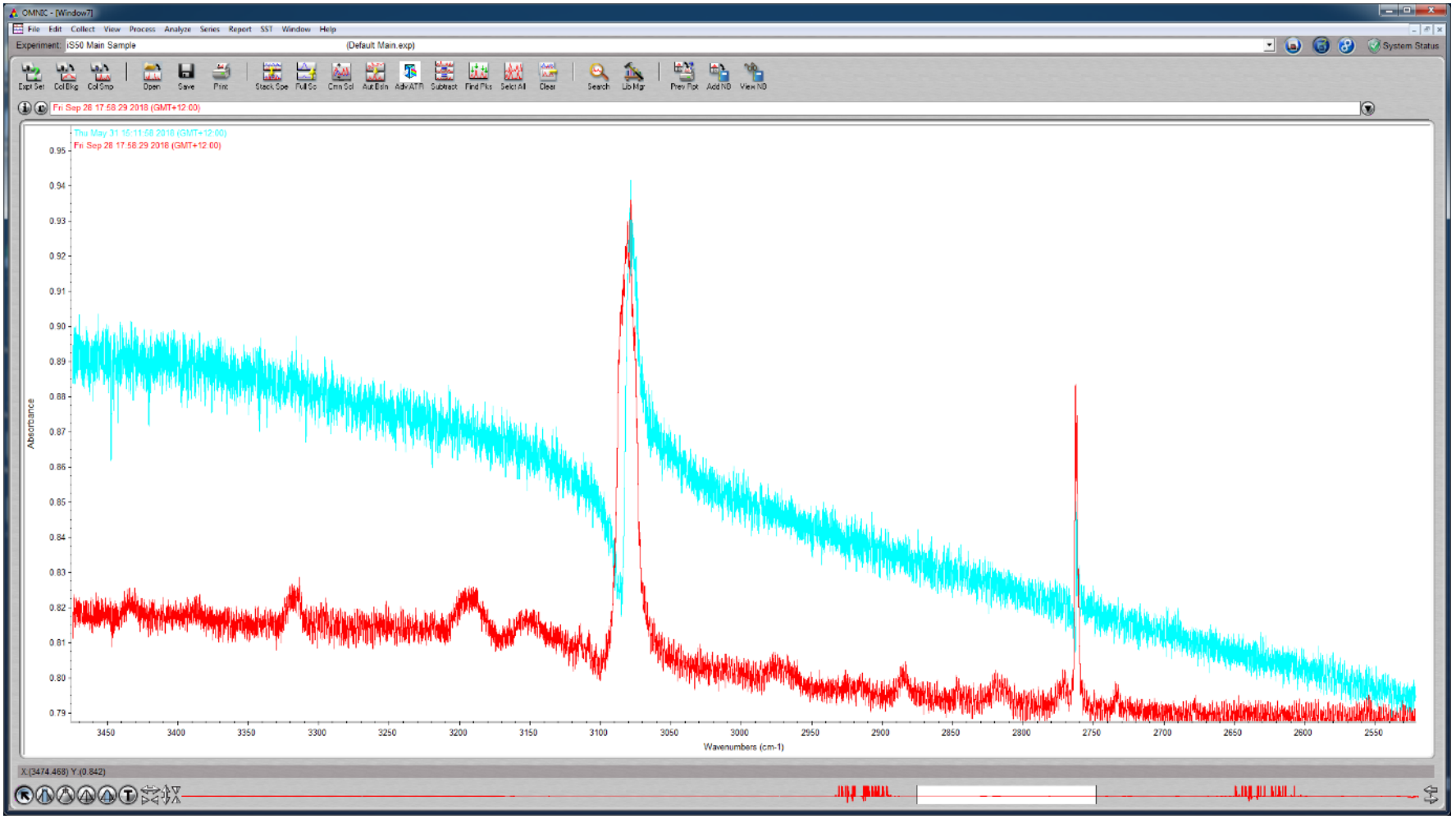

Figure 22: The crystalline DCE spectra presenting the behaviour at b_u CH stretch (ν_9) at different low temperatures, the blue is 120 K and red is 117 K.

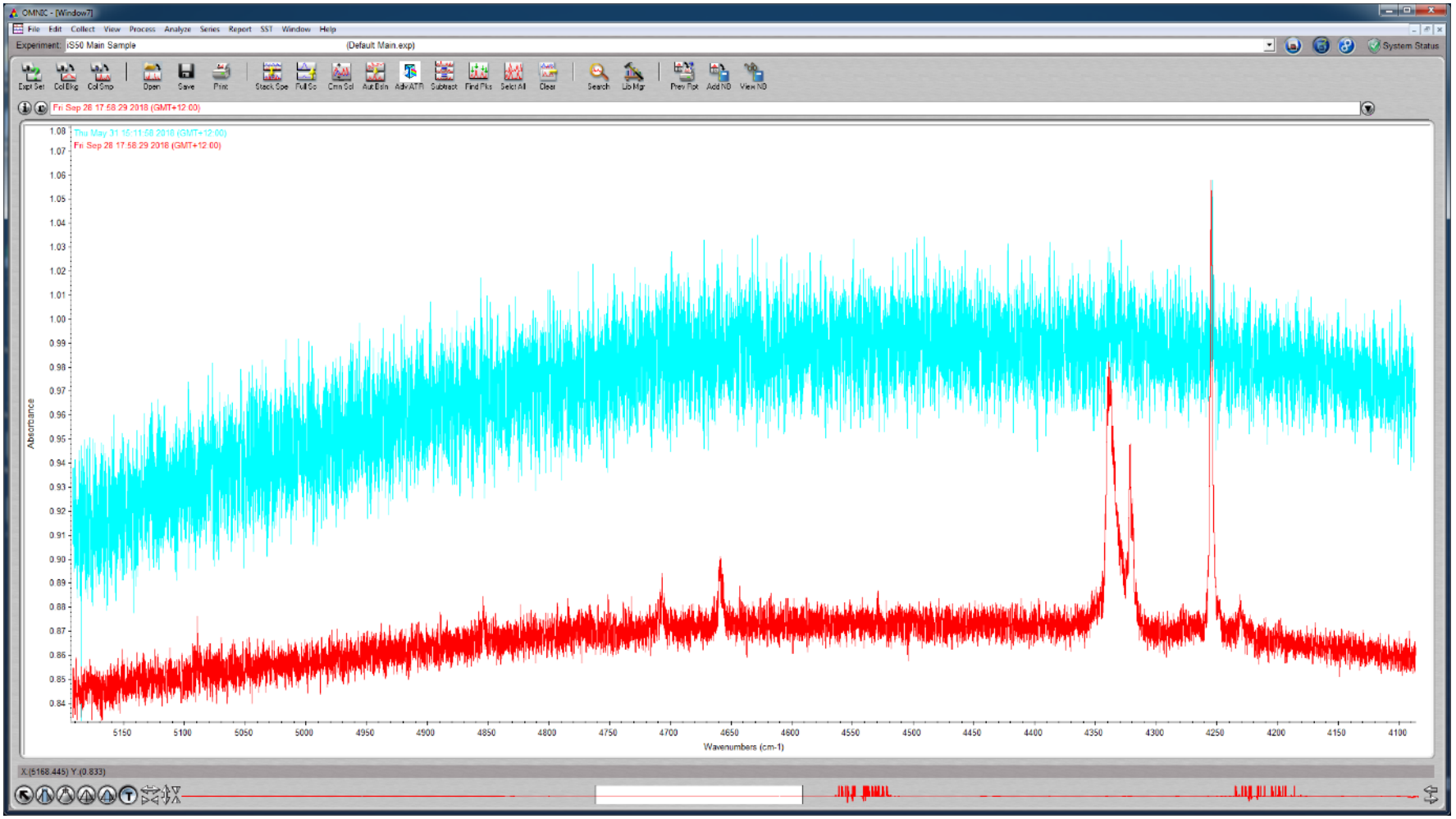

Figure 23: The scan for DCE at the high energy, overtone region.

4.2.3. High Temperature.

To record the behaviour at high temperatures till and beyond the melting point, crystalline tDCE formed on the windows as the cell was cooled to 180 K. Following this, data was collected by warming over a range of temperatures with one or two K spacing till the melting point which is around 223 K.

The obtained spectra were dominated by the four active infrared transitions for tDCE that were accessible at energies greater than 800 cm^{-1}. The spectra for b_u CH stretch (ν_9) and b_u CH bend (ν_{10}) at different temperatures have been shown in figures 24 and 25. As a result of the problem associated to baseline drift in the low frequency region, this study will focus on the peaks at b_u CH stretch (ν_9) and b_u CH bend (ν_{10}) as shown in figures 24, 25, 26, 27 and 28.

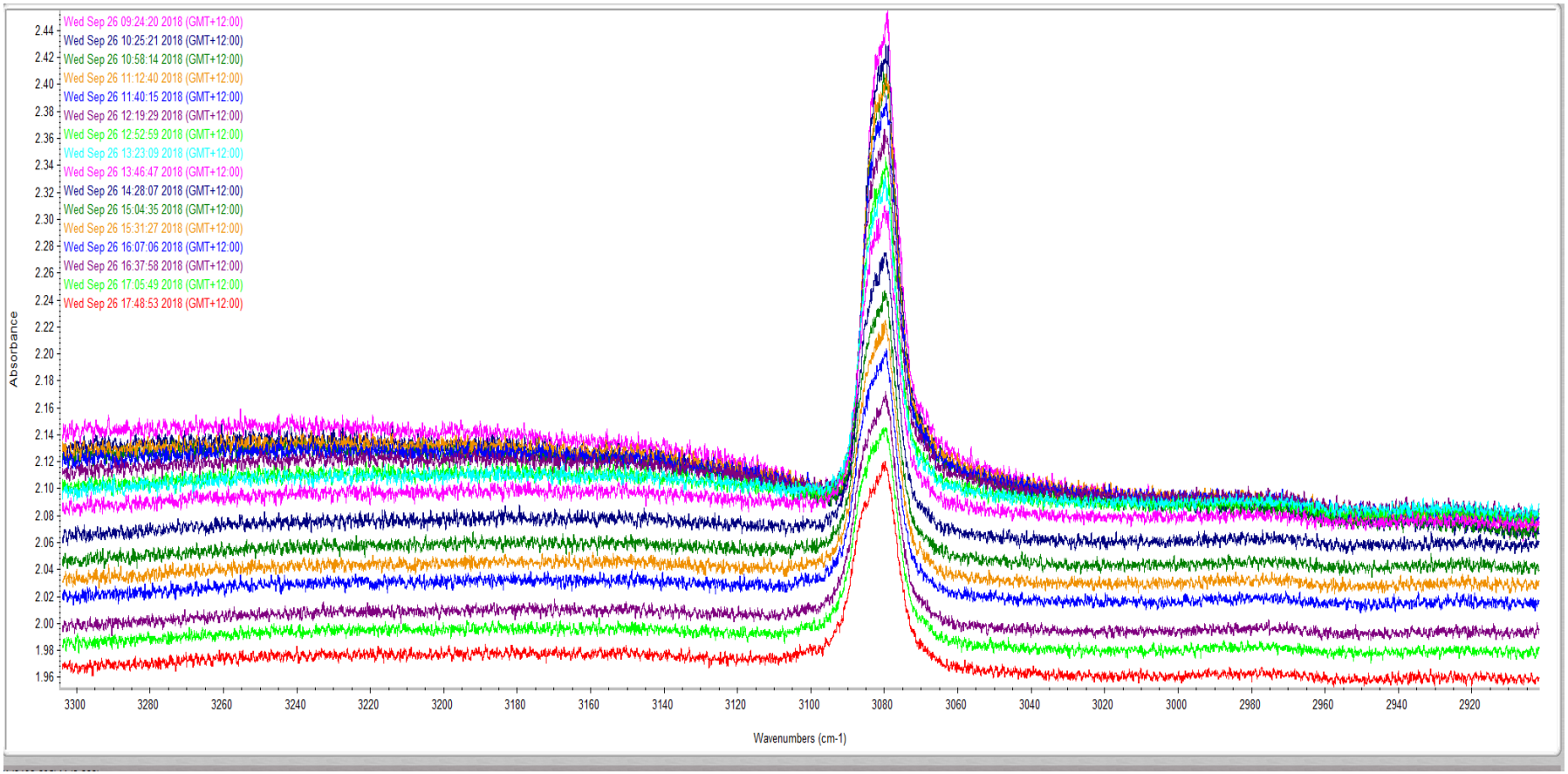

Figure 24: IR spectra for the crystalline tDCE at b_u CH stretch (ν_9) with increasing temperature (1-2 K increments) to study the behaviour of Fano parameter with heating: From the top at180 K to the bottom at 206.66 K.

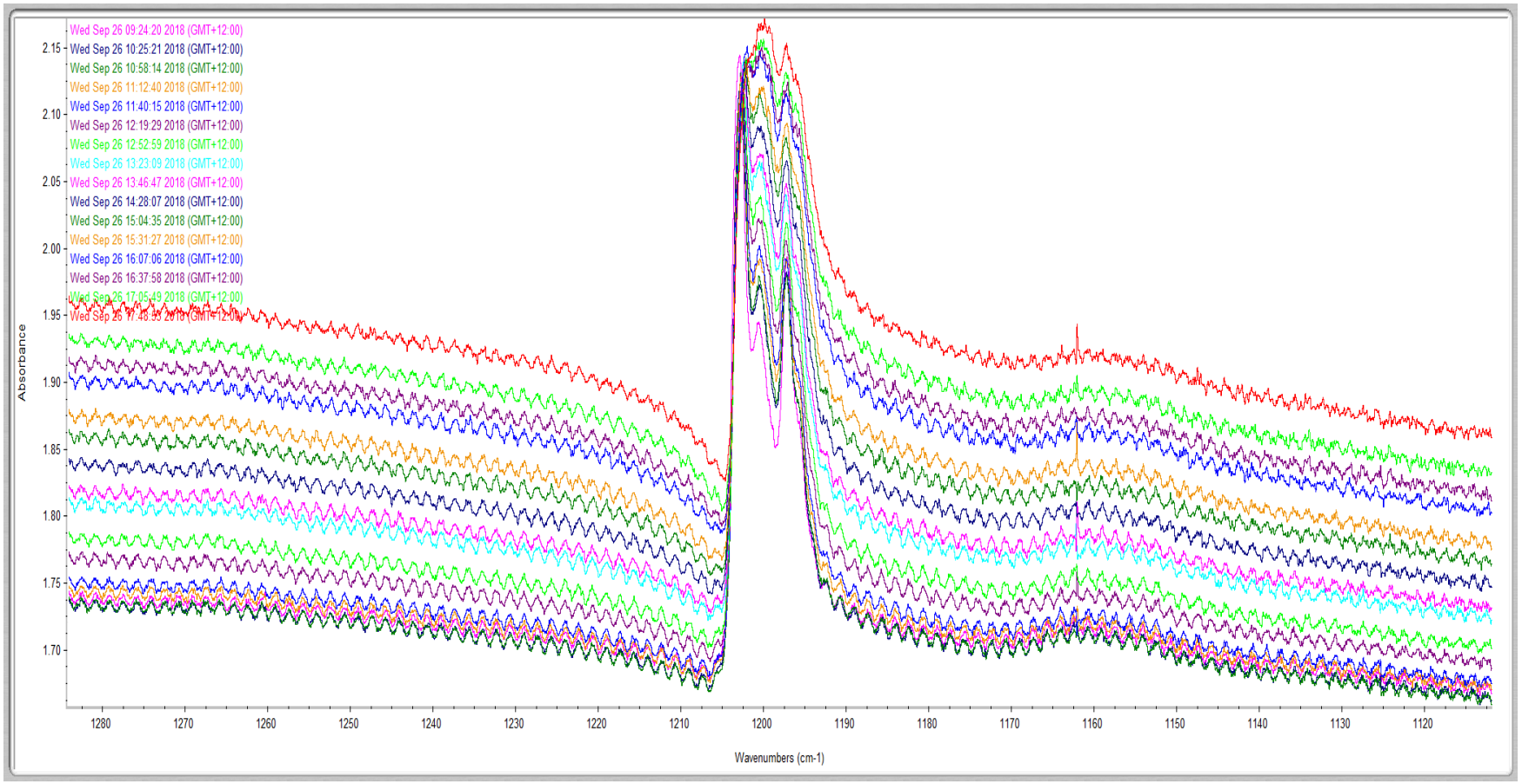

Figure 25 : IR spectra for the crystalline tDCE at b_u CH bend *(ν_{10})* with increasing temperature (1-2 K increments) to study the behaviour of Fano parameter with heating. From the bottom at180 K to the top at 206.66 K.

Figure 26 : IR spectra for the crystalline tDCE at b_u CH stretch (ν_9) at a temperature of 199.8 K. Note that the absorption is low due to IR heating the sample and molecules being lost from it. The small regular oscillations are due to window interference and the larger negative going peaks are due to an increase in water vapour background.

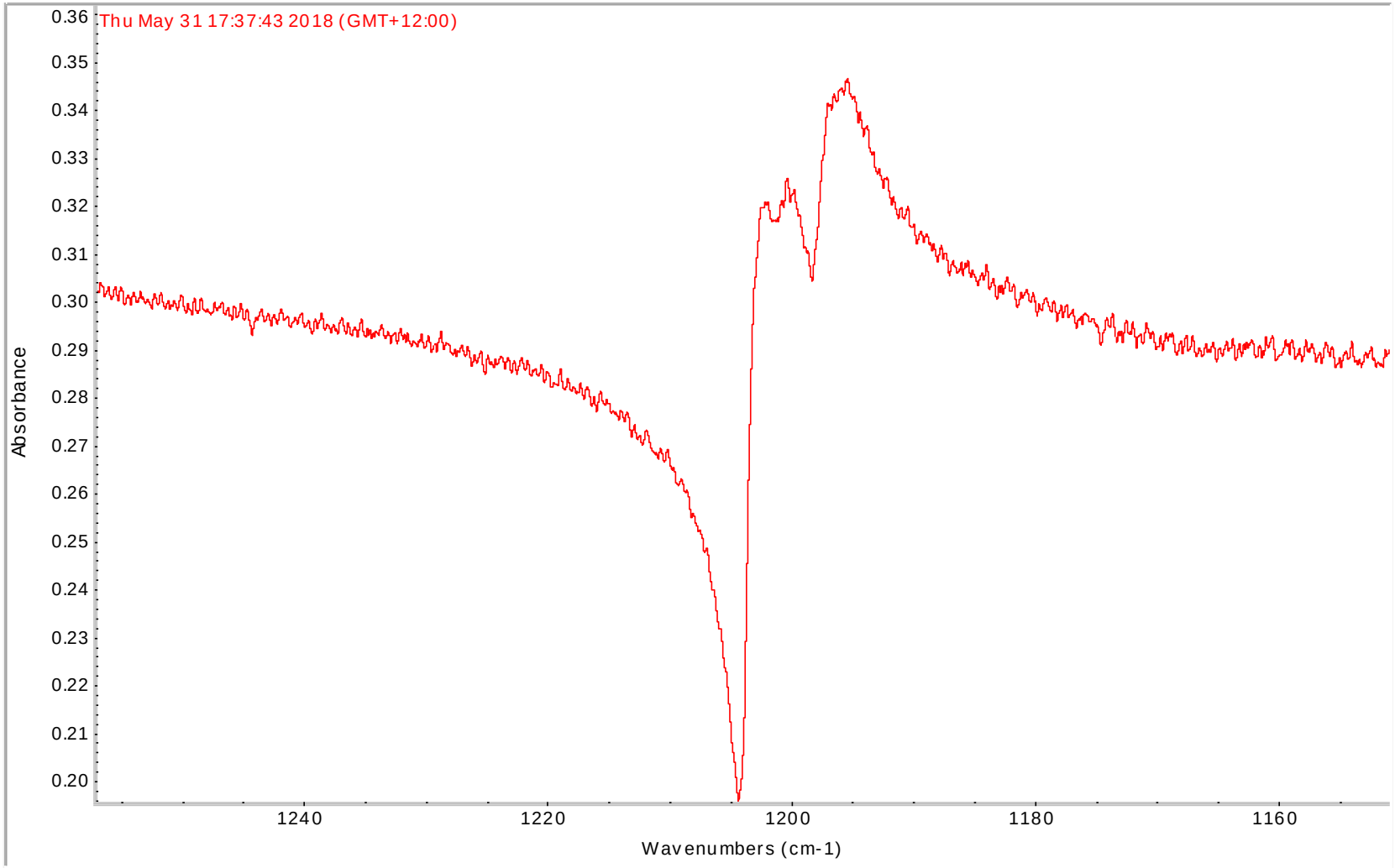

Figure 27: IR spectra for the crystalline DCE at b_u CH bend (ν_{10}) at a temperature of 199.8 K to study the behaviour of the Fano lineshape parameters with heating as energy is being absorbed by the crystal. Note the high absorbance from the background continuum and the resulting peak inversion which is a spectral signature of Fano interference.

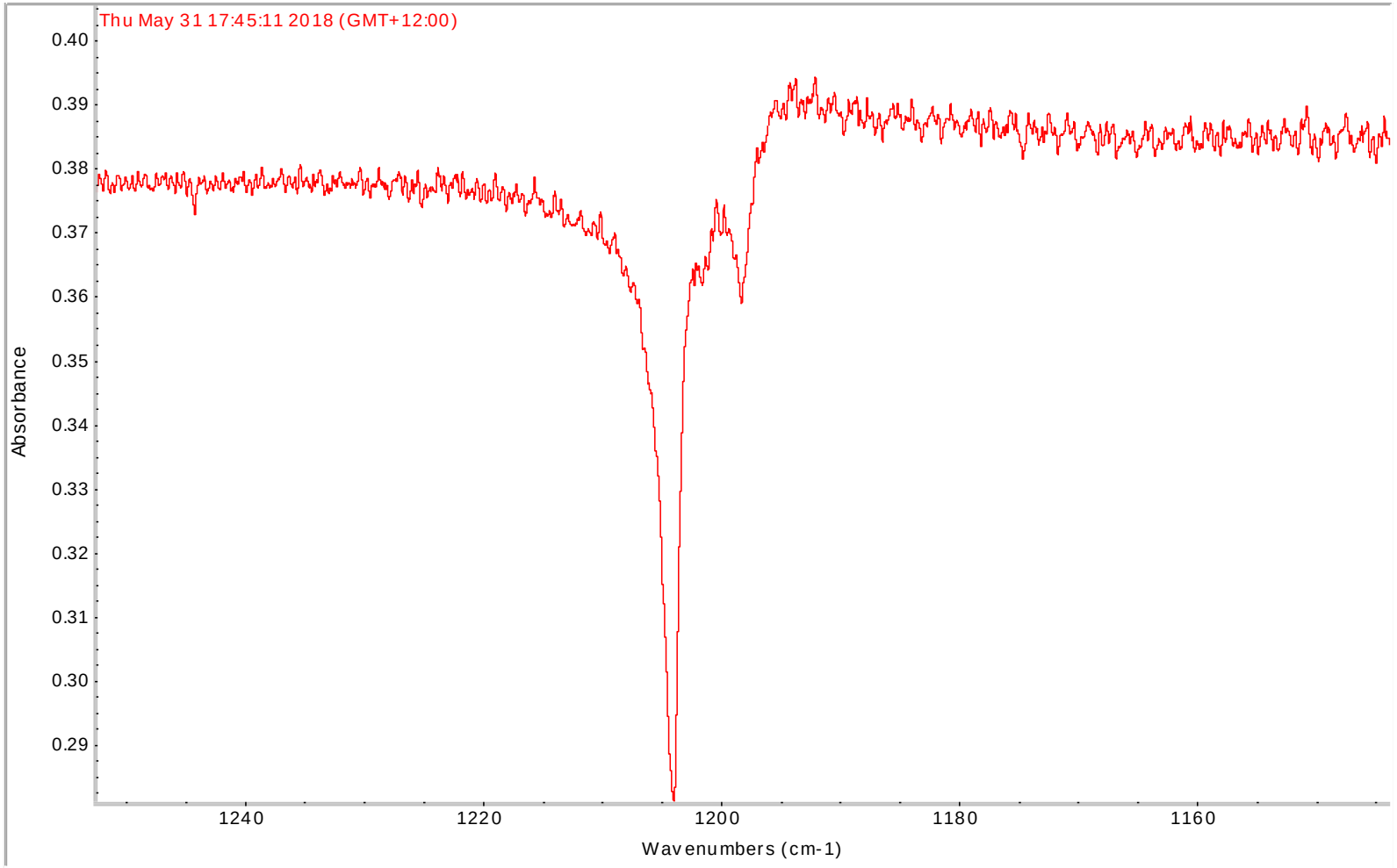

Figure 28 : IR spectra for the crystalline DCE at b_u CH bend (ν_{10}) at a temperature of 204.96 K, to study the behaviour of the Fano lineshape parameters with heating as energy is being absorbed by the crystal.

As observed, under sample heating conditions, the behaviour is quite different from that of using cooling conditions. Heating the Fano coupling between the discrete state vibration makes the continuum evident. It is difficult to directly compare the absolute values of the absorbance between scans at different temperatures due to the loss of sample as the crystalline DCE absorbs IR energy. It is possible to compare the relative intensities between the intensity of the continuum absorption and the discrete state absorption as both should be proportional to the amount of the present sample. There is the additional complication of scattering of light due to the finite size of the crystals and light lost by the IR beam being refracted off the optical detection axis. In the spectra in figures 24–28, there is also an apparent correlation between the linewidth and the Fano asymmetry of the peak. Fundamentally, the narrower the linewidth is, the stronger the coupling to the continuum becomes.

4.3. Fano Profiles

Strongly asymmetric Fano lineshapes are not generally found in infrared spectra. Due to the problem associated to the baseline drift at low frequencies in the region of a_u CH bend (ν_6) and b_u CCl stretch (ν_{11}), we will focus on analysing the Fano profiles at approximately 3090 cm^{-1} and 1200 cm^{-1} of the crystalline tDCE (the ν_9 and ν_{10} modes) that correspond to the CH stretch and CH bend, respectively. Fano resonance asymmetry of these modes was observed directly as the experimental results show the appearance of Fano resonance. There was a significant difference between the cases of high temperature and low temperature. This suggests that it was related to the crystal size, morphology and temperature changing population of the low frequency lattice modes in the crystalline phase.

To prove that the asymmetric lineshapes related to the absorption spectra of the crystalline tDCE are in fact due to Fano resonance and determine the ratio of these couplings, we should first fit the experiment data to the Fano profile formula.

4.3.1. Fit with Fano profile. Origin Lab software[1], Peak Analysis, Breit-Wigner - Fano (BWF) function was obtained to plot the fundamental lineshape in spectra associated to at b_u CH stretch (ν_9) and b_u CH bend (ν_{10}) at low temperatures and for high temperatures with different conditions using the following formula:

$$\boldsymbol{y = y0 + H * \frac{\left(1 + \frac{x - xc}{q * w}\right)^2}{\left(1 + \left(\frac{x - xc}{w}\right)^2\right)}} \quad (16)$$

Where, y0 is (the base /the continuum), xc is the centre or peak position, H is the height or the intensity, w is the width and q is asymmetric parameter.

Based on the fit result (Table 3) for the peak at the b_u CH stretch (ν_9), asymmetry in the underlying continuum shape became noticeable at low temperatures, and peak heights continually diminished with increasing temperature due to the loss of sample through IR heating. However, the peak at the b_u CH bend (ν_{10}) was changeable and almost resolved to three peaks. The suggestion of the isotope splitting into chlorine atoms has been shown in Figure 29.

To understand the behaviour of these peaks, we try to fit all three peaks to the same Fano peak shape parameters with same width, intensity and same q parameter, but it was unsuccessful as it impossible to fit them in the same parameters. The result of three peak as individual parameters under different conditions are shown in Tables 4, 5 and 6 which illustrate clear different behaviours for each of the three peaks that are not due to isotope of chlorine atoms.

[1] OriginPro, Version 2018b.OriginLab Corporation, Northampton, MA, USA.

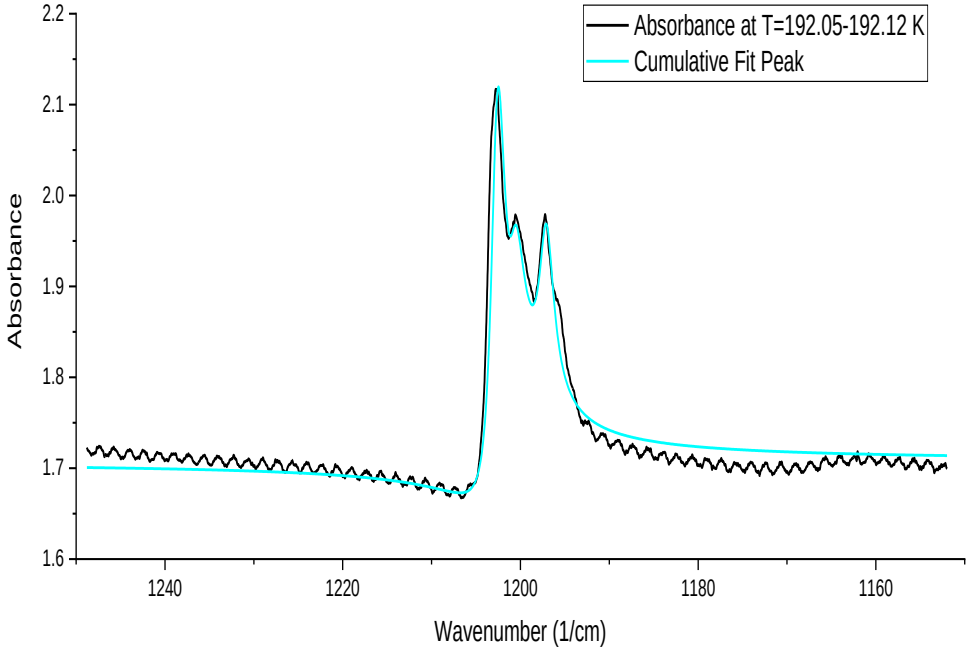

Figure 29 : The peak at 190 K as high temperature (heating), q_1=-4.956, q_2=-2.009 and q_3=-16.117.

T (K)	P (psi) Ar	Peak position (cm^{-1})	Fano parameter	Intensity	Width (cm^{-1})
Cooling +Ar					
200	155.7	3080.959	-2.006	0.100	3.011
180	124.5	3082.098	-1.900	0.087	3.682
150	96.6	3081.119	-1.918	0.091	3.476
120	70.5	3080.954	-1.686	0.089	3.001
Heating +Ar					
148.7-149.45	1.2	3080.950	-1.670	0.080	3.000
Heating without Argon					
179.20-179.45	-	3080.913	-1.800	0.073	3.130
199.60-199.80	-	3078.997	6.998	0.033	4.513
204.84-204.96	-	3078.946	6.977	0.025	4.901
206.02-206.15	-	3078.149	2.986	0.013	5.700

Table 3: Summary of observed peaks of DCE at b_u CH Stretch (ν_9) with Fano Parameter (q), width (W) and the amplitude (H) under different conditions.

T (K)	q (1)	H (1)	W (1)
Cooling + Ar			
200	-3.653	0.142	0.788
120	-3.669	0.179	0.607
Heating +Ar			
148.7-149.5	-3.669	0.175	0.453
Heating without Ar			
179.20-179.45	-3.805	0.164	0.631
199.60-199.8	1.774	-0.090	1.224
204.84-204.96	2.000	0.073	0.699
206.02-206.15	-2.737	-0.033	0.258

Table 4: Summary of observed peaks of DCE at b_u CH bend (ν_{10}) with Fano Parameter (q (1)), width (W (2)) and the amplitude (H (1)) for the peak 1203 cm^{-1} under different conditions.

T (K)	q (2)	H (2)	W (2)
Cooling + Ar			
200	-3.450	0.035	0.990
120	-3.987	0.004	0.067
148.7-149.5	-3.126	0.005	0.232
Heating without Ar			
179.20-179.45	-3.970	0.008	0.397
199.60-199.8	-2.247	0.010	0.498
204.84-204.96	2.000	-0.028	0.396
206.02-206.15	-2.265	0.001	0.002

Table 5: Summary of observed peaks of DCE at b_u CH bend (ν_{10}) with Fano Parameter (q (2)), width (W (2)) and the amplitude (H (2)) for the second peak at 1200 cm^{-1} under different conditions.

T (K)	q (3)	H (3)	W (3)
Cooling + Ar			
200	-6.321	0.060	1.409
120	-3.283	0.098	0.464
Heating without Ar			
148.7-149.5	-4.378	0.102	0.490
Heating without Ar			
179.20-179.45	-4.141	0.084	0.651
199.60-199.8	-1.200	0.030	1.594
204.84-204.96	2.000	-0.029	0.999
206.02-206.15	-2.416	-0.007	0.040

Table 6: Summary of observed peaks of DCE at b_u CH bend (ν_{10}) with Fano Parameter (q (3)), width (W (3)) and the amplitude (H (3)) for the third peak at 1197 cm^{-1} under different conditions.

In following section, we will focus on the b_u CH bend (ν_{10}) peak under heating conditions. Based on fit parameters (Appendix 1), we will study the temperature dependence of the relationships between Fano parameters, i.e., the width, the intensity and the unperturbed continuum absorption for the peaks associated with the b_u CH bend (ν_{10}).

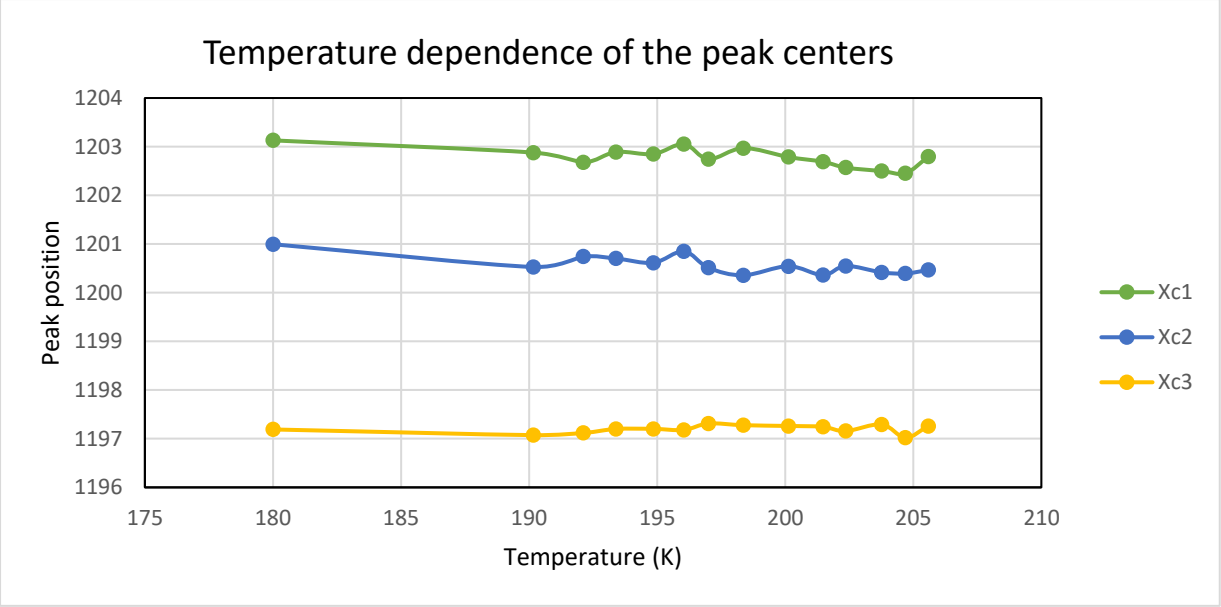

Figure 30 : The relationship between the peak positions with an increase in temperature; Xc1 peak centre for 1203 cm^{-1} , Xc2 for the peak at 1200 cm^{-1} and third for 1197 cm^{-1}.

The peak positions from the fitted curves showed only small shifts around the mean frequencies. The continuum (y0) in this region increased with increasing temperature, while the intensity of the vibrational state of the tDCE molecules at two peaks decreased, indicating that the continuum absorbs the IR as its absorbance is temperature dependent.

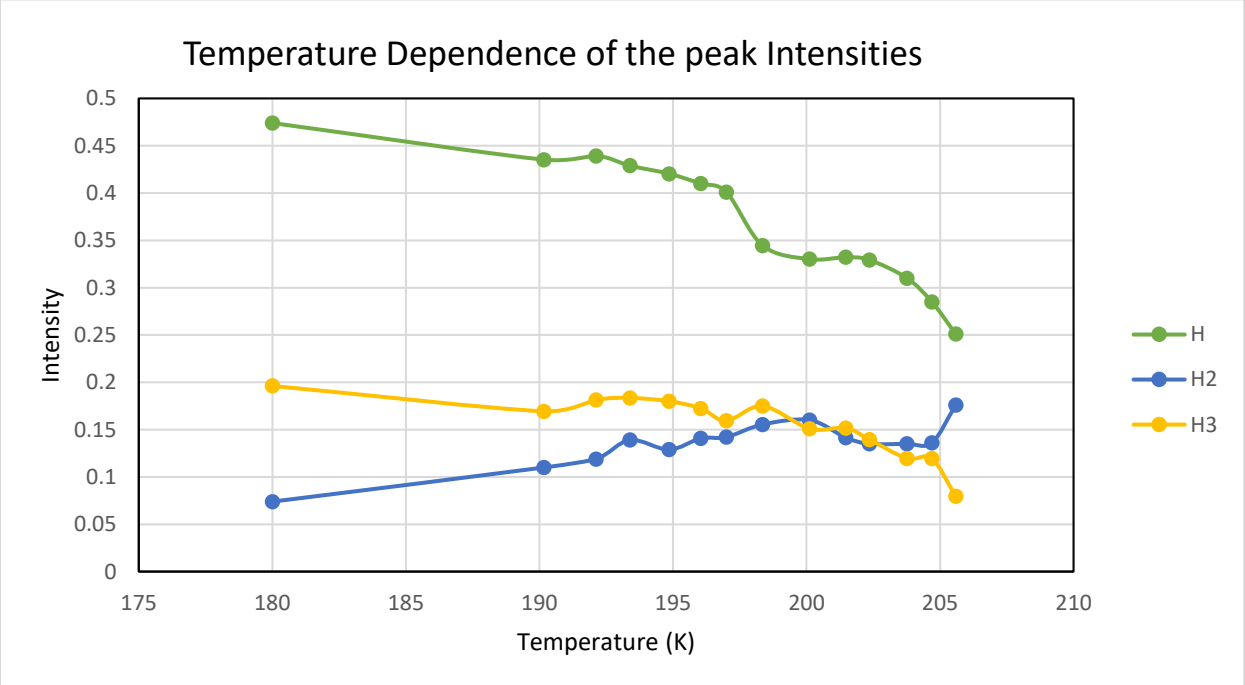

Figure 31: Temperature Dependence of the Peak Intensities: H, H2, and H3 for the peak at 1203, 1200 and 1197 cm^{-1} respectively

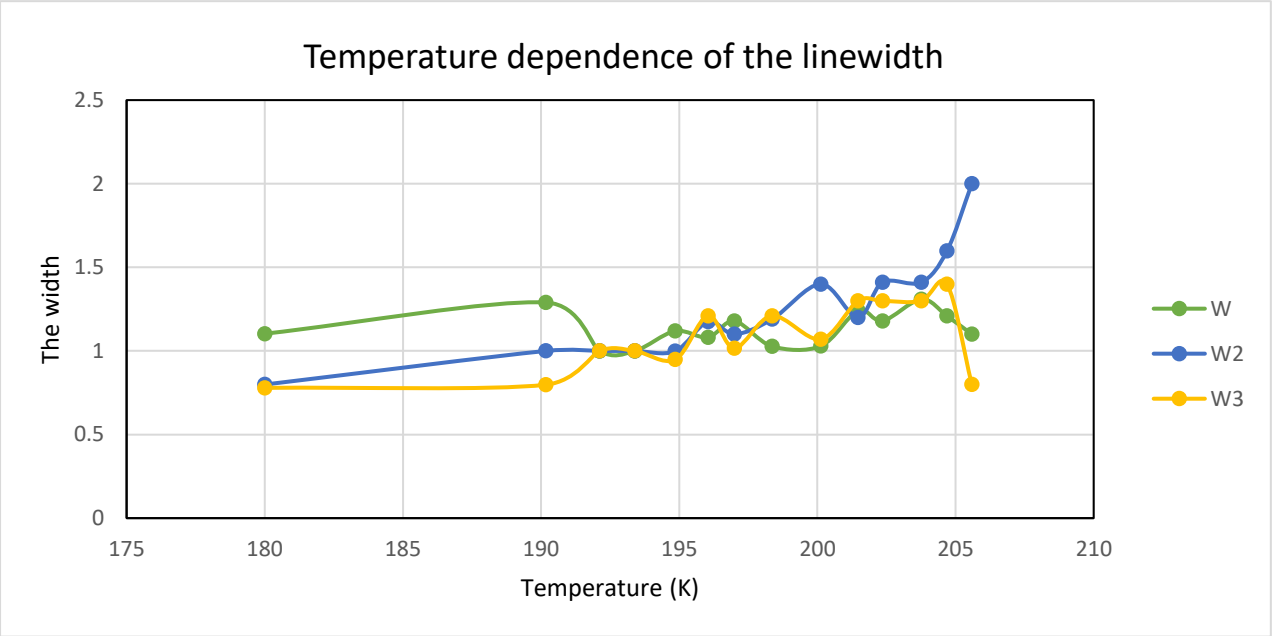

Figure 32 : The linewidth, which is related to the lifetime of the states involved for the b_u CH bend (ν_{10}), as a function of temperature from 180 to 206K, : W, W2, and W3 for the peak at 1203, 1200 and 1197 cm^{-1} respectively

From the fit of the experiment results, the *q* parameter is shown as the ratio of the discrete state to the unperturbed continuum for the 1200 cm^{-1} region. This shows the high probabilities of coupling to the continuum with this band as the value of *q* moves closer to zero with increasing temperatures due to short life time, while the continuum intensity increases.

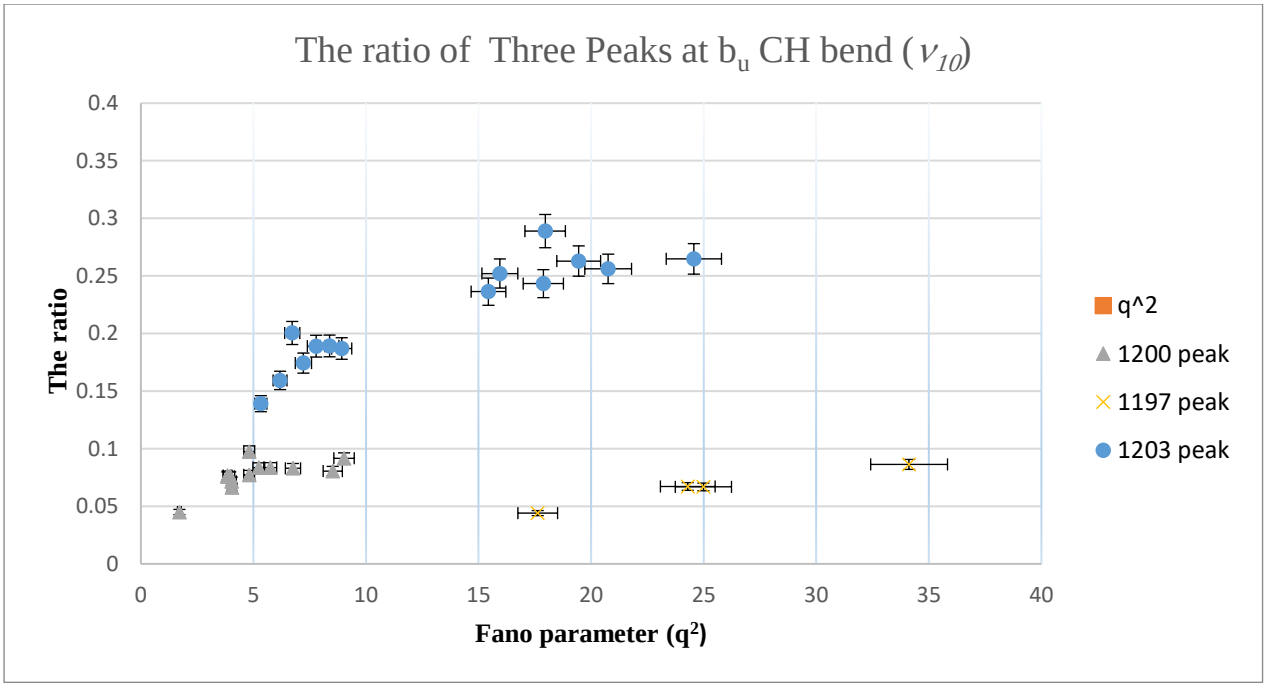

Figure 33 : the ratio of the three component peaks as a function of square of the Fano *q* parameter (q2).

While there are small shifts in the peak position, the intensity and the lifetime (width) of the components of this band increased as temperatures and background continuum absorption increased. The bands are temperature dependent for this peak which suggests the existence of a relationship between the weak hydrogen bonds and the C–H….Cl, so the behaviour for the small component is ignored. The figure 34 demonstrates the peak at 120 K while cooling (non-equilibrium conditions). The molecules are loosely bound and under non-equilibrium conditions, will have a range of energies. Moreover, any change in the cell temperatures (heating or cooling) will affect their low frequency behaviour. They interact with each other or even potentially with the surface, thus affecting the rate of excitation of the low frequency modes, which is highly dependent on the conditions applied as shown in non-equilibrium scans. In this study, the behaviour observed when heating larger crystals shows that the continuum remains mostly in equilibrium as show in Figure 35. The reduction in the strength of coupling to the continuum is attributed to better defined eigenmodes of local

vibrations that couple less intensely to the phonon bands and other modes contributing to the density of states in this energy region.

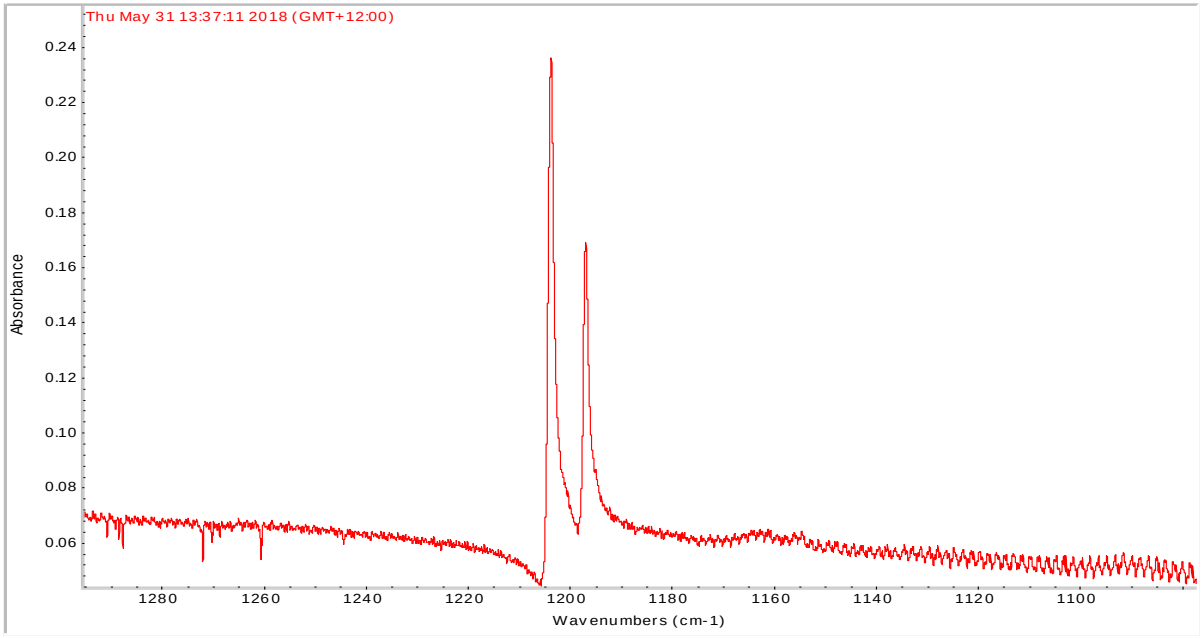

Figure 34 : The peak at low temperature (cooling) T=120 K, q1=-3.669, q2=-3.283 and q3=-3.987.

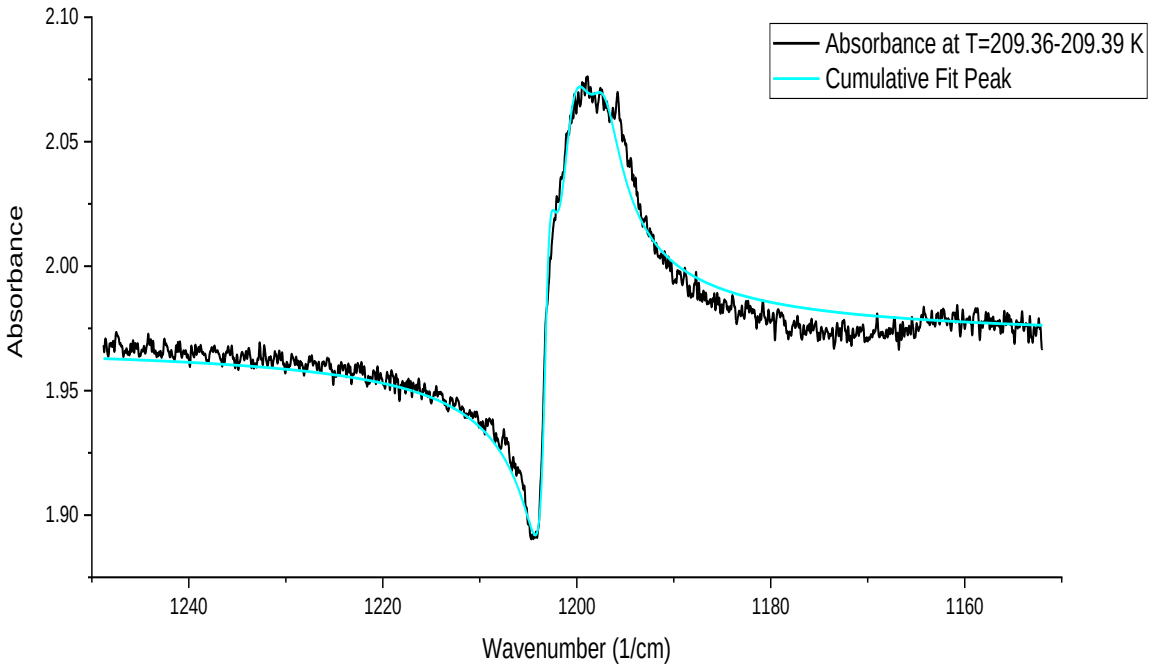

Figure 35 : The peak after the crystal was left overnight q1=-1.480, q2=-1.356, q3=-4.030.

4.4. Simulated spectra for trans 1, 2 dichloroethylene absorption

In this work, we show that the origin of the Fano lineshape in tDCE comes from the discrete vibrational states of tDCE molecules interfering with the continuum of the background transitions in the crystal phase. The continuum arises due to other resonances for the overtone / combination bands, combinations of delocalised vibrations where the molecular inversion symmetry is broken and from coupling between other vibrational states include with the optical phonons. As observed, the *q* parameter shows the coupling between the discrete states and the continuum of background states which have a lower probability of being occupied at lower temperatures under equilibrium conditions. The population of the same energies as the vibrational modes changes with disordered orientations and high temperatures. However, as expected, these effects significantly change for temperatures near the melting point of the crystalline phase.

The crystal structure for tDCE has not been determined, and there have been no experiments to measure the phonon spectra of the molecular crystal. To gain some insight, we studied the vibrational properties for calculated vibrational modes associated with different structures of molecular clusters and the following figure 36 shows a Density functional theory (DFT) model for a two-dimension structure using 19 molecules of DCE.

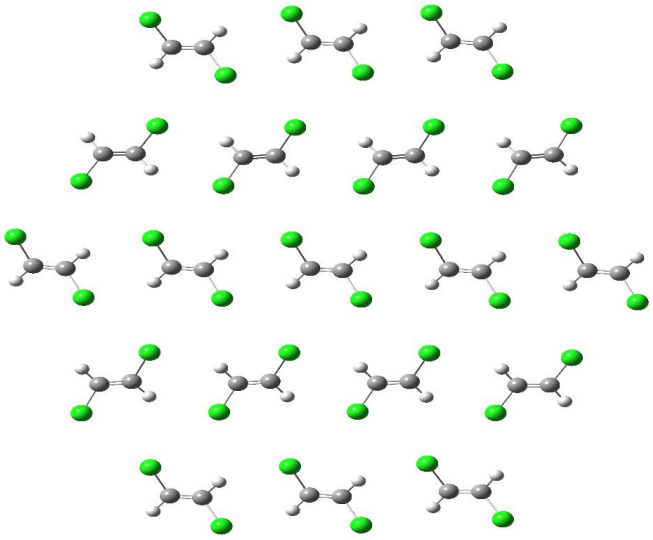

Figure 36 : 2D model structure for the solid DCE

Cartesian coordinate list for the 2-dimensional 19 molecule test structure

Coordinates were

H	9.76655800	7.21909300	0.00000000
C	7.81597700	6.33467200	0.00000000
C	2.08007600	6.21295500	0.00000000
C	3.62521300	6.22795800	0.00000000
C	9.29951700	6.27208800	0.00000000
Cl	6.92456500	7.84099700	0.00000000
Cl	1.27793400	7.76800300	0.00000000
Cl	4.39661400	7.79803500	0.00000000
Cl	10.03068600	7.85663000	0.00000000
H	4.08771400	-6.97873800	0.00000000
H	-1.60253200	-6.95299600	0.00000000
H	-7.26019300	-6.94435100	0.00000000
C	5.00829200	-12.13156500	0.00000000
C	-0.69830900	-12.32858700	0.00000000
C	-6.41169900	-12.37601100	0.00000000
C	6.33996800	-12.15385800	0.00000000
C	0.62981000	-12.42178500	0.00000000

C	-5.08366600	-12.47640900	0.00000000
H	4.37174900	-13.01651700	0.00000000
H	-1.38190800	-13.17767000	0.00000000
H	-7.08795300	-13.23113700	0.00000000
H	6.96668200	-11.26156700	0.00000000
H	1.31279200	-11.57224400	0.00000000
H	-4.39604200	-11.63066500	0.00000000
Cl	4.12717200	-10.61914100	0.00000000
Cl	-1.49517500	-10.77079000	0.00000000
Cl	-7.21071200	-10.82444500	0.00000000
Cl	7.22204600	-13.65899000	0.00000000
Cl	1.42409400	-13.97984100	0.00000000
Cl	-4.29836600	-14.04010900	0.00000000
Cl	10.04516600	-4.82547900	0.00000000
Cl	10.03068600	7.85663000	0.00000000
H	10.00972400	5.44497700	0.00000000
C	10.68260100	-0.05290800	0.00000000
C	12.00598300	-0.20159400	0.00000000
H	9.96749200	-0.87550500	0.00000000
H	12.71543300	0.62617500	0.00000000
Cl	9.94619900	1.53466400	0.00000000
Cl	12.73947800	-1.78514500	0.00000000
C	9.14768400	-6.32146900	0.00000000
C	9.29951700	6.27208800	0.00000000
C	3.40851000	-6.12624200	0.00000000
C	3.62521300	6.22795800	0.00000000
C	-2.29881800	-6.11446200	0.00000000
C	-2.08007600	6.21295500	0.00000000
C	-7.97624500	-6.12261900	0.00000000
C	-7.81597700	6.33467200	0.00000000
H	7.18423500	-5.44628200	0.00000000
H	7.26019300	6.94435100	0.00000000
H	1.39925400	-5.36165900	0.00000000

H	1.60253200	6.95299600	0.00000000
H	-4.32163200	-5.38928600	0.00000000
H	-4.08771400	6.97873800	0.00000000
H	-10.00972400	-5.44497700	0.00000000
H	-9.76655800	7.21909300	0.00000000
C	7.97624500	6.12261900	0.00000000
C	2.29881800	6.11446200	0.00000000
C	-3.40851000	6.12624200	0.00000000
C	-9.14768400	6.32146900	0.00000000
Cl	7.24058100	4.53469000	0.00000000
Cl	1.52439400	4.54573000	0.00000000
Cl	-4.21543400	4.57430200	0.00000000
Cl	-10.04516600	4.82547900	0.00000000
Cl	4.21543400	-4.57430200	0.00000000
Cl	4.39661400	7.79803500	0.00000000
Cl	-1.52439400	-4.54573000	0.00000000
Cl	-1.27793400	7.76800300	0.00000000
Cl	-7.24058100	-4.53469000	0.00000000
Cl	-6.92456500	7.84099700	0.00000000
H	4.32163200	5.38928600	0.00000000
H	-1.39925400	5.36165900	0.00000000
H	-7.18423500	5.44628200	0.00000000
C	5.02068700	0.00619800	0.00000000
C	5.08366600	12.47640900	0.00000000
C	-0.66273300	0.06174900	0.00000000
C	-0.62981000	12.42178500	0.00000000
C	-6.34531700	0.12582400	0.00000000
C	-6.33996800	12.15385800	0.00000000
C	-12.00598300	0.20159400	0.00000000
C	6.34531700	-0.12582400	0.00000000
C	6.41169900	12.37601100	0.00000000
C	0.66273300	-0.06174900	0.00000000
C	0.69830900	12.32858700	0.00000000

C	-5.02068700	-0.00619800	0.00000000
C	-5.00829200	12.13156500	0.00000000
C	-10.68260100	0.05290800	0.00000000
H	4.31290600	-0.82274400	0.00000000
H	4.39604200	11.63066500	0.00000000
H	-1.36545500	-0.77148300	0.00000000
H	-1.31279200	11.57224400	0.00000000
H	-7.05354100	-0.70271400	0.00000000
H	-6.96668200	11.26156700	0.00000000
H	-12.71543300	-0.62617500	0.00000000
H	7.05354100	0.70271400	0.00000000
H	7.08795300	13.23113700	0.00000000
H	1.36545500	0.77148300	0.00000000
H	1.38190800	13.17767000	0.00000000
H	-4.31290600	0.82274400	0.00000000
H	-4.37174900	13.01651700	0.00000000
H	-9.96749200	0.87550500	0.00000000
Cl	4.26989800	1.58613600	0.00000000
Cl	4.29836600	14.04010900	0.00000000
Cl	-1.42409400	1.63682600	0.00000000
Cl	-1.42409400	13.97984100	0.00000000
Cl	-7.09620400	1.70614700	0.00000000
Cl	-7.22204600	13.65899000	0.00000000
Cl	-12.73947800	1.78514500	0.00000000
Cl	7.09620400	-1.70614700	0.00000000
Cl	7.21071200	10.82444500	0.00000000
Cl	1.42409400	-1.63682600	0.00000000
Cl	1.49517500	10.77079000	0.00000000
Cl	-4.26989800	-1.58613600	0.00000000
Cl	-4.12717200	10.61914100	0.00000000
Cl	-9.94619900	1.53466400	-0.00000000

Table 7: Cartesian coordinate list for the two-dimensional 19 molecule test structure, coordinates in Angstroms.

The structure was calculated using density functional theory with B3LYP. B3LYP is Becke's 3 parameter hybrid functional theory that uses non-local correlation from the LYP (Lee Yang Parr) function with VWN functional III for local correlation (B3LYP) (Becke, 1993; Lee, Yang, & Parr, 1988). The standard basis set cc-pVdZ was used and all calculations were performed using Gaussian 09 rev D.01 (Dunning, 1989; Frisch et al., 2013).

This structure was optimized from an initial two-dimensional guess obtained from an optimization using periodic boundary conditions. The z coordinate of all atoms was frozen in the optimization which resulted in 20 negative (imaginary) frequencies associated with the out of plane deformation modes. These frequencies ranged from -8.65 cm^{-1} to -1.17 cm^{-1}. They were calculated using anharmonic approximation with only ^{35}Cl. The complete list of frequencies and associated intensities and eigenvalues can be found in Appendix 2.

Figures 37–42 present the simulated spectra from the two-dimensional 19 molecule fragment. Individual absorptions as indicated by blue vertical lines have been convoluted with a Lorentzian lineshape function with a linewidth of 0.8cm^{-1}. There are many resonances that aren't absorb due to symmetry. They are the dark states, and individual molecular resonances will be split into different states. Based on the symmetry, only half of them will be optically active.

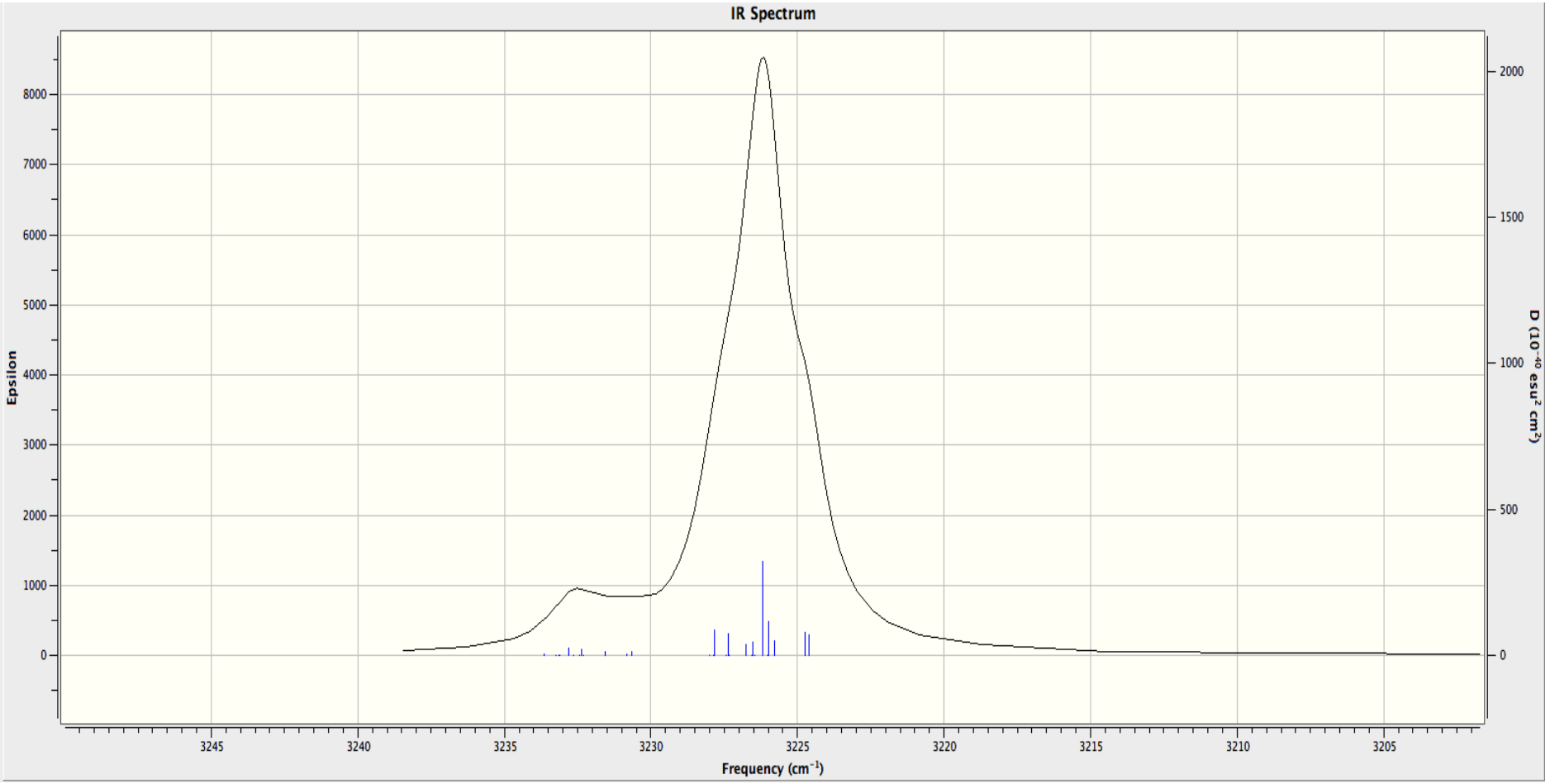

Figure 37 : show simulated spectra for 19 molecule, individual absorptions as indicated by blue vertical lines for tDCE at the peaks associated to at b_u CH stretch (ν_9) and a_g CH stretch (ν_{11}) shown the symmetric and antisymmetric modes can absorb light and all active.

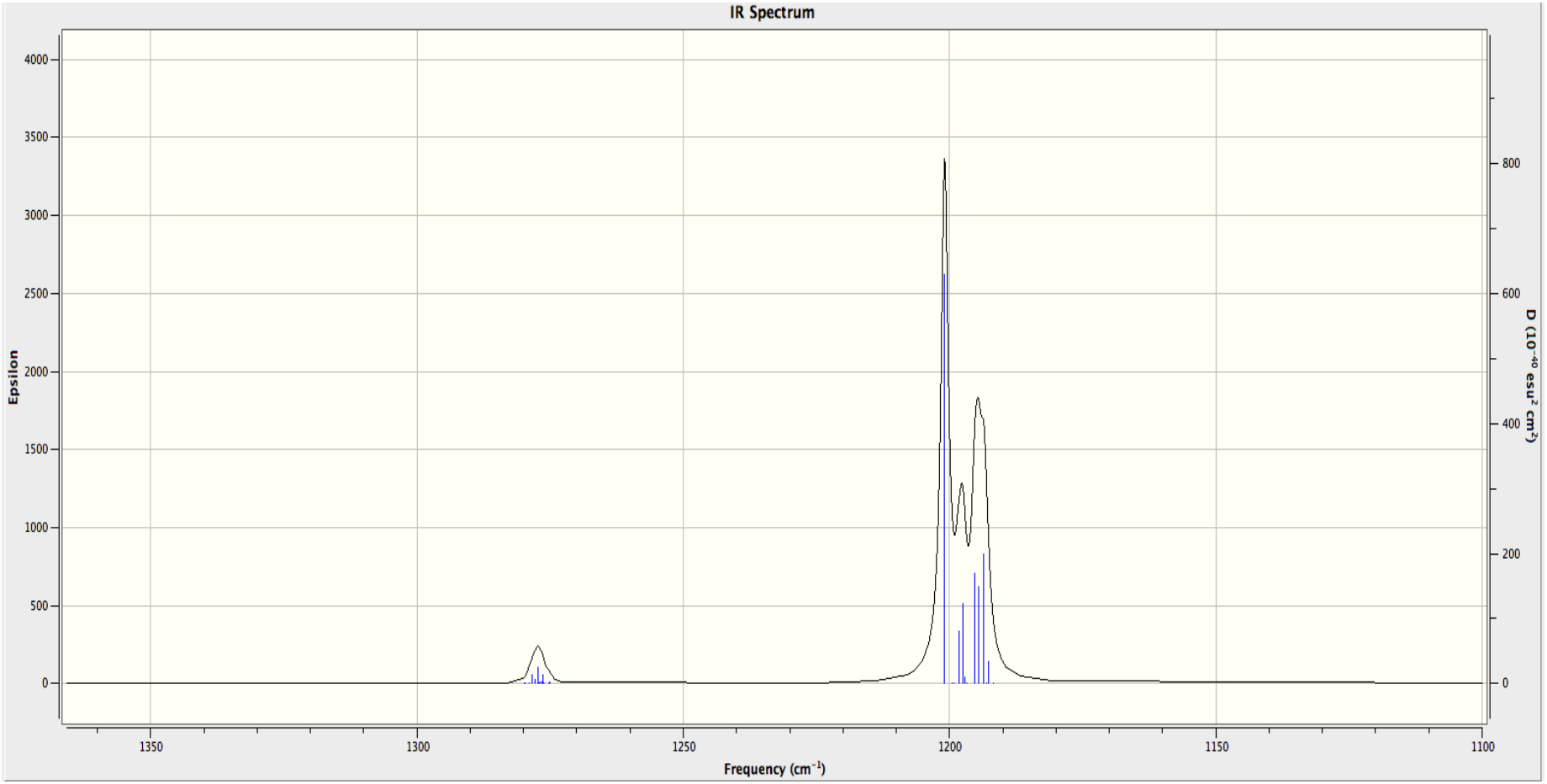

Figure 38 : show the absorbance spectra for tDCE at the peaks associated to the peak at b_u CH bend (ν_{10}) and the peak associated to a_g CH bend (ν_3) which is previously forbidden vibrations and became active due to the delocalisation of the vibration over several molecules.

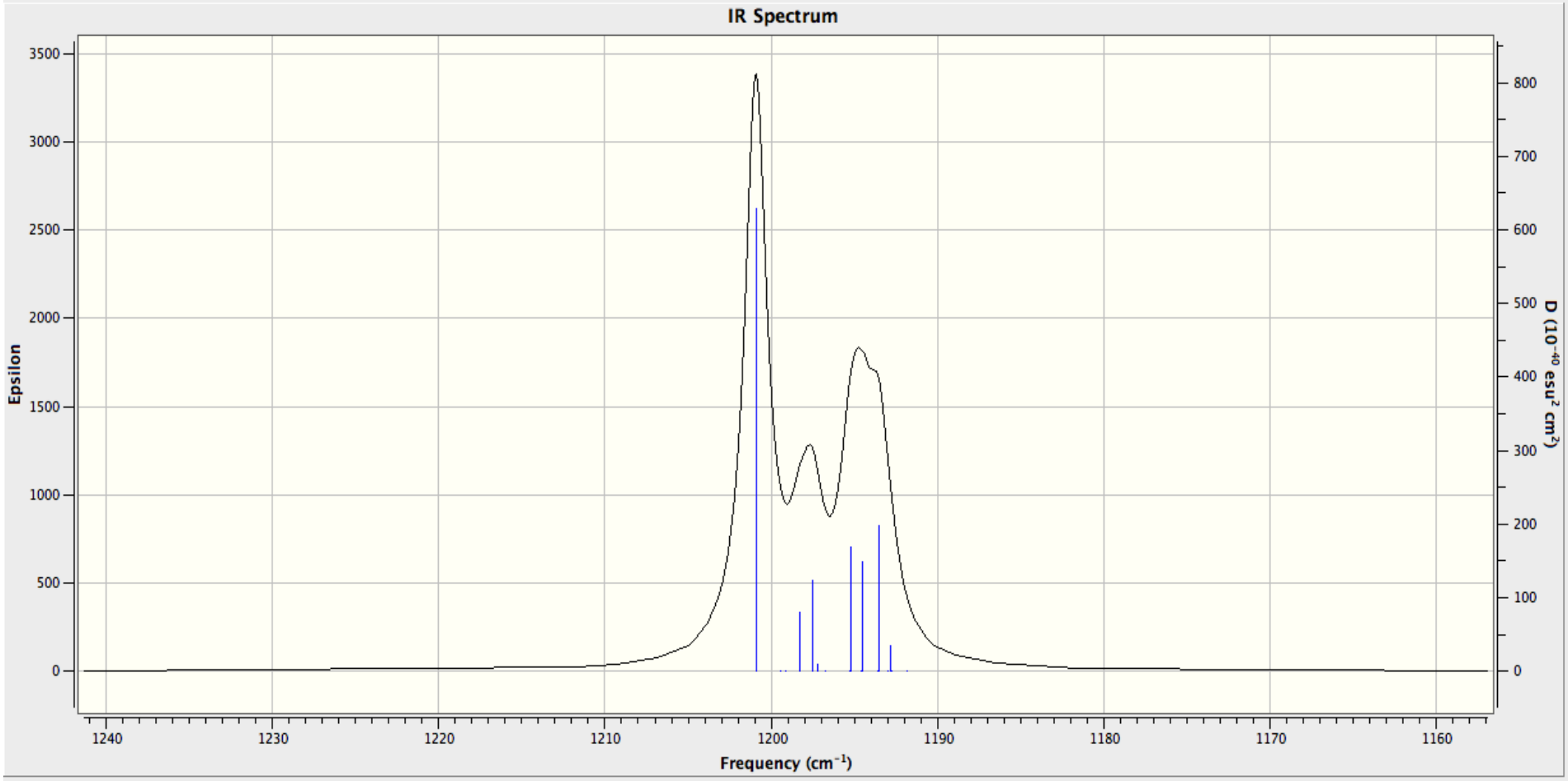

Figure 39 : DCE calculation spectra corresponding to b_u CH bend (ν_{10}), the individual vertical lines indicated individual vibrational resonances that show the large resonance corresponds to one resonance with a continuum, but the other peaks will have more than resonance contributing. That would explain why the *q* are different for each of the peaks.

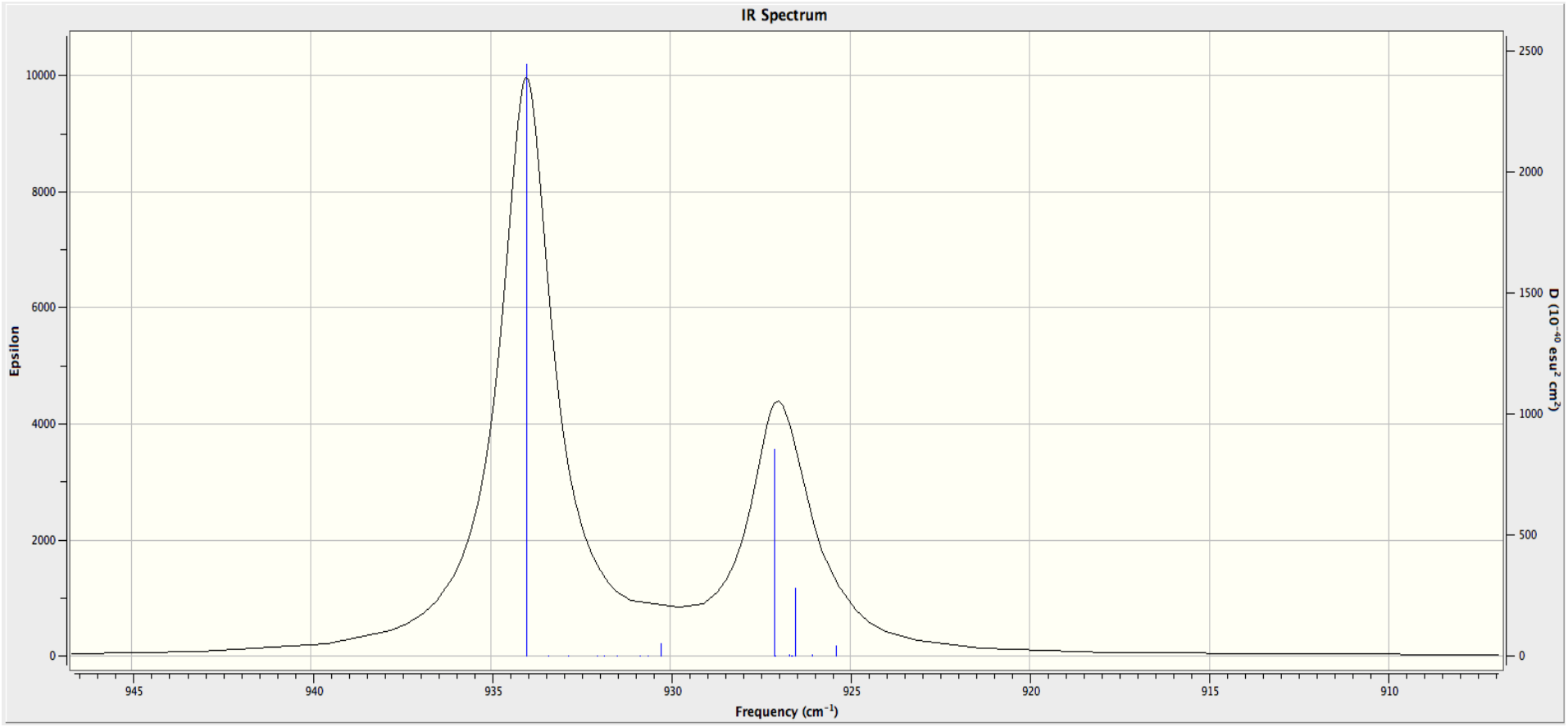

Figure 40 : Simulated spectra for tDCE absorption at the peaks associated to a_u CH bend (ν_6) and the peak split to more peak due to the delocalisation of the vibration over several molecules.

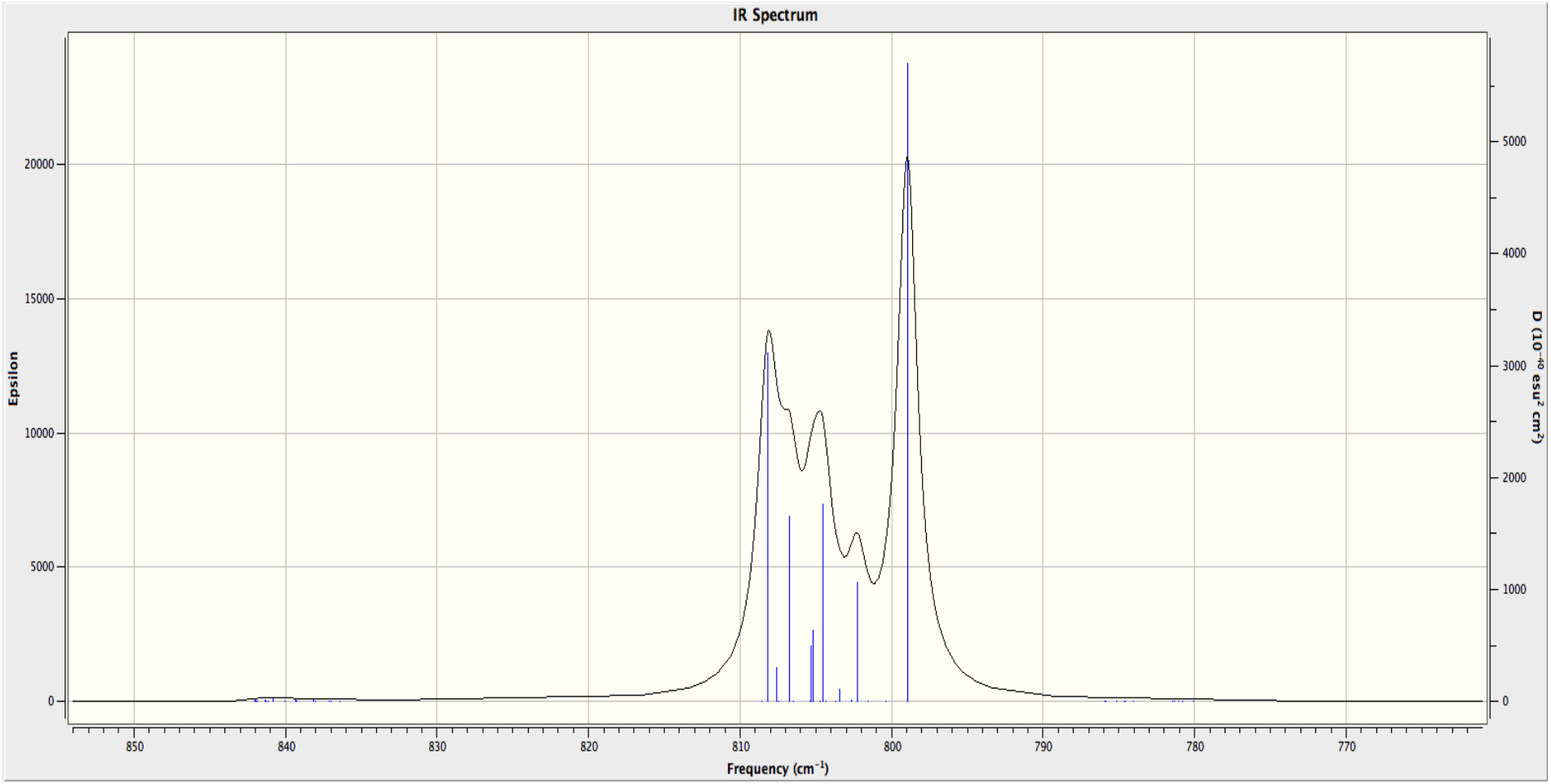

Figure 41 : show simulated absorbance spectra for 19 DCE at b_u CCl stretch (ν_{11}) and smaller absorbance for a_g CCl str (ν_4) at high frequency and b_g CH bend (ν_8) at low frequency, which are as forbidden vibrations which become active in solid phase.

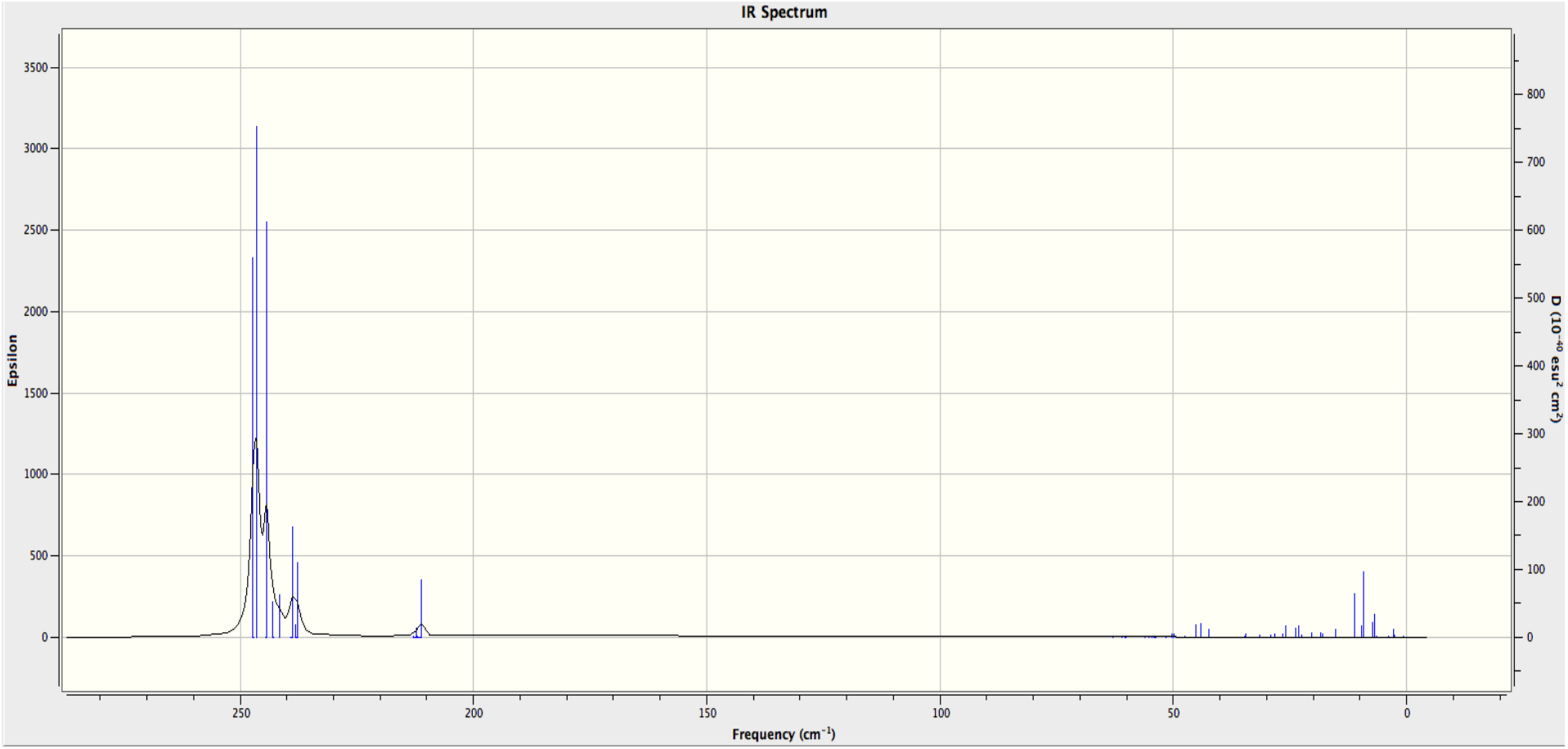

Figure 42 : simulated spectra show very low frequencies absorbance that corresponding to phonon modes and the peak at a_u Torsion (ν_7) and b_u CCCl deform (ν_{12}) modes.

4.5. Argon Matrix Isolated DCE molecules

Ar matrix isolation experiments were conducted at very high dilution (>1:2000 DCE:Ar) to establish the peak origins in an environment where isolated DCE molecules were surrounded by a homogeneous environment of Ar atoms with no continuum.

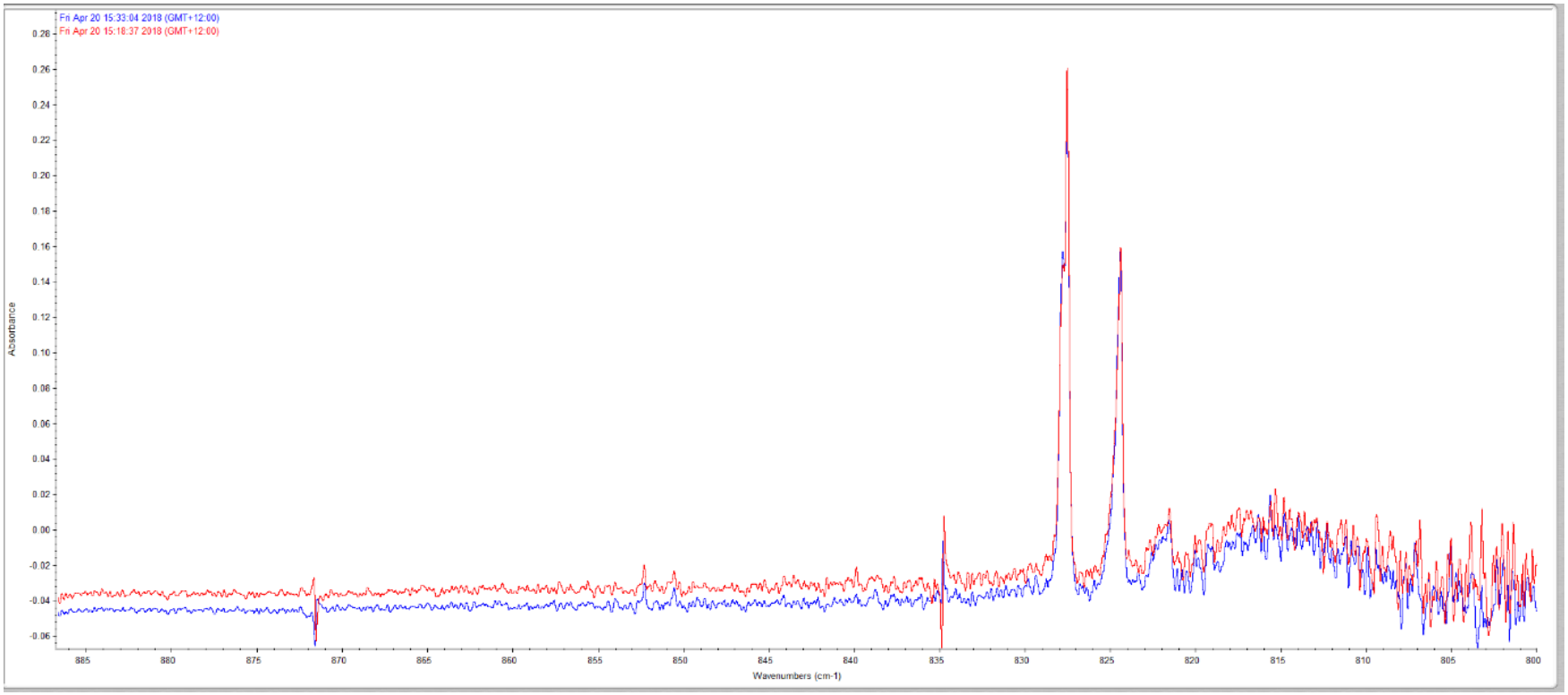

Figure 43 : Red and blue scans are Matrix isolation of DCE molecules at 20 K show the DCE at b_u CCl stretch (ν_{11}) with isotope effects for ^{35}Cl ^{35}Cl : ^{35}Cl ^{37}Cl : ^{37}Cl ^{37}Cl 9:6:1 as expected. Blue with increased Argon.

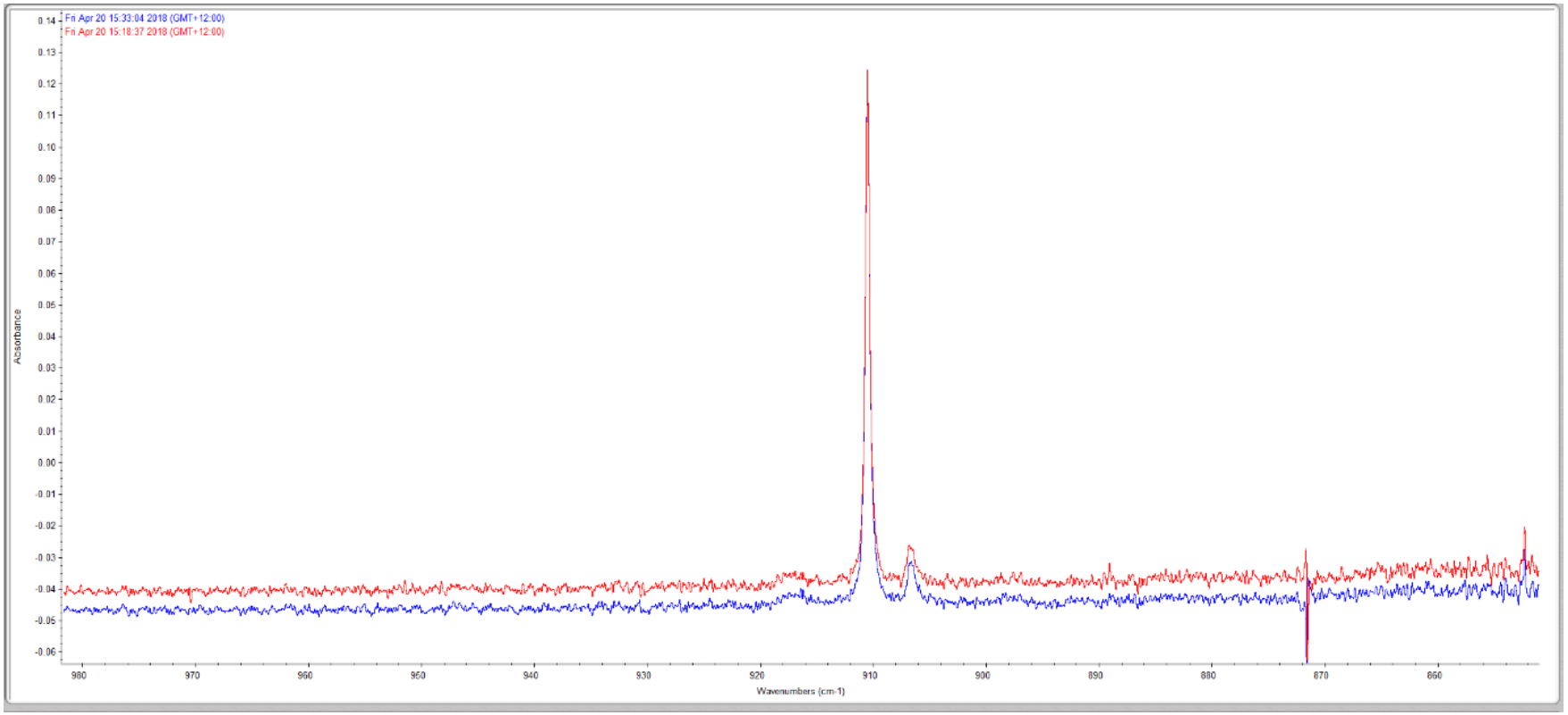

Figure 44 : Red and blue scans are Matrix isolation of DCE show the DCE at CH bend (ν_6) with no isotope effect as expected. Blue with increased deposition time.

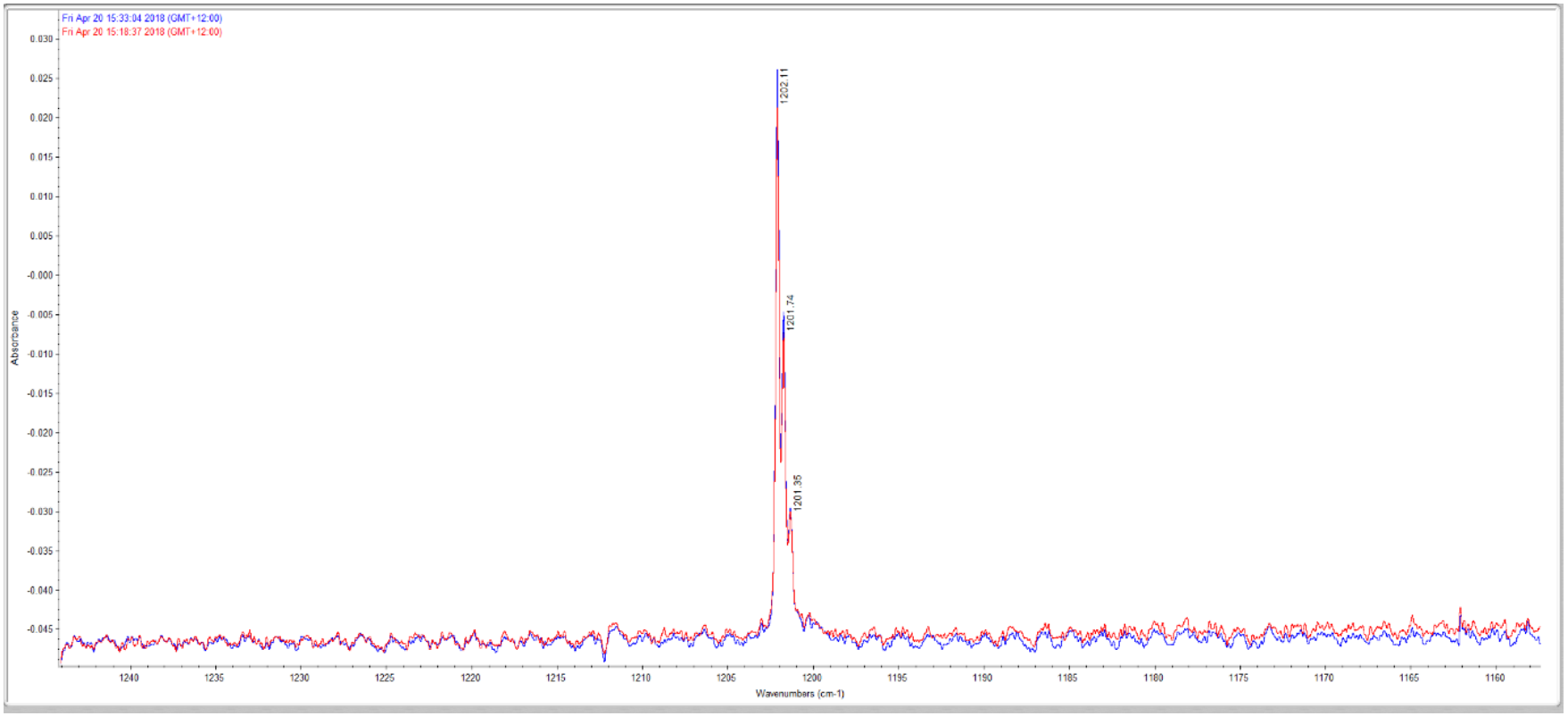

Figure 45 : Red scan is Matrix isolation of DCE at 20 K shows highly resolved CH bend (ν_{10}) for ^{35}Cl ^{35}Cl : ^{35}Cl ^{37}Cl : ^{37}Cl ^{37}Cl 9:6:1 and blue scan corresponding to longer deposition time.

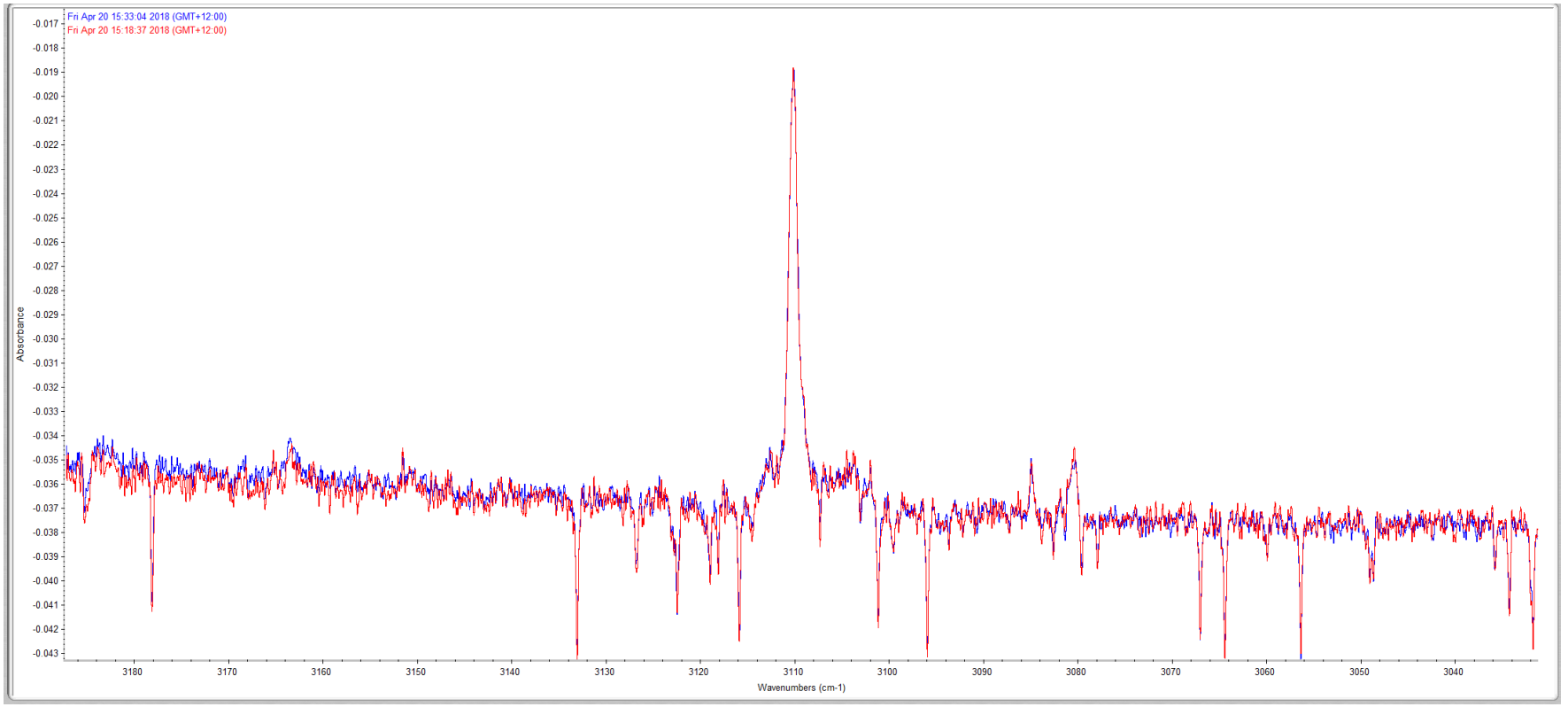

Figure 46 : Red and blue scans are Matrix isolation of DCE at 20 K show the DCE at b_u CH stretch (ν_9) with no isotope effect as expected. Blue with increased deposition time.

Chapter 5: Summary of Results

The vibrational spectra of isolated molecules in the gas phase ranges from small to quite complex molecules. However, in the solid phase, the interactions between the neighbouring molecules due to the weak bonds in the crystalline phase affects the vibrational frequencies (Bakker et al., 2017). Further, IR absorption is observed when there is a change in dipole moment of the molecule. Symmetry considerations reduce the number of allowed IR absorption bands and the absorption does not correspond exactly with the number of fundamental vibrations. In the condensed phase, the local symmetry might break around the interacting molecules or vibrations couple between adjacent molecules such that there are differences in the bands observed in the gas phase and in the solid phase. To give more information on the spectral changes expected from gas to crystal, we studied the vibrational properties of this compound using anharmonic calculations (see Appendix 2 and 3). The anharmonic values for the calculated fundamental bands – infrared energies in cm^{-1} and their intensities – for isolated gas phase molecules at the MP2/cc-pVQZ level theory have been listed for the most abundant isotope ^{35}Cl.

The following table provides the fundamental bands for 12 modes that are obtained from the NIST in gas phase and Argon matrix-isolated DCE molecules (20 K) that have been calculated and experiment in cm^{-1} in gas and solid phase, respectively.

Symmetry			NIST (Gas)	Matrix isolated 20 K	Calculated	Experiment (Solid)
a_g	ν_1	CH str	ia -3070	3104.31	3108.024	3078.215
a_g	ν_2	CC str	ia- 1578	1593.09	1589.872	1569.783
a_g	ν_3	CH bend	ia- 1274	1266.993	1277.144	1268.911
a_g	ν_4	CCl str	ia - 846	873.911	865.617	871.591
a_g	ν_5	CCCl deform	ia - 350	-	355.892	-
a_u	ν_6	CH bend	899.8 VS	910.15	912.987	902.552
a_u	ν_7	Torsion	227 M	-	217.307	-
b_g	ν_8	CH bend	ia -763	-	775.611	-
b_u	ν_9	CH str	3090 S	3110.25	3128.985	3086.91
b_u	ν_{10}	CH bend	1200 S	1202.11	1193.541	1200.33
b_u	ν_{11}	CCl str	828 VS	828	846.878	838.151(!)
b_u	ν_{12}	CCCl deform	250 W	-	240.687	-

Table 8: Infrared value from NIST in gas phase, Matrix isolated, calculated anharmonic Energy in cm^{-1} in and Experiment value cm^{-1} in solid phase. (!) Uncertainty due to noisy both because of the reduced transmittance of the cell due to the window materials and also because of the very intense CCl stretch absorption.

As compared to the solid phase, all the vibrational modes for the observed infrared peaks in this experiment with their intensities as the integrated area and calculation values given for both harmonic and anharmonic values have been quoted in the Appendix 3. As a first approximation, the energy of the transition of the overtone will be n times the fundamental transition in the harmonic oscillator. Further, anharmonic effects reduce the energies of all states to lower values, resulting in lower values even for the fundamental (v = 0 to v = 1) transition than as predicted of a harmonic approximation. As the analysis of

anharmonic and harmonic frequencies demonstrates, the harmonic approximation will be an overestimate of the value for the measured frequencies. Additionally, the estimated values of the anharmonic frequencies are within a few cm^{-1} and generally correspond well with this experiment.

The related peaks for the b_u CH stretch (ν_9), b_u CH bend (ν_{10}), a_u CH bend (ν_6) and b_u CCl stretch (ν_{11}) have been observed directly and the overtone and combination bands are also assigned with the help of the anharmonic calculation (Tables 17 and 18 in Appendix 4).

As shown in Table 8, there is a noticeable difference between the experimental and the calculated frequencies associated with the stretching and bending modes. In fact, the band at 3086 cm-^{1} is assigned to the CH asymmetric stretch. This mode is calculated at 3128 cm^{-1}, and the bending mode is 1193cm^{-1} (expt: 1200 cm^{-1}), 912 cm^{-1} (expt: 902 cm^{-1}) and 846 cm^{-1} (expt: 838 cm^{-1}).

In the gas phase, there are overtone transitions but due to the symmetry, some of them have zero intensity. In the solid phase, with weak bound interactions, certain bands are observed due to the transitions of vibrational fundamentals that are forbidden in the gas phase. These generally contain weaker bands that can be attributed to the effects of breaking symmetry in the crystal. There are evidences of combination bands too. In contrast with the observed and calculated frequencies, most of the calculated frequencies are expected to be larger than the observed ones and corrections to the calculated frequencies to be approximately proportional to the magnitude of frequencies. Moreover, a scaling factor was chosen from the average for the value of observed/calculated frequencies, as shown in Table 9. Additionally, the populated vibrations of the low frequency modes are the major thermal source in condensed matter. Due to the limitations of our detection system in this IR region, we were unable to directly measure these frequencies. Excitation of the low frequency modes

contributed to important physical properties such as the heat capacity and thermal conductivity. Further, with through coupling, they also contributed to the vibrational dynamics of high frequencies at the high energy-level regions at ambient temperature (Zhang, Wang, Tominaga, & Hayashi, 2016).

Experiment (120 K)	Integrated Area	Treated Calculated Frequencies	The difference
3078.215	0.214	3079.018	0.803
3080.91	1.712	3099.784	18.873
1569.783	0.19	1575.035	5.252
1260.911	0.164	1265.225	4.314
1200.33	0.944	1182.402	-17.928
902.552	1.646	904.467	1.914
871.591	0.118	863.457	-8.134
838.151	0.324	830.329	-7.822

Table 9: Experiment value with their IR intensities in solid phase and corrected calculated Energy all in cm^{-1} with the difference related to weak bonds between molecules

In the spectrum at 120 K with equilibrium (Figure 23), for the b_u CH stretching mode vibration and the molecules in the solid state, all the symmetric and antisymmetric modes are absorbent because of the symmetry breaking effects of both coupling to adjacent molecules or mixing with continuum modes. By adding Argon to help establish equilibrium, we can populate the low energy levels, enhance the continuum absorbance in the region of the fundamental absorption peak and consequently establish clear Fano interference in the spectrum with $q = 1$ with a corresponding sharply asymmetric lineshape. There are clear differences in the same spectra between the lineshapes at different molecular absorption regions due to different continuum behaviour at the different spectral regions. In the 1200cm^{-}

^{1} region, it appears that there are partially resolved absorption bands originating from the coupling of motions in nearby molecules. This band is characterized by at least three peaks which are partially resolved. The analysis of the three peaks demonstrates that all three peaks have different widths, intensities and coupling behaviour to the background continuum. The peak splitting is not consistent with the isotope effects as would be expected in the gas phase due to Fermi resonance. While in the spectrum measured at a temperature of 117 K (without Argon present), the scan demonstrated the presence of Fano profiles related to CH bending with approximately the same probability of transition to the background continuum and to the primary peak. The overtone and combination bands are clearly influenced by the background continuum coupling. Under conditions far from equilibrium, the combination and overtones are not apparent presumably due to spectral broadening due to the coupling with the greater number of populated quantum states. Once the thermal equilibrium is established, the bands become apparent, the continuum absorbance drops and the coupling with the fundamental peaks is reduced.

The figure 47 shows the physical nature of the polycrystalline tDCE on one of the windows. The growth of the crystals is largely uncontrolled and can explain why the q parameters gave variable results under different conditions. Concurrent with the hypothesis, the Fano interference is significantly dependent on the crystal thickness, temperature, intensity and the dipole moment orientation.

In this work, we have, for the first time, definitive evidence of discrete state to continuum coupling in a molecular crystal. It has been demonstrated that the coupling depends on the population of the continuum background states, which is influenced by the physical size and structure of the crystal as well as the thermal conditions and rate of energy transfer between the background modes. Currently, there is insufficient knowledge to

simulate the continuum states as required to accurately model the dynamics. Nevertheless, this work might serve as incentive for further studies in this field.

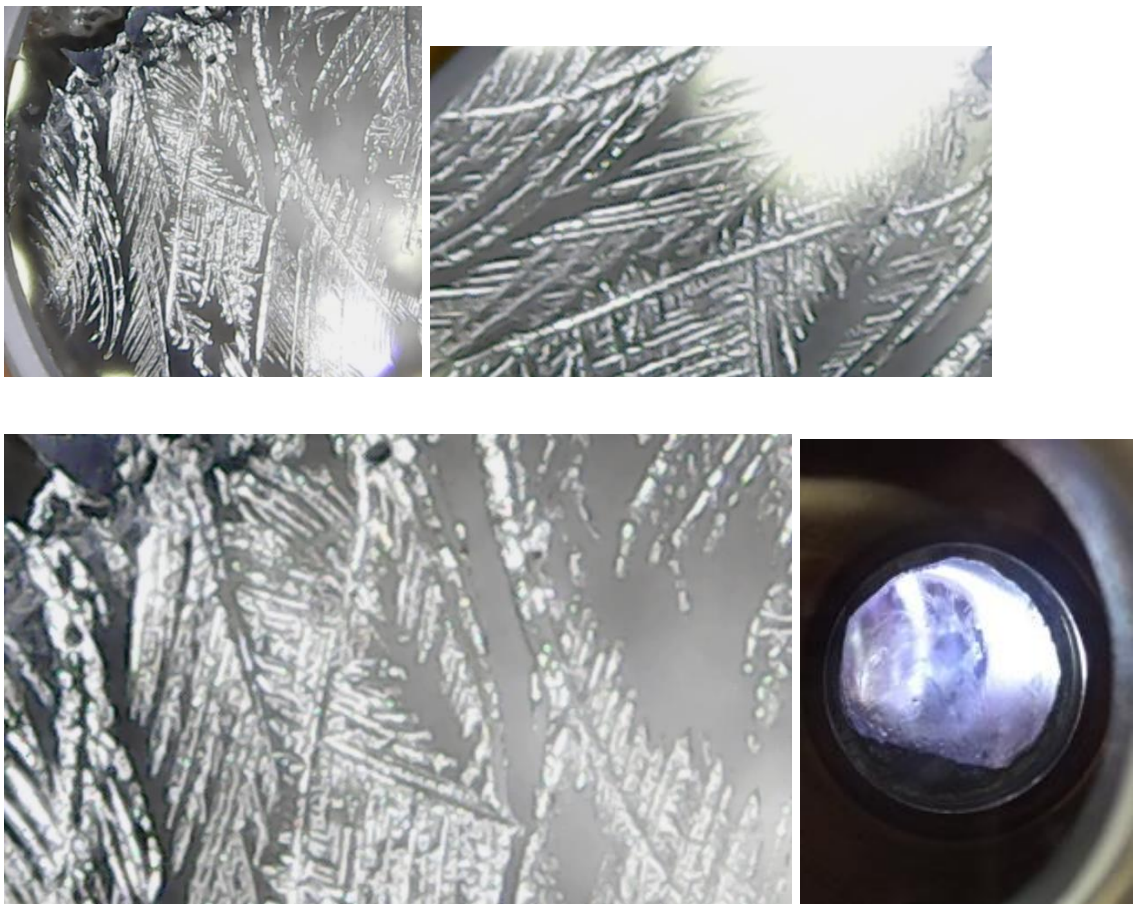

Figure 47: Photographs of DCE crystals on the windows of the cryocell below its freezing point (T=200 K) Top right photograph is approximately 8 mm x 8 mm.

References

Andrews, L., Wang, X., Gong, Y., Kushto, G. P., Vlaisavljevich, B., & Gagliardi, L. (2014). Infrared spectra and electronic structure calculations for nn complexes with U, UN, and NUN in solid argon, neon, and nitrogen. *The Journal of Physical Chemistry A, 118*(28), 5289-5303. doi:10.1021/jp501637j

Babić, L., & de Dood, M. J. A. (2010). Interpretation of Fano lineshape reversal in the reflectivity spectra of photonic crystal slabs. *Optics Express, 18*(25), 26569-26582. doi:10.1364/OE.18.026569

Bakker, D. J., Ong, Q., Dey, A., Mahé, J., Gaigeot, M.-P., & Rijs, A. M. (2017). Anharmonic, dynamic and functional level effects in far-infrared spectroscopy: Phenol derivatives. *Journal of Molecular Spectroscopy, 342*, 4-16. https://doi.org/10.1016/j.jms.2017.02.004

Becke, A. D. (1993). Density-functional thermochemistry. III. The role of exact exchange. *The Journal of Chemical Physics, 98*(7), 5648-5652. 10.1063/1.464913

Bianconi, A. (2003). *Ugo Fano and shape resonances.* Paper presented at the AIP Conference Proceedings.

Cappelluti, E., Benfatto, L., Manzardo, M., & Kuzmenko, A. B. (2012). Charged-phonon theory and Fano effect in the optical spectroscopy of bilayer graphene. *Physical Review B, 86*(11), 115439. doi:10.1103/PhysRevB.86.115439

Chen, M., Tanner, D., & Nino, J. C. J. P. R. B. (2005). Infrared study of the phonon modes in bismuth pyrochlores. *72*(5), 054303. 10.1103/PhysRevB.72.054303

Clark, C. (2001). Effects of configuration interaction on intensities and phase shifts. In (pp. 116-119).

Cohen-Tannoudji, C., Dupont-Roc, J., & Grynberg, G. (1998). *Atom-photon interactions : basic processes and applications*. New York, NYC: Wiley.

Connerade, J. P., & Lane, A. M. (1988). Interacting resonances in atomic spectroscopy. *Reports on Progress in Physics, 51*(11), 1439-1478. 10.1088/0034-4885/51/11/002

Craig, N. C., Appleman, R. A., Barnes, H. E., Morales, E., Smith, J. A., Klee, S., . . . Mellau, G. C. (1998). A Complete Structure of trans-1,2-Dichloroethylene from High-Resolution Infrared Spectroscopy. *The Journal of Physical Chemistry A, 102*(34), 6745-6752. 10.1021/jp981740l

Craig, N. C., & Lacuesta, N. N. (2004). Applications of Group Theory: Infrared and Raman Spectra of the Isomers of 1,2-Dichloroethylene. A Physical Chemistry Experiment. *Journal of Chemical Education, 81*(8), 1199. 10.1021/ed081p1199

Demtröder, W. (2013). *Laser spectroscopy: basic concepts and instrumentation*: Springer Science & Business Media.

Dlott, D. D. (1986). Optical Phonon Dynamics in Molecular Crystals. *Annual Review of Physical Chemistry, 37*(1), 157-187. 10.1146/annurev.pc.37.100186.001105

Dunning, T. H. (1989). Gaussian basis sets for use in correlated molecular calculations. I. The atoms boron through neon and hydrogen. *The Journal of Chemical Physics, 90*(2), 1007-1023. 10.1063/1.456153

Durand, P., Paidarová, I., & Gadéa, F. X. (2001). Theory of Fano profiles. *Journal of Physics B: Atomic, Molecular and Optical Physics, 34*(10), 1953-1966. 10.1088/0953-4075/34/10/310

ETH Zurich. (n.d.). *Pcv - Spectroscopy of atoms and molecules*. Retrieved from https://www.ethz.ch/content/dam/ethz/special-interest/chab/physical-chemistry/ultrafast-spectroscopy-dam/documents/lectures/spectroscopyFS13/scriptFS13/PCV_Ch3.pdf

Fano , U. (1961). Effects of configuration interaction on intensities and phase shifts. *Physical Review, 124*(6), 1866-1878. 10.1103/PhysRev.124.1866

Fano, U., Pupillo, G., Zannoni, A., & Clark, C. (2005). *On the Absorption Spectrum of Noble Gases at the Arc Spectrum Limit* (Vol. 110). 10.6028/jres.110.083

Frisch, M. J., Trucks, G. W., Schlegel, H. B., Scuseria, G. E., Robb, M. A., Cheeseman, J. R., . . . Fox, D. J. (2013). Gaussian 09 Revision. D.01 Wallingford, CT.

Herbert, J. M. (2015). *The Quantum Chemistry of Loosely-Bound Electrons*. Columbus, OH: John Wiley & Sons, Inc.

Holmes, A. (2016). *Combination bands, overtones and fermi resonances*. Retrieved from https://chem.libretexts.org/Bookshelves/Physical_and_Theoretical_Chemistry_Textbook_Maps/Supplemental_Modules_(Physical_and_Theoretical_Chemistry)/Spectroscopy/Vibrational_Spectroscopy/Vibrational_Modes/Combination_Bands%2C_Overtones_and_Fermi_Resonances

Huang, L., Lai, Y.-C., Luo, H.-G., & Grebogi, C. (2015). Universal formalism of Fano resonance. *AIP Advances, 5*(1), 017137. 10.1063/1.4906797

Huang, L., Lambrakos, S. G., & Massa, L. (2017). *Dft calculation of ir absorption spectra for pce-nh2o, tce-nh2o, dce-nh2o, vc-nh2o for small and water-dominated molecular clusters* (NRL Memorandum Report No. NRL/MR/6390--17-9745). Washington, DC: Naval Research Laboratory.

Joe, Y. S., Satanin, A. M., & Kim, C. S. (2006). Classical analogy of Fano resonances. *Physica Scripta, 74*(2), 259-266. 10.1088/0031-8949/74/2/020

Katsumoto, S. (2007). Coherence and spin effects in quantum dots. *Journal of Physics: Condensed Matter, 19*(23), 233201. 10.1088/0953-8984/19/23/233201

Kondratyuk, P. (2005). Analytical formulas for Fermi resonance interactions in continuous distributions of states. *Spectrochimica Acta Part A: Molecular and Biomolecular Spectroscopy, 61*(4), 589-593. https://doi.org/10.1016/j.saa.2004.05.010

Lee, C., Yang, W., & Parr, R. G. (1988). Development of the Colle-Salvetti correlation-energy formula into a functional of the electron density. *Physical Review B, 37*(2), 785-789. 10.1103/PhysRevB.37.785

Li, Z., Lui, C. H., Cappelluti, E., Benfatto, L., Mak, K. F., Carr, G. L., . . . Heinz, T. F. (2012). Structure-Dependent Fano Resonances in the Infrared Spectra of Phonons in Few-Layer Graphene. *Physical Review Letters, 108*(15), 156801. 10.1103/PhysRevLett.108.156801

Limonov, M. F., Rybin, M. V., Poddubny, A. N., & Kivshar, Y. S. (2017). Fano resonances in photonics. *Nature Photonics, 11*(9), 543. doi:10.1038/nphoton.2017.142

Lin, C. D., & Chu, W.-C. (2013). Controlling atomic line shapes. *Science, 340*(6133), 694-695. 10.1126/science.1238396 %J Science

Meierott, S., Hotz, T., Néel, N., & Kröger, J. (2016). Asymmetry parameter of peaked Fano line shapes. *Review of Scientific Instruments, 87*(10), 103901. 10.1063/1.4963678

Merkel, K., Kocot, A., Wrzalik, R., & Ziolo, J. (2008). Origin of the liquid-liquid phase transition for trans-1,2-dichloroethylene observed by IR spectroscopy. *The Journal of Chemical Physics, 129*(7), 074503. 10.1063/1.2968135

Miroshnichenko, A. E., Flach, S., Gorbach, A. V., Luk'yanchuk, B. S., Kivshar, Y. S., & Tribelsky, M. I. (2008). Fano resonances: A discovery that was not made 100 years ago. *Optics and Photonics News, 19*(12), 48-48. 10.1364/OPN.19.12.000048

Miroshnichenko, A. E., Flach, S., & Kivshar, Y. S. (2010). Fano resonances in nanoscale structures. *Reviews of Modern Physics, 82*(3), 2257-2298. 10.1103/RevModPhys.82.2257

Misochko, O., Lebedev, M. J. J. o. E., & Physics, T. (2015). Fano interference at the excitation of coherent phonons: Relation between the asymmetry parameter and the initial phase of coherent oscillations. *120*(4), 651-663.

Palacios, A., Feist, J., González-Castrillo, A., Sanz-Vicario, J. L., & Martín, F. (2013). Autoionization of Molecular Hydrogen: Where do the Fano Lineshapes Go? *ChemPhysChem, 14*(7), 1456-1463. 10.1002/cphc.201200974

Pavithraa, S., Methikkalam, R. R. J., Gorai, P., Lo, J. I., Das, A., Raja Sekhar, B. N., . . . Sivaraman, B. (2017). Qualitative observation of reversible phase change in astrochemical ethanethiol ices using infrared spectroscopy. *Spectrochimica Acta Part A: Molecular and Biomolecular Spectroscopy, 178*, 166-170. https://doi.org/10.1016/j.saa.2017.01.023

Ray, S. K., Chandel, S., Singh, A. K., Kumar, A., Mandal, A., Misra, S., . . . Ghosh, N. (2017). Polarization-tailored Fano interference in plasmonic crystals: A mueller matrix model of anisotropic Fano resonance. *ACS Nano, 11*(2), 1641-1648. 10.1021/acsnano.6b07406

Sathyanarayana, D. N. (2015). *Vibrational spectroscopy: theory and applications*. New Delhi, India New Age International (P) Ltd.

Shimanouchi, T. (1972). Ethylene, 1,2-dichloro-, (E)-. Retrieved from https://webbook.nist.gov/cgi/cbook.cgi?ID=C156605&Mask=800#Refs

Zangeneh-Nejad, F., & Fleury, R. (2019). Topological Fano Resonances. *Physical Review Letters, 122*(1), 014301. 10.1103/PhysRevLett.122.014301

Zhang, F., Wang, H.-W., Tominaga, K., & Hayashi, M. (2016). Characteristics of Low-Frequency Molecular Phonon Modes Studied by THz Spectroscopy and Solid-State ab Initio Theory: Polymorphs I and III of Diflunisal. *The Journal of Physical Chemistry B, 120*(8), 1698-1710. 10.1021/acs.jpcb.5b08798

Appendix 1

Fit parameters of the experimental data at b_u CH bend (v_{10}) of the crystalline spectrum at high Temperatures.

T (K)	The continuum	Peak position	Intensity	Width	q Fano parameter	q2	Modified state/Continuum
180	1.64061	1203.12987	0.47402	1.10303	-4.23776	17.95861	0.288929118
190.17	1.65543	1202.87893	0.43529	1.28975	-4.40998	19.44792	0.262946787
192.12	1.65907	1202.67981	0.43935	0.99988	-4.95599	24.56184	0.264817036
193.39	1.67474	1202.8909	0.42895	0.99988	-4.55599	20.75704	0.25612931
194.85	1.66759	1202.84899	0.42044	1.11882	-3.99319	15.94557	0.252124323
196.04	1.68555	1203.05501	0.41011	1.08111	-4.22783	17.87455	0.243309306
197.00	1.69699	1202.7432	0.40108	1.17845	-3.92929	15.43932	0.236347887
198.36	1.71845	1202.97056	0.34449	1.02786	-2.59292	6.723234	0.200465536
200.12	1.74471	1202.78789	0.33016	1.02905	-2.89459	8.378651	0.189234887
201.47	1.75693	1202.69079	0.33216	1.24124	-2.78966	7.782203	0.189057048
202.36	1.7609	1202.57079	0.32926	1.17972	-2.98676	8.920735	0.186983929
203.76	1.77875	1202.4997	0.31016	1.30879	-2.68676	7.218679	0.174369642
204.69	1.78939	1202.45524	0.28506	1.20879	-2.48612	6.180793	0.159305685
205.59	1.80439	1202.79589	0.25096	1.09979	-2.30882	5.33065	0.139083014

Table 10: fit parameters for experiment data at 1203 peak as function of increasing temperature.

T (K)	The continuum	Peak position	Intensity	Width	q Fano parameter	q^2	Modified state/continuum
180	1.64061	1200.99577	0.07388	0.79909	-1.30752	1.709609	0.04503203
190.17	1.65543	1200.52846	0.10999	0.99998	-2.01126	4.045167	0.06644195
192.12	1.65907	1200.74229	0.11899	0.99997	-2.00911	4.036523	0.0717209
193.39	1.67474	1200.70245	0.13899	0.99997	-2.59911	6.755373	0.08299199
194.85	1.66759	1200.61563	0.12888	0.99865	-2.19319	4.810082	0.07728518
196.04	1.68555	1200.85088	0.14082	1.17578	-2.28896	5.239338	0.08354543
197	1.69699	1200.51307	0.14206	1.09999	-2.39688	5.745034	0.08371293
198.36	1.71845	1200.35771	0.15549	1.18955	-6.98754	48.82572	0.0904827
200.12	1.74471	1200.54418	0.16008	1.39997	-3.00398	9.023896	0.09175164
201.47	1.75693	1200.36077	0.14163	1.19992	-2.91919	8.52167	0.0806122
202.36	1.7609	1200.5496	0.13503	1.41024	-1.96174	3.848424	0.07668238
203.76	1.77875	1200.4181	0.13503	1.41024	-1.96174	3.848424	0.07591286
204.69	1.78939	1200.39404	0.13603	1.59794	-1.99174	3.967028	0.07602032
205.59	1.80439	1200.46691	0.17603	1.99994	-2.19394	4.813373	0.09755651

Table 11: fit parameters for experiment data at 1200 peak as function of increasing temperature.

T (K)	The continuum	Peak position	Intensity	Width	q Fano parameter	q^2	Modified state/continuum
180	1.64061	1197.19018	0.19621	0.77909	-10.68612	114.1931607	0.1195958
190.17	1.65543	1197.07375	0.16937	0.79784	-17.93099	321.5204024	0.1023118
192.12	1.65907	1197.11889	0.18149	0.99997	-16.11711	259.7612348	0.1093926
193.39	1.67474	1197.19998	0.18353	0.99997	-18.9971	360.8898084	0.1095872
194.85	1.66759	1197.20224	0.17999	0.94835	-19.8606	394.4434324	0.1079342
196.04	1.68555	1197.18047	0.17247	1.20966	-15.88896	252.4590499	0.1023227
197	1.69699	1197.31248	0.15936	1.01702	-7.7622	60.25174884	0.0939074
198.36	1.71845	1197.2778	0.17498	1.20934	-8.94997	80.101963	0.1018243
200.12	1.74471	1197.26208	0.15096	1.06989	-9.62882	92.71417459	0.0865244
201.47	1.75693	1197.24443	0.15173	1.29878	-5.84149	34.12300542	0.0863609
202.36	1.7609	1197.15695	0.13954	1.29899	-6.91862	47.8673027	0.0792436
203.76	1.77875	1197.29464	0.11954	1.29899	-4.92855	24.2906051	0.0672045
204.69	1.78939	1197.02194	0.11954	1.39899	-4.99855	24.9855021	0.0668049
205.59	1.80439	1197.26197	0.07954	0.79899	-4.19855	17.6278221	0.0440814

Table 12: fit parameters for experiment data at 1197 peak as function of increasing temperature.

Fit parameters of the experimental data at b_u CH bend (ν_{10}) of the crystalline spectrum at high Temperatures with growth crystal.

T(K)	The continuum	Peak position	Intensity	Width	q Fano parameter	q^2	Modified state/continuum
201.61	1.89328	1203.46561	0.08339	1.00089	-1.00101	1.002021	0.044045255
203.53	1.88111	1203.46561	0.083339	1.00989	-1.00901	1.018101	0.044303098
205.43	1.88005	1203.37182	0.08339	1.00989	-1.05901	1.121502	0.044355203
206.65	1.89031	1203.30961	0.07599	1.01088	-1.05001	1.102521	0.040199756
207.12	1.8874	1203.34904	0.08339	1.00989	-1.15001	1.322523	0.044182473
208.47	1.88895	1203.33813	0.08105	0.70145	-1.27932	1.63666	0.042907435
209.39	1.89079	1203.15094	0.08466	0.80289	-1.48001	2.19043	0.044774935
210.39	1.88899	1203.29094	0.07466	0.70104	-1.30999	1.716074	0.039523767
211.44	1.88292	1203.20494	0.06999	0.60104	-1.22999	1.512875	0.03717099
212.18	1.89037	1203.33515	0.05009	0.79961	-1.19889	1.437337	0.026497458
213.1	1.88375	1203.69515	0.03241	0.32261	-1.20923	1.462237	0.017205043
214.03	1.88065	1203.79931	0.03241	0.39226	-1.10092	1.212025	0.017233403
215.03	1.87477	1203.64089	0.03241	0.20923	-1.29099	1.666655	0.017287454
216.26	1.8682	1203.62089	0.02241	0.20923	-1.19899	1.437577	0.011995504

Table 13: fit parameters for experiment data with growth crystal at 1203 peak as function of increasing temperature

T (K)	The continuum	Peak position	Intensity	Width	q Fano parameter	q^2	Modified state/continuum
201.61	1.89328	1201.49439	0.05773	1.09899	-1.27431	1.623866	0.03049206
203.53	1.88111	1201.39439	0.05773	1.09899	-1.27431	1.623866	0.03068933
205.43	1.88005	1201.22221	0.05773	1.09899	-1.27431	1.623866	0.03070663
206.65	1.89031	1201.04377	0.05761	1.99865	-1.45622	2.120577	0.03047648
207.12	1.8874	1201.06673	0.05761	1.99865	-1.45622	2.120577	0.03052347
208.47	1.88895	1201.04288	0.06823	1.90874	-1.40534	1.974981	0.0361206
209.39	1.89079	1201.04872	0.06971	1.92335	-1.35622	1.839333	0.03686819
210.39	1.88899	1201.04872	0.06501	1.60335	-1.49622	2.238674	0.03441522
211.44	1.88292	1201.04872	0.05901	1.60335	-1.59622	2.547918	0.03133962
212.18	1.89037	1201.14872	0.05701	1.20335	-1.69622	2.877162	0.03015812
213.1	1.88375	1201.29872	0.07001	1.99335	-1.51622	2.298923	0.03716523
214.03	1.88065	1201.33711	0.06099	1.19935	-1.89622	3.59565	0.03243028
215.03	1.87477	1201.37711	0.05999	1.24935	-1.89622	3.59565	0.03199859
216.26	1.8682	1201.20711	0.07005	1.24935	-2.89622	8.38809	0.03749599

Table 14: fit parameters for experiment data with growth crystal at 1201 peak as function of increasing temperature

T (K)	The continuum	Peak position	Intensity	Width	q Fano parameter	q^2	Modified state/continuum
201.61	1.89328	1197.30224	0.06349	1.99933	-4.97625	24.76306406	0.0335344
203.53	1.88111	1197.46224	0.06349	1.99933	-4.97625	24.76306406	0.0337513
205.43	1.88005	1197.24235	0.06349	1.99933	-4.03625	16.29131406	0.0337704
206.65	1.89031	1197.18351	0.04421	2.01102	-6.03813	36.4590139	0.0233877
207.12	1.8874	1197.15951	0.04421	1.99933	-4.03825	16.30746306	0.0234238
208.47	1.88895	1197.35707	0.04041	1.99952	-4.03543	16.28469528	0.0213928
209.39	1.89079	1197.42196	0.03591	1.92335	-4.03012	16.24186721	0.0189921
210.39	1.88899	1197.46096	0.04001	1.82335	-4.03012	16.24186721	0.0211806
211.44	1.88292	1196.96096	0.05001	1.92335	-4.03012	16.24186721	0.0265598
212.18	1.89037	1197.12962	0.06001	1.95935	-4.03012	16.24186721	0.0317451
213.1	1.88375	1197.29962	0.04601	1.85935	-4.03012	16.24186721	0.0244247
214.03	1.88065	1197.55998	0.06601	1.80935	-4.03012	16.24186721	0.0350996
215.03	1.87477	1197.60998	0.06601	1.85935	-4.03012	16.24186721	0.0352097
216.26	1.8682	1197.65998	0.06901	1.85935	-4.03012	16.24186721	0.0369393

Table 15: fit parameters for experiment data with big crystal at 1197 peak as function of increasing the temperature.

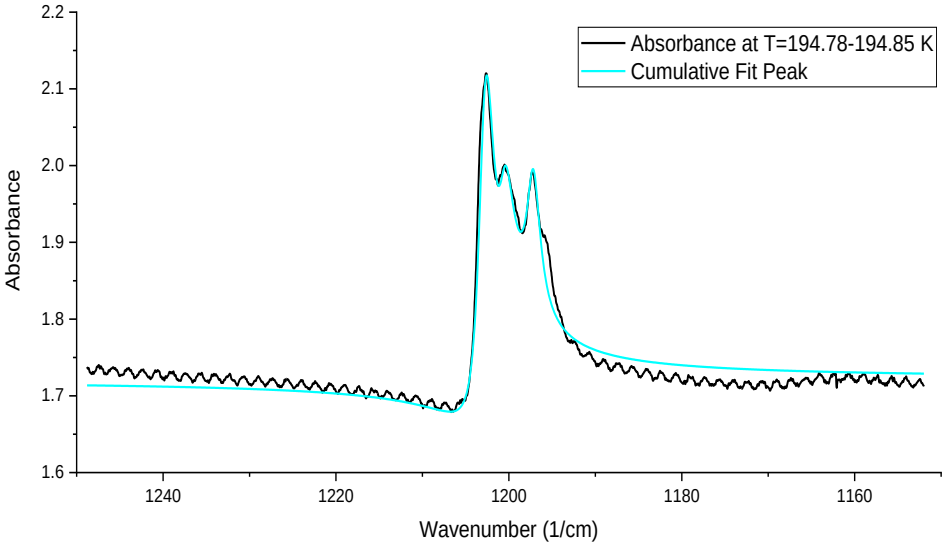
Absorbance at T=194.78-194.85 K
Cumulative Fit Peak
Absorbance
Wavenumber (1/cm)
2.2
2.1
2.0
1.9
1.8
1.7
1.6
1240
1220
1200
1180
1160

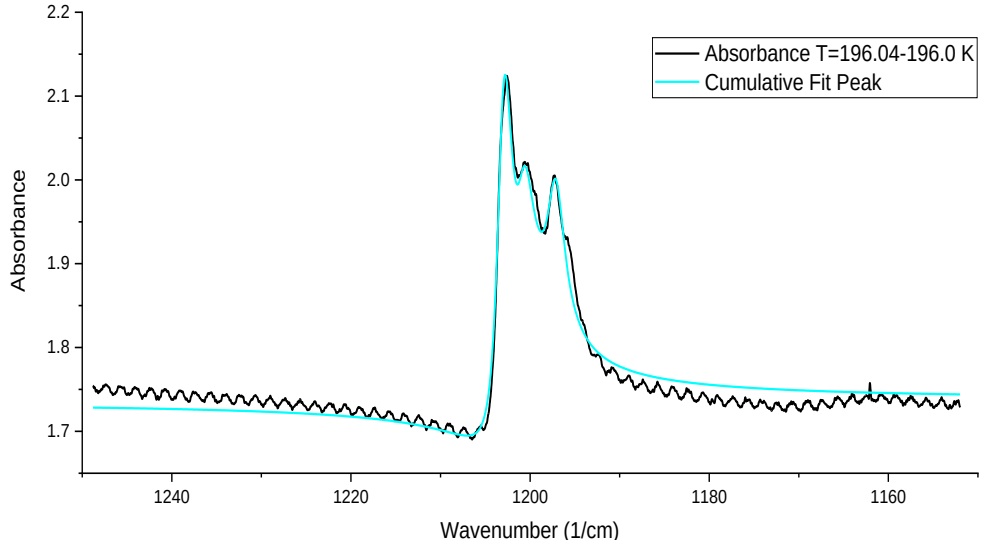
Absorbance T=196.04-196.0 K
Cumulative Fit Peak
Absorbance
Wavenumber (1/cm)
2.2
2.1
2.0
1.9
1.8
1.7
1240
1220
1200
1180
1160

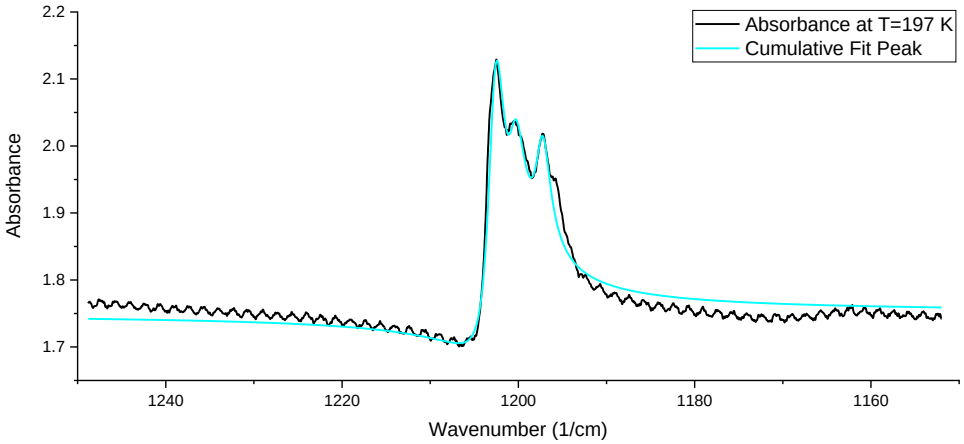
Absorbance at T=197 K
Cumulative Fit Peak
Absorbance
2.2
2.1
2.0
1.9
1.8
1.7
1240
1220
1200
1180
1160
Wavenumber (1/cm)

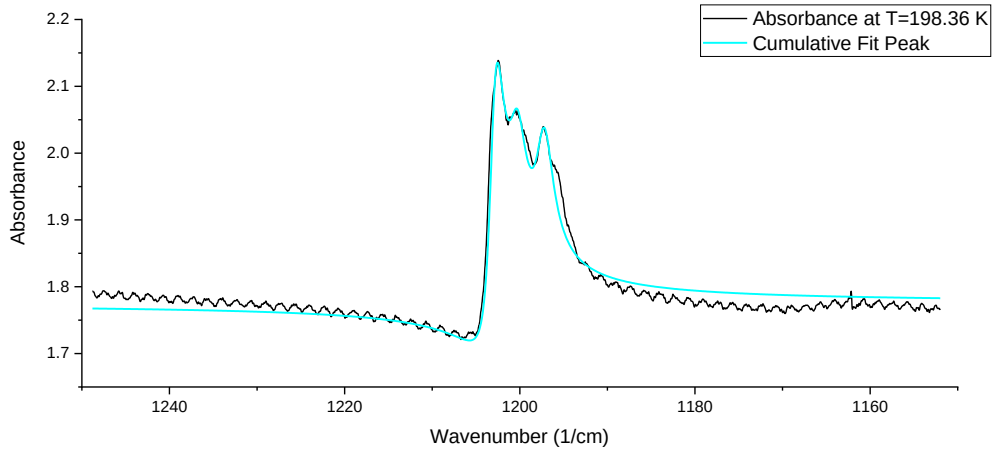
Absorbance at T=198.36 K
Cumulative Fit Peak
Absorbance
2.2
2.1
2.0
1.9
1.8
1.7
1240
1220
1200
1180
1160
Wavenumber (1/cm)

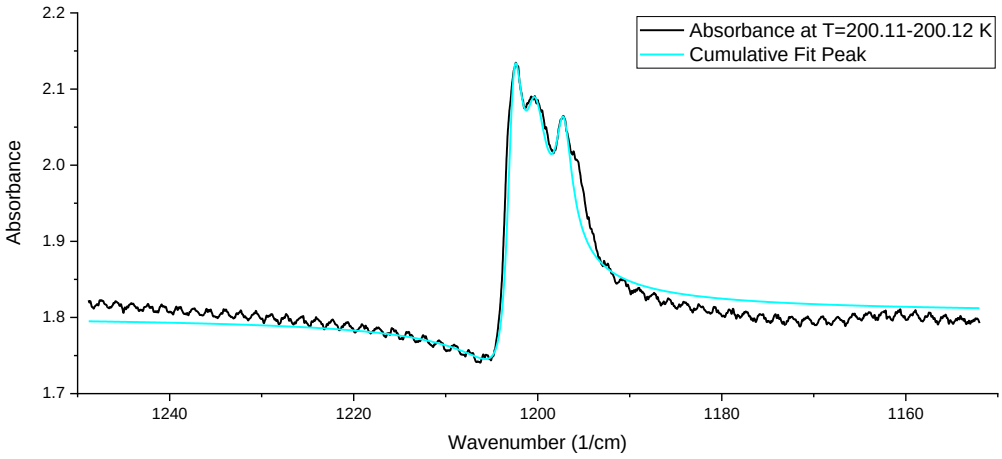
Absorbance at T=200.11-200.12 K
Cumulative Fit Peak
Absorbance
2.2
2.1
2.0
1.9
1.8
1.7
1240
1220
1200
1180
1160
Wavenumber (1/cm)

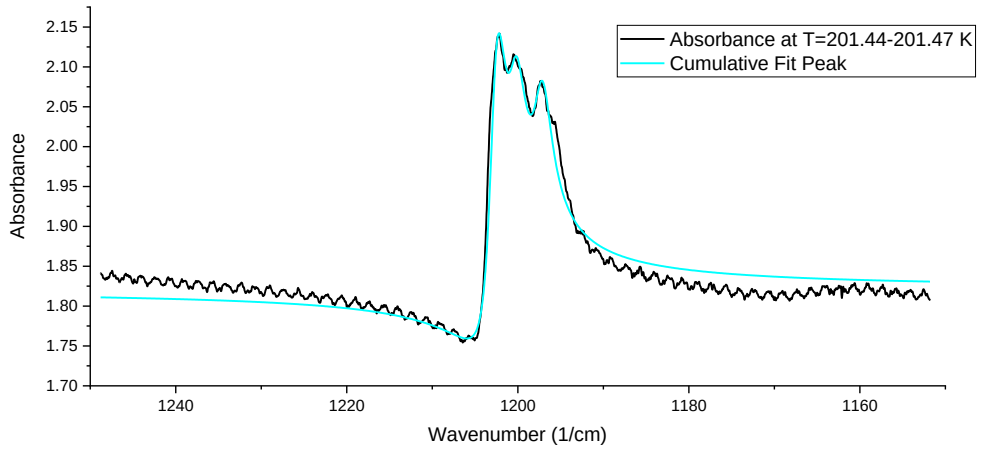
Absorbance at T=201.44-201.47 K
Cumulative Fit Peak
Absorbance
2.15
2.10
2.05
2.00
1.95
1.90
1.85
1.80
1.75
1.70
1240
1220
1200
1180
1160
Wavenumber (1/cm)

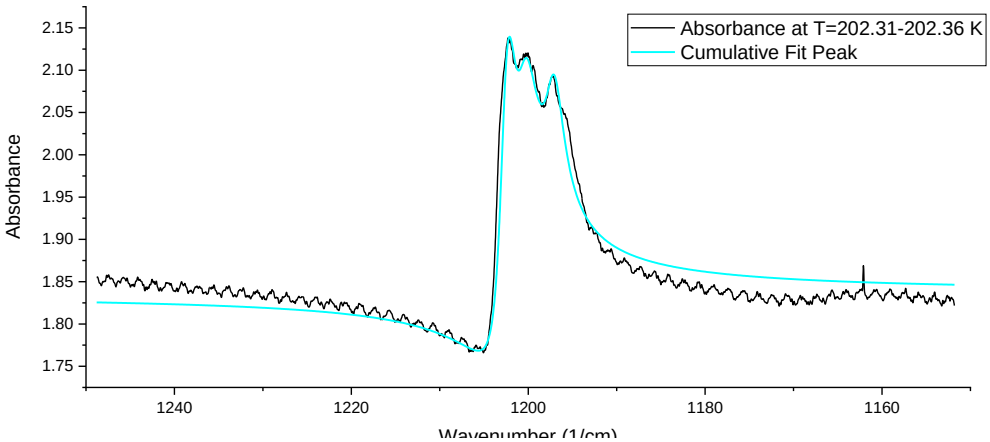
Absorbance at T=202.31-202.36 K
Cumulative Fit Peak
Absorbance
2.15
2.10
2.05
2.00
1.95
1.90
1.85
1.80
1.75
1240
1220
1200
1180
1160

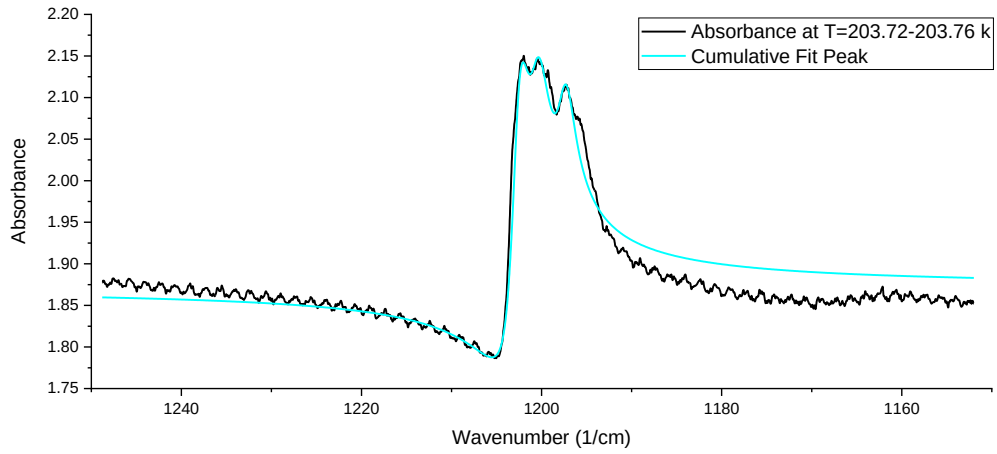

After left the crystal growth all overnight.

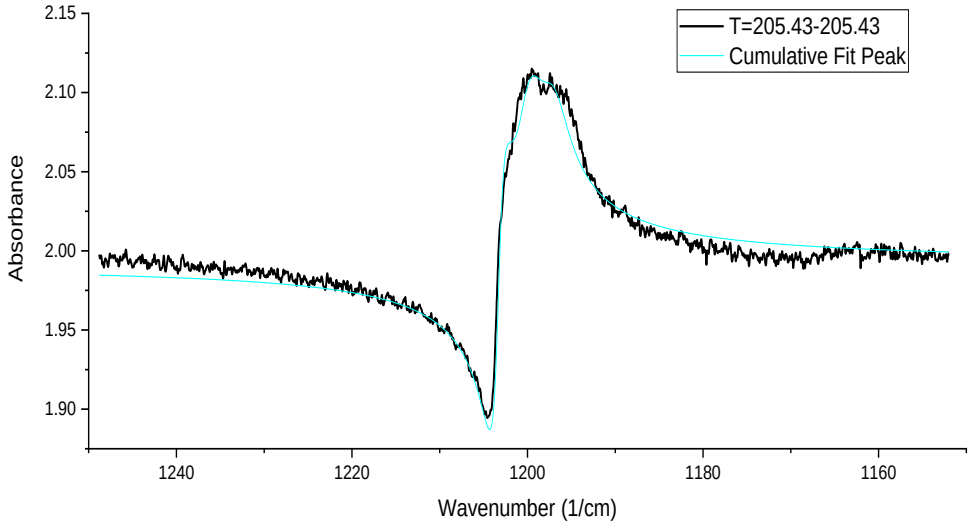

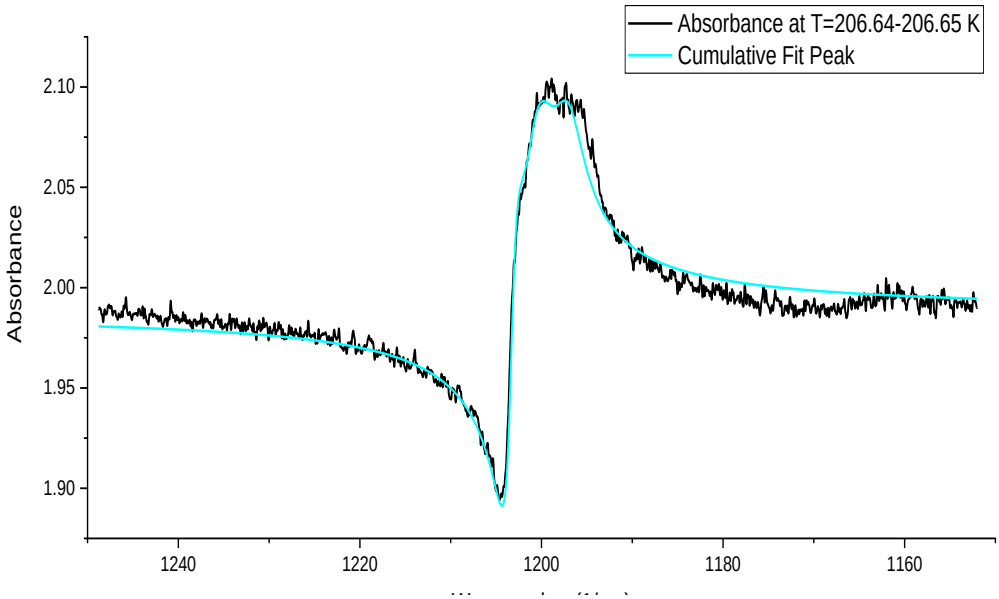
Absorbance at T=206.64-206.65 K
Cumulative Fit Peak
Absorbance
2.10
2.05
2.00
1.95
1.90
1240
1220
1200
1180
1160

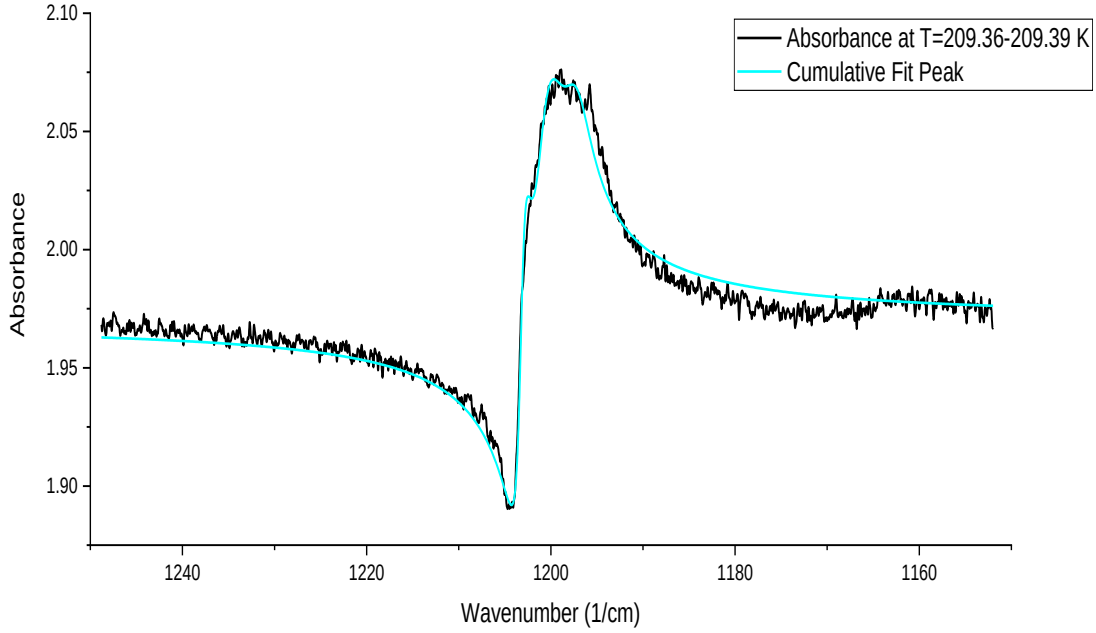
Absorbance at T=209.36-209.39 K
Cumulative Fit Peak
Absorbance
2.10
2.05
2.00
1.95
1.90
1240
1220
1200
1180
1160
Wavenumber (1/cm)

Appendix 2

List of frequencies calculated harmonic frequencies, and intensities for the two-dimensional 19 molecule structure used for modeling the absorption spectrum Harmonic frequencies (cm^{-1}), IR intensities (KM/Mole), reduced masses (AMU), force constants (mDyne/A),

	1	2	3
	BG	AU	AU
Frequencies --	-8.6474	-8.6343	-6.9235
Red. Masses --	18.9538	19.1659	16.0163
Frc consts --	0.0008	0.0008	0.0005
IR Inten --	0.0000	0.0001	0.0001

--

--

	4	5	6
	BG	BG	AU
Frequencies --	-6.8865	-5.4747	-4.9686
Red. Masses --	16.1356	23.2357	15.0927
Frc consts --	0.0005	0.0004	0.0002
IR Inten --	0.0000	0.0000	0.0001

--

--

	7	8	9
	AU	BG	BG
Frequencies --	-4.7868	-4.7658	-4.0645
Red. Masses --	18.4299	16.3065	17.4501
Frc consts --	0.0002	0.0002	0.0002
IR Inten --	0.0000	0.0000	0.0000

--

--

10	11	12

	AU	AU	BG
Frequencies --	-3.8436	-3.4463	-3.3154
Red. Masses --	16.6517	16.1277	16.4454
Frc consts --	0.0001	0.0001	0.0001
IR Inten --	0.0010	0.0007	0.0000

--

--

	13	14	15
	BG	AU	AU
Frequencies --	-3.1510	-3.0433	-2.6367
Red. Masses --	16.3946	16.3601	16.3392
Frc consts --	0.0001	0.0001	0.0001
IR Inten --	0.0000	0.0002	0.0043

--

--

	16	17	18
	BG	AU	BG
Frequencies --	-2.5064	-2.5050	-1.8840
Red. Masses --	16.5440	19.7551	17.3637
Frc consts --	0.0001	0.0001	0.0000
IR Inten --	0.0000	0.0015	0.0000

--

--

	19	20	21
	AU	BG	AU
Frequencies --	-1.4636	-1.1724	0.6615
Red. Masses --	16.6541	21.6845	21.1081
Frc consts --	0.0000	0.0000	0.0000
IR Inten --	0.0005	0.0000	0.0004

--

--

	22	23	24
	BG	AU	BU
Frequencies --	1.9709	2.5445	2.8419
Red. Masses --	19.9772	21.7865	16.4397
Frc consts --	0.0000	0.0001	0.0001
IR Inten --	0.0000	0.0026	0.0085

--

--

	25	26	27
	AU	BG	AG
Frequencies --	3.9014	4.3052	4.5595
Red. Masses --	18.0255	18.5713	16.1553
Frc consts --	0.0002	0.0002	0.0002
IR Inten --	0.0008	0.0000	0.0000

--

--

	28	29	30
	AG	BG	AU
Frequencies --	5.1307	5.2856	5.6975
Red. Masses --	16.2536	24.1068	24.8930
Frc consts --	0.0003	0.0004	0.0005
IR Inten --	0.0000	0.0000	0.0000

--

--

	31	32	33
	AU	BG	BU
Frequencies --	6.4513	6.6585	6.8673
Red. Masses --	23.3266	29.9308	16.5941
Frc consts --	0.0006	0.0008	0.0005

IR Inten --	0.0020	0.0000	0.0591
--			
--			
	34	35	36
	BU	AG	AU
Frequencies --	7.4124	7.4773	7.6357
Red. Masses --	16.5625	16.9093	22.6850
Frc consts --	0.0005	0.0006	0.0008
IR Inten --	0.0400	0.0000	0.0003
--			
--			
	37	38	39
	AG	BG	AU
Frequencies --	8.5979	8.7019	8.9466
Red. Masses --	16.4620	28.0364	29.0248
Frc consts --	0.0007	0.0013	0.0014
IR Inten --	0.0000	0.0000	0.0016
--			
--			
	40	41	42
	BU	BG	AG
Frequencies --	9.2564	9.4280	9.4805
Red. Masses --	16.4809	28.4818	16.8811
Frc consts --	0.0008	0.0015	0.0009
IR Inten --	0.2241	0.0000	0.0000
--			
--			
	43	44	45
	BG	BU	AU
Frequencies --	9.6344	9.6845	10.2983

Red. Masses --	23.5557	16.9340	32.4935
Frc consts --	0.0013	0.0009	0.0020
IR Inten --	0.0000	0.0415	0.0000

--

--

	46	47	48
	BU	AG	AG
Frequencies --	11.0642	13.9040	15.0781
Red. Masses --	16.3884	16.7042	16.4893
Frc consts --	0.0012	0.0019	0.0022
IR Inten --	0.1780	0.0000	0.0000

--

--

	49	50	51
	BU	AG	AG
Frequencies --	15.2137	15.4486	15.8231
Red. Masses --	16.8736	16.8234	16.6415
Frc consts --	0.0023	0.0024	0.0025
IR Inten --	0.0424	0.0000	0.0000

--

--

	52	53	54
	BU	AG	BU
Frequencies --	16.2531	16.8720	17.9175
Red. Masses --	16.4215	17.2565	17.4855
Frc consts --	0.0026	0.0029	0.0033
IR Inten --	0.0017	0.0000	0.0193

--

--

	55	56	57

	BU	AG	BU
Frequencies --	18.3959	19.2706	20.2555
Red. Masses --	16.5713	16.5375	16.8591
Frc consts --	0.0033	0.0036	0.0041
IR Inten --	0.0346	0.0000	0.0321

--

--

	58	59	60
	AG	AG	BU
Frequencies --	20.6550	22.3956	22.5483
Red. Masses --	16.4946	17.0671	16.8131
Frc consts --	0.0041	0.0050	0.0050
IR Inten --	0.0000	0.0000	0.0201

--

--

	61	62	63
	BU	BU	AG
Frequencies --	23.2425	23.8696	25.1752
Red. Masses --	17.9882	16.9064	19.7725
Frc consts --	0.0057	0.0057	0.0074
IR Inten --	0.1029	0.0766	0.0000

--

--

	64	65	66
	BU	AG	BU
Frequencies --	25.8603	26.0480	26.6237
Red. Masses --	19.4093	19.0990	18.4000
Frc consts --	0.0076	0.0076	0.0077
IR Inten --	0.1076	0.0000	0.0315

--

--

	67	68	69
	AG	AG	BU
Frequencies --	27.7393	28.2039	28.2181
Red. Masses --	19.6141	20.0376	19.9902
Frc consts --	0.0089	0.0094	0.0094
IR Inten --	0.0000	0.0000	0.0364

--

--

	70	71	72
	BG	AU	BU
Frequencies --	28.7651	29.1923	30.2069
Red. Masses --	2.1092	2.0582	19.3225
Frc consts --	0.0010	0.0010	0.0104
IR Inten --	0.0000	0.0263	0.0035

--

--

	73	74	75
	AG	BU	AU
Frequencies --	30.6764	31.5893	34.4899
Red. Masses --	19.1270	19.7979	1.9854
Frc consts --	0.0106	0.0116	0.0014
IR Inten --	0.0000	0.0264	0.0494

--

--

	76	77	78
	AG	BU	BG
Frequencies --	34.5702	34.6690	35.0519
Red. Masses --	21.0992	20.8043	1.9776

Frc consts --	0.0149	0.0147	0.0014
IR Inten --	0.0000	0.0183	0.0000

--

--

	79	80	81
	AG	BG	AU
Frequencies --	36.2093	38.1032	38.8008
Red. Masses --	20.7172	1.9639	1.9607
Frc consts --	0.0160	0.0017	0.0017
IR Inten --	0.0000	0.0000	0.0009

--

--

	82	83	84
	AU	BG	BG
Frequencies --	42.2969	42.6655	43.7918
Red. Masses --	1.9598	1.9586	1.9538
Frc consts --	0.0021	0.0021	0.0022
IR Inten --	0.1334	0.0000	0.0000

--

--

	85	86	87
	AU	AG	BU
Frequencies --	44.0242	45.0417	45.1096
Red. Masses --	1.9558	20.4932	20.3936
Frc consts --	0.0022	0.0245	0.0245
IR Inten --	0.2242	0.0000	0.2015

--

--

	88	89	90
	AG	BG	BU

Frequencies --	46.5425	47.4610	47.4734
Red. Masses --	21.7148	1.9594	21.3772
Frc consts --	0.0277	0.0026	0.0284
IR Inten --	0.0000	0.0000	0.0177

--

--

	91	92	93
	AG	BU	AG
Frequencies --	47.9875	48.3949	49.5298
Red. Masses --	21.8701	20.0185	18.8892
Frc consts --	0.0297	0.0276	0.0273
IR Inten --	0.0000	0.0080	0.0000

--

--

	94	95	96
	BU	BU	AG
Frequencies --	49.7896	50.2476	50.2564
Red. Masses --	19.1590	17.5547	17.5339
Frc consts --	0.0280	0.0261	0.0261
IR Inten --	0.0582	0.0523	0.0000

--

--

	97	98	99
	AG	AU	BU
Frequencies --	51.6049	53.7914	54.0381
Red. Masses --	18.0900	1.9579	17.0865
Frc consts --	0.0284	0.0033	0.0294
IR Inten --	0.0000	0.0006	0.0118

--

--

	100	101	102
	AG	BU	AU
Frequencies --	54.2041	54.5686	55.3145
Red. Masses --	17.2102	16.8305	1.9725
Frc consts --	0.0298	0.0295	0.0036
IR Inten --	0.0000	0.0003	0.0007

	103	104	105
	BG	BG	BG
Frequencies --	56.1106	60.1864	60.2940
Red. Masses --	1.9540	1.9807	1.9823
Frc consts --	0.0036	0.0042	0.0042
IR Inten --	0.0000	0.0000	0.0000

	106	107	108
	AU	AU	BG
Frequencies --	60.9296	62.8585	62.9096
Red. Masses --	1.9740	1.9667	1.9662
Frc consts --	0.0043	0.0046	0.0046
IR Inten --	0.0027	0.0060	0.0000

	109	110	111
	AU	BG	BG
Frequencies --	211.1216	211.3665	211.6922
Red. Masses --	8.4463	8.4439	8.4551
Frc consts --	0.2218	0.2223	0.2232
IR Inten --	4.5013	0.0000	0.0000

--

--

	112	113	114
	AU	AU	BG
Frequencies --	211.7327	212.0337	212.1110
Red. Masses --	8.4548	8.4665	8.4674
Frc consts --	0.2233	0.2243	0.2245
IR Inten --	0.0072	0.0809	0.0000

--

--

	115	116	117
	AU	BG	BG
Frequencies --	212.2418	212.3690	212.5127
Red. Masses --	8.4544	8.4856	8.4657
Frc consts --	0.2244	0.2255	0.2253
IR Inten --	0.7259	0.0000	0.0000

--

--

	118	119	120
	AU	AU	BG
Frequencies --	212.5152	212.6086	212.6905
Red. Masses --	8.4759	8.4986	8.4597
Frc consts --	0.2255	0.2263	0.2255
IR Inten --	0.0087	0.0001	0.0000

--

--

	121	122	123
	AU	BG	AU
Frequencies --	212.7162	212.7319	212.8355
Red. Masses --	8.4703	8.4855	8.4782

Frc consts --	0.2258	0.2263	0.2263
IR Inten --	0.0000	0.0000	0.1100

--

--

	124	125	126
	AU	BG	AU
Frequencies --	212.9304	212.9329	212.9653
Red. Masses --	8.4680	8.4788	8.4791
Frc consts --	0.2262	0.2265	0.2266
IR Inten --	0.0976	0.0000	0.1160

--

--

	127	128	129
	BG	BU	AG
Frequencies --	212.9761	237.6839	237.6885
Red. Masses --	8.4742	6.4787	6.4787
Frc consts --	0.2265	0.2156	0.2157
IR Inten --	0.0000	6.5212	0.0000

--

--

	130	131	132
	AG	BU	BU
Frequencies --	237.9125	238.0584	238.0992
Red. Masses --	6.4721	6.4701	6.4525
Frc consts --	0.2158	0.2160	0.2155
IR Inten --	0.0000	0.1053	1.1021

--

--

	133	134	135
	BU	AG	AG

Frequencies --	238.8524	238.8614	238.9859
Red. Masses --	6.4938	6.4835	6.4814
Frc consts --	0.2183	0.2179	0.2181
IR Inten --	9.7330	0.0000	0.0000

--

--

	136	137	138
	AG	BU	BU
Frequencies --	239.2469	239.2472	241.5774
Red. Masses --	6.5074	6.5074	6.4841
Frc consts --	0.2195	0.2195	0.2230
IR Inten --	0.0000	0.0103	3.7603

--

--

	139	140	141
	AG	BU	AG
Frequencies --	242.9058	243.0007	244.3012
Red. Masses --	6.4978	6.4915	6.4895
Frc consts --	0.2259	0.2258	0.2282
IR Inten --	0.0000	3.1859	0.0000

--

--

	142	143	144
	BU	AG	BU
Frequencies --	244.3393	244.6350	246.4438
Red. Masses --	6.4880	6.4987	6.5449
Frc consts --	0.2282	0.2291	0.2342
IR Inten --	37.5339	0.0000	46.4983

--

--

	145	146	147
	AG	BU	AG
Frequencies --	247.0094	247.2275	346.9604
Red. Masses --	6.5122	6.4954	20.0913
Frc consts --	0.2341	0.2339	1.4250
IR Inten --	0.0000	34.6617	0.0000

--

--

	148	149	150
	BU	BU	AG
Frequencies --	346.9954	347.0336	347.0393
Red. Masses --	20.0846	20.1146	20.1312
Frc consts --	1.4248	1.4273	1.4285
IR Inten --	0.0102	0.0070	0.0000

--

--

	151	152	153
	AG	AG	BU
Frequencies --	347.0751	347.0886	347.1091
Red. Masses --	20.1099	20.1225	20.1259
Frc consts --	1.4273	1.4283	1.4287
IR Inten --	0.0000	0.0000	0.0099

--

--

	154	155	156
	AG	BU	AG
Frequencies --	347.1867	347.1872	347.7878
Red. Masses --	20.0478	20.0457	19.9970
Frc consts --	1.4238	1.4236	1.4251
IR Inten --	0.0000	0.0125	0.0000

--

--

	157	158	159
	BU	AG	BU
Frequencies --	347.7879	347.9911	347.9933
Red. Masses --	19.9970	19.9493	19.9502
Frc consts --	1.4251	1.4234	1.4234
IR Inten --	0.1142	0.0000	0.1015

--

--

	160	161	162
	BU	AG	AG
Frequencies --	348.0212	348.0256	348.0600
Red. Masses --	19.9726	19.9751	19.9819
Frc consts --	1.4253	1.4255	1.4263
IR Inten --	0.0803	0.0000	0.0000

--

--

	163	164	165
	BU	BU	AG
Frequencies --	348.0621	348.2584	348.2587
Red. Masses --	19.9838	19.9750	19.9751
Frc consts --	1.4264	1.4274	1.4274
IR Inten --	0.0076	0.0083	0.0000

--

--

	166	167	168
	BG	AU	AU
Frequencies --	780.0494	780.0522	780.8077
Red. Masses --	1.8078	1.8078	1.8053

Frc consts --	0.6481	0.6481	0.6485
IR Inten --	0.0000	0.2343	0.3864

--

--

	169	170	171
	BG	BG	AU
Frequencies --	780.8078	781.0426	781.0508
Red. Masses --	1.8053	1.8034	1.8033
Frc consts --	0.6485	0.6482	0.6482
IR Inten --	0.0000	0.0000	0.5620

--

--

	172	173	174
	AU	BG	AU
Frequencies --	781.3002	781.3005	781.4320
Red. Masses --	1.8033	1.8033	1.8027
Frc consts --	0.6486	0.6486	0.6486
IR Inten --	0.0904	0.0000	0.0456

--

--

	175	176	177
	BG	BG	AU
Frequencies --	781.4321	784.0287	784.5346
Red. Masses --	1.8027	1.7888	1.7875
Frc consts --	0.6486	0.6478	0.6482
IR Inten --	0.0000	0.0000	0.0010

--

--

	178	179	180
	BG	AU	BG

Frequencies --	784.6017	785.1629	785.8452
Red. Masses --	1.7882	1.7845	1.7820
Frc consts --	0.6486	0.6481	0.6484
IR Inten --	0.0000	0.0068	0.0000

--

--

	181	182	183
	AU	BG	AU
Frequencies --	785.8555	785.9167	785.9459
Red. Masses --	1.7821	1.7813	1.7812
Frc consts --	0.6484	0.6483	0.6482
IR Inten --	0.0157	0.0000	0.0153

--

--

	184	185	186
	BG	BU	AG
Frequencies --	785.9467	798.9587	800.3586
Red. Masses --	1.7812	10.0523	10.1417
Frc consts --	0.6482	3.7806	3.8276
IR Inten --	0.0000	1142.0956	0.0000

--

--

	187	188	189
	AG	BU	BU
Frequencies --	801.5675	802.2669	802.6283
Red. Masses --	10.0424	10.1704	10.1955
Frc consts --	3.8016	3.8568	3.8698
IR Inten --	0.0000	213.3484	3.5003

--

--

	190	191	192
	BU	AG	AG
Frequencies --	803.4348	803.6541	804.3392
Red. Masses --	10.0986	10.1034	10.0759
Frc consts --	3.8407	3.8446	3.8407
IR Inten --	22.0724	0.0000	0.0000

--

--

	193	194	195
	BU	AG	BU
Frequencies --	804.5299	804.7423	805.1776
Red. Masses --	10.0304	10.0382	9.9883
Frc consts --	3.8252	3.8302	3.8153
IR Inten --	354.4965	0.0000	128.6154

--

--

	196	197	198
	BU	AG	AG
Frequencies --	805.3334	805.4049	806.4841
Red. Masses --	9.9409	9.9046	9.8224
Frc consts --	3.7986	3.7854	3.7641
IR Inten --	99.4897	0.0000	0.0000

--

--

	199	200	201
	BU	AG	BU
Frequencies --	806.7301	807.4750	807.5712
Red. Masses --	9.7977	9.7913	9.7902
Frc consts --	3.7569	3.7614	3.7619
IR Inten --	334.3773	0.0000	61.1130

--

--

	202	203	204
	BU	AG	AG
Frequencies --	808.1775	808.5606	836.4082
Red. Masses --	9.7915	9.7723	4.7584
Frc consts --	3.7680	3.7642	1.9613
IR Inten --	630.7280	0.0000	0.0000

--

--

	205	206	207
	BU	AG	BU
Frequencies --	837.0002	837.1065	837.9938
Red. Masses --	4.7492	4.7638	4.7278
Frc consts --	1.9603	1.9668	1.9561
IR Inten --	0.1101	0.0000	0.9359

--

--

	208	209	210
	AG	BU	AG
Frequencies --	838.0028	838.1407	839.2526
Red. Masses --	4.7298	4.7095	4.6755
Frc consts --	1.9570	1.9492	1.9403
IR Inten --	0.0000	1.6940	0.0000

--

--

	211	212	213
	BU	AG	BU
Frequencies --	839.3504	840.0303	840.8024
Red. Masses --	4.6911	4.6429	4.6211

Frc consts --	1.9472	1.9303	1.9248
IR Inten --	4.0088	0.0000	6.2697

--

--

	214	215	216
	AG	BU	AG
Frequencies --	840.8084	841.1504	841.2458
Red. Masses --	4.6225	4.6089	4.6178
Frc consts --	1.9254	1.9213	1.9254
IR Inten --	0.0000	1.2131	0.0000

--

--

	217	218	219
	BU	AG	AG
Frequencies --	841.3332	841.8880	841.9547
Red. Masses --	4.5956	4.5952	4.6030
Frc consts --	1.9166	1.9190	1.9225
IR Inten --	2.3102	0.0000	0.0000

--

--

	220	221	222
	BU	BU	AG
Frequencies --	841.9680	842.0856	842.0878
Red. Masses --	4.5988	4.5775	4.5791
Frc consts --	1.9208	1.9125	1.9131
IR Inten --	2.1312	0.0864	0.0000

--

--

	223	224	225
	BG	AU	BG

Frequencies --	925.3659	925.3683	926.0383
Red. Masses --	1.0827	1.0827	1.0825
Frc consts --	0.5462	0.5462	0.5470
IR Inten --	0.0000	10.0481	0.0000

--

--

	226	227	228
	AU	AU	BG
Frequencies --	926.0484	926.5072	926.5923
Red. Masses --	1.0826	1.0827	1.0827
Frc consts --	0.5470	0.5476	0.5477
IR Inten --	1.4872	65.7193	0.0000

--

--

	229	230	231
	BG	AU	BG
Frequencies --	926.6153	926.6921	927.0801
Red. Masses --	1.0828	1.0828	1.0827
Frc consts --	0.5478	0.5479	0.5483
IR Inten --	0.0000	1.1202	0.0000

--

--

	232	233	234
	AU	AU	BG
Frequencies --	927.0963	930.2575	930.6138
Red. Masses --	1.0827	1.0823	1.0822
Frc consts --	0.5483	0.5518	0.5522
IR Inten --	198.8558	12.0041	0.0000

--

--

	235	236	237
	AU	AU	BG
Frequencies --	930.8361	931.4705	931.8279
Red. Masses --	1.0824	1.0823	1.0827
Frc consts --	0.5526	0.5532	0.5539
IR Inten --	0.0348	0.0932	0.0000

--

--

	238	239	240
	BG	AU	BG
Frequencies --	932.0289	932.8378	933.3941
Red. Masses --	1.0824	1.0824	1.0825
Frc consts --	0.5540	0.5549	0.5557
IR Inten --	0.0000	0.2719	0.0000

--

--

	241	242	243
	AU	BU	AG
Frequencies --	934.0003	1191.7740	1191.7874
Red. Masses --	1.0829	1.0999	1.0999
Frc consts --	0.5566	0.9204	0.9205
IR Inten --	572.9144	0.2282	0.0000

--

--

	244	245	246
	AG	BU	BU
Frequencies --	1192.7195	1192.7826	1192.9718
Red. Masses --	1.0992	1.0996	1.0996
Frc consts --	0.9213	0.9218	0.9221
IR Inten --	0.0000	10.3322	0.4206

--

--

	247	248	249
	AG	BU	AG
Frequencies --	1192.9901	1193.5286	1193.5900
Red. Masses --	1.0999	1.0991	1.0993
Frc consts --	0.9223	0.9225	0.9227
IR Inten --	0.0000	59.3838	0.0000

--

--

	250	251	252
	BU	AG	BU
Frequencies --	1194.5296	1194.5973	1195.2142
Red. Masses --	1.0987	1.0990	1.1004
Frc consts --	0.9237	0.9240	0.9261
IR Inten --	44.7347	0.0000	50.5101

--

--

	253	254	255
	AG	AG	BU
Frequencies --	1195.2622	1196.7186	1197.1854
Red. Masses --	1.1005	1.0966	1.0968
Frc consts --	0.9263	0.9253	0.9262
IR Inten --	0.0000	0.0000	2.8795

--

--

	256	257	258
	BU	BU	AG
Frequencies --	1197.5242	1198.2650	1199.1278
Red. Masses --	1.0964	1.0987	1.0999

Frc consts --	0.9263	0.9295	0.9318
IR Inten --	37.0033	24.1824	0.0000

--

--

	259	260	261
	AG	BU	AG
Frequencies --	1199.4496	1200.9224	1275.0832
Red. Masses --	1.0974	1.0998	1.1659
Frc consts --	0.9302	0.9345	1.1168
IR Inten --	0.0000	189.3851	0.0000

--

--

	262	263	264
	BU	BU	AG
Frequencies --	1275.1117	1275.2570	1275.3046
Red. Masses --	1.1659	1.1713	1.1714
Frc consts --	1.1169	1.1223	1.1225
IR Inten --	0.6646	0.2955	0.0000

--

--

	265	266	267
	AG	BU	AG
Frequencies --	1276.2619	1276.4016	1276.4493
Red. Masses --	1.1735	1.1741	1.1667
Frc consts --	1.1262	1.1270	1.1200
IR Inten --	0.0000	4.1585	0.0000

--

--

	268	269	270
	BU	BU	AG

Frequencies --	1276.5819	1276.9348	1276.9894
Red. Masses --	1.1688	1.1723	1.1701
Frc consts --	1.1222	1.1262	1.1243
IR Inten --	0.9055	0.7111	0.0000

--

--

	271	272	273
	AG	BU	BU
Frequencies --	1277.0469	1277.2952	1277.8487
Red. Masses --	1.1757	1.1718	1.1728
Frc consts --	1.1297	1.1264	1.1283
IR Inten --	0.0000	8.0147	1.9490

--

--

	274	275	276
	AG	BU	AG
Frequencies --	1277.8726	1278.3916	1278.4699
Red. Masses --	1.1679	1.1732	1.1706
Frc consts --	1.1237	1.1297	1.1273
IR Inten --	0.0000	4.6810	0.0000

--

--

	277	278	279
	AG	BU	AG
Frequencies --	1278.9383	1279.7623	1279.9142
Red. Masses --	1.1735	1.1712	1.1723
Frc consts --	1.1309	1.1301	1.1315
IR Inten --	0.0000	0.0014	0.0000

--

--

	280	281	282
	BU	AG	AG
Frequencies --	1656.5195	1656.5205	1656.8276
Red. Masses --	7.1755	7.1755	7.1771
Frc consts --	11.6011	11.6010	11.6079
IR Inten --	0.4239	0.0000	0.0000

--

--

	283	284	285
	BU	AG	BU
Frequencies --	1656.8277	1656.9302	1656.9312
Red. Masses --	7.1771	7.1829	7.1823
Frc consts --	11.6079	11.6187	11.6178
IR Inten --	1.0127	0.0000	0.3291

--

--

	286	287	288
	BU	AG	AG
Frequencies --	1657.2297	1657.2446	1657.3223
Red. Masses --	7.1775	7.1749	7.1691
Frc consts --	11.6142	11.6102	11.6020
IR Inten --	0.0644	0.0000	0.0000

--

--

	289	290	291
	BU	AG	BU
Frequencies --	1657.3465	1658.0146	1658.0680
Red. Masses --	7.1654	7.1574	7.1440
Frc consts --	11.5962	11.5926	11.5717
IR Inten --	0.1484	0.0000	0.0019

--

--

	292	293	294
	AG	BU	AG
Frequencies --	1658.1476	1658.2103	1658.2562
Red. Masses --	7.1307	7.1195	7.1219
Frc consts --	11.5513	11.5339	11.5384
IR Inten --	0.0000	0.0474	0.0000

--

--

	295	296	297
	BU	AG	BU
Frequencies --	1658.6406	1658.7501	1658.8144
Red. Masses --	7.1200	7.1017	7.0949
Frc consts --	11.5408	11.5126	11.5025
IR Inten --	0.0188	0.0000	0.0016

--

--

	298	299	300
	AG	AG	BU
Frequencies --	1659.0983	3224.6074	3224.6084
Red. Masses --	7.0873	1.0874	1.0874
Frc consts --	11.4940	6.6616	6.6616
IR Inten --	0.0000	0.0000	55.5655

--

--

	301	302	303
	AG	BU	BU
Frequencies --	3224.7325	3224.7383	3225.7947
Red. Masses --	1.0872	1.0872	1.0870

Frc consts --	6.6612	6.6613	6.6646
IR Inten --	0.0000	64.3082	39.5936

--

--

	304	305	306
	AG	BU	AG
Frequencies --	3225.8001	3226.0017	3226.0024
Red. Masses --	1.0871	1.0868	1.0869
Frc consts --	6.6647	6.6641	6.6644
IR Inten --	0.0000	94.8913	0.0000

--

--

	307	308	309
	BU	AG	BU
Frequencies --	3226.1950	3226.4462	3226.5389
Red. Masses --	1.0865	1.0871	1.0877
Frc consts --	6.6626	6.6674	6.6719
IR Inten --	259.2526	0.0000	37.3384

--

--

	310	311	312
	AG	BU	AG
Frequencies --	3226.5597	3226.7717	3227.3436
Red. Masses --	1.0879	1.0874	1.0873
Frc consts --	6.6730	6.6707	6.6728
IR Inten --	0.0000	30.4023	0.0000

--

--

	313	314	315
	BU	AG	BU

Frequencies --	3227.3481	3227.4288	3227.8187
Red. Masses --	1.0873	1.0870	1.0874
Frc consts --	6.6728	6.6710	6.6750
IR Inten --	61.5554	0.0000	70.1812

--

--

	316	317	318
	AG	BU	BU
Frequencies --	3227.8548	3227.9845	3230.6606
Red. Masses --	1.0873	1.0865	1.1031
Frc consts --	6.6749	6.6702	6.7833
IR Inten --	0.0000	0.8855	10.2485

--

--

	319	320	321
	AG	AG	BU
Frequencies --	3230.6612	3230.8135	3230.8135
Red. Masses --	1.1031	1.1028	1.1028
Frc consts --	6.7834	6.7825	6.7825
IR Inten --	0.0000	0.0000	2.7493

--

--

	322	323	324
	BU	AG	AG
Frequencies --	3231.5454	3231.5455	3232.3024
Red. Masses --	1.1037	1.1037	1.1041
Frc consts --	6.7911	6.7911	6.7964
IR Inten --	11.3317	0.0000	0.0000

--

--

	325	326	327
	BU	AG	BU
Frequencies --	3232.3561	3232.4330	3232.4371
Red. Masses --	1.1036	1.1033	1.1033
Frc consts --	6.7939	6.7920	6.7920
IR Inten --	16.2101	0.0000	0.9672

--

--

	328	329	330
	AG	BU	AG
Frequencies --	3232.6305	3232.8130	3232.8176
Red. Masses --	1.1046	1.1034	1.1034
Frc consts --	6.8010	6.7943	6.7943
IR Inten --	0.0000	21.3551	0.0000

--

--

	331	332	333
	BU	AG	BU
Frequencies --	3233.1053	3233.1055	3233.1508
Red. Masses --	1.1050	1.1050	1.1047
Frc consts --	6.8055	6.8055	6.8037
IR Inten --	0.5191	0.0000	0.3344

--

--

	334	335	336
	AG	BU	AG
Frequencies --	3233.2307	3233.6292	3233.6335
Red. Masses --	1.1051	1.1050	1.1050
Frc consts --	6.8068	6.8076	6.8076
IR Inten --	0.0000	3.2836	0.0000

Appendix 3

Trans -1, 2-dichloroethylene Calculated Infrared Energies and Intensities for Isolated Gas Phase Molecules

Anharmonic Infrared Spectroscopy

Units: Energies (E) in cm^{-1}

Integrated intensity (I) in $km.mol^{-1}$

Fundamental Bands				
Mode (Quant)	E(harm)	E(anharm)	I(harm)	I(anharm)
1(1)	3260.358	3108.024	0.00000000	0.00005992
2(1)	3257.554	3128.985	16.98454678	14.15047954
3(1)	1636.542	1589.872	0.00000000	0.00003183
4(1)	1300.803	1277.144	0.00000000	0.00000641
5(1)	1220.735	1193.541	20.22245069	18.02189905
6(1)	934.442	912.987	54.44220429	54.20469141
7(1)	878.513	865.617	0.00000000	0.00000036
8(1)	861.816	846.878	110.16920943	112.10902631
9(1)	787.356	775.611	0.00000000	0.00001251
10(1)	359.872	355.892	0.00000000	0.00000072
11(1)	239.139	240.687	3.35671331	3.36349744
12(1)	217.690	217.307	0.20918182	0.22860134

Overtones			
Mode (Qunta)	E(harm)	E(anharm)	I(anharm)
1(2)	6520.717	6171.471	0.00000000
2(2)	6515.109	6227.508	0.00000000
3(2)	3273.084	3182.303	0.00000000
4(2)	2601.605	2550.816	0.00000000
5(2)	2441.469	2395.548	0.00000000
6(2)	1868.883	1819.451	0.00000000
7(2)	1757.026	1734.234	0.00000000
8(2)	1723.632	1691.436	0.00000000
9(2)	1574.712	1554.339	0.00000000
10(2)	719.745	711.400	0.00000000
11(2)	478.277	482.000	0.00000000
12(2)	435.380	435.551	0.00000000

Combination Bands			
Mode(Quanta)	E(harm)	E(anharm)	I(anharm)
2(1) 1(1)	6517.913	6143.420	1.51458081
3(1) 1(1)	4896.900	4719.181	0.00000000
3(1) 2(1)	4894.096	4723.135	0.11428644
4(1) 1(1)	4561.161	4395.252	0.00000000

4(1)	2(1)	4558.357	4394.826	1.04326485
4(1)	3(1)	2937.345	2855.651	0.00000000
5(1)	1(1)	4481.093	4317.370	0.50693576
5(1)	2(1)	4478.289	4322.939	0.00000000
5(1)	3(1)	2857.277	2779.383	0.49456295
5(1)	4(1)	2521.537	2468.319	0.56815330
6(1)	1(1)	4194.800	4031.878	0.08231380
6(1)	2(1)	4191.996	4032.838	0.00000000
6(1)	3(1)	2570.984	2496.870	0.00070249
6(1)	4(1)	2235.244	2190.462	0.00535836
6(1)	5(1)	2155.176	2113.872	0.00000000
7(1)	1(1)	4138.872	3991.597	0.00000000
7(1)	2(1)	4136.068	3992.791	1.01452595
7(1)	3(1)	2515.055	2439.666	0.00000000
7(1)	4(1)	2179.316	2142.075	0.00000000
7(1)	5(1)	2099.248	2064.959	0.06010448
7(1)	6(1)	1812.955	1778.119	0.00363745
8(1)	1(1)	4122.175	3975.702	0.01453676
8(1)	2(1)	4119.371	3976.777	0.00000000
8(1)	3(1)	2498.358	2429.573	0.08347288
8(1)	4(1)	2162.619	2122.027	0.39609145
8(1)	5(1)	2082.551	2044.013	0.00000000
8(1)	6(1)	1796.258	1758.517	0.00000000
8(1)	7(1)	1740.329	1705.745	0.32677560
9(1)	1(1)	4047.714	3895.030	0.00000000
9(1)	2(1)	4044.910	3897.485	0.02593723
9(1)	3(1)	2423.898	2356.930	0.00000000
9(1)	4(1)	2088.159	2053.245	0.00000000
9(1)	5(1)	2008.091	1978.327	0.00558917
9(1)	6(1)	1721.798	1683.343	6.53701471
9(1)	7(1)	1665.869	1640.502	0.00000000
9(1)	8(1)	1649.172	1620.572	0.00014611
10(1)	1(1)	3620.231	3483.860	0.00000000
10(1)	2(1)	3617.427	3485.073	0.03102451
10(1)	3(1)	1996.414	1942.779	0.00000000
10(1)	4(1)	1660.675	1634.250	0.00000000
10(1)	5(1)	1580.607	1555.651	0.02775529
10(1)	6(1)	1294.314	1268.690	0.00811053
10(1)	7(1)	1238.386	1220.465	0.00000000
10(1)	8(1)	1221.689	1206.933	0.76608819
10(1)	9(1)	1147.228	1131.266	0.00000000
11(1)	1(1)	3499.497	3368.384	0.00685107
11(1)	2(1)	3496.693	3369.677	0.00000000
11(1)	3(1)	1875.681	1829.303	0.28007836
11(1)	4(1)	1539.941	1518.713	0.01777126
11(1)	5(1)	1459.873	1442.654	0.00000000
11(1)	6(1)	1173.580	1153.801	0.00000000
11(1)	7(1)	1117.652	1104.988	0.24283464
11(1)	8(1)	1100.955	1085.579	0.00000000
11(1)	9(1)	1026.495	1016.216	0.04174285
11(1)	10(1)	599.011	596.836	0.01139981
12(1)	1(1)	3478.049	3344.814	0.01500374
12(1)	2(1)	3475.245	3346.078	0.00000000
12(1)	3(1)	1854.232	1805.939	0.16989927
12(1)	4(1)	1518.493	1494.921	0.02133926

12(1) 5(1)	1438.425	1417.423	0.00000000
12(1) 6(1)	1152.132	1130.284	0.00000000
12(1) 7(1)	1096.203	1082.146	0.14875057
12(1) 8(1)	1079.506	1063.154	0.00000000
12(1) 9(1)	1005.046	992.136	0.82404171
12(1) 10(1)	577.562	570.980	0.00320160
12(1) 11(1)	456.829	461.226	0.00000000

Table 16: Calculated Anharmonic IR frequencies for trans -1, 2-dichloroethylene in gas phase.

Appendix 4

Corrected calculated Energy by scaling factor with IR intensity and experiment in solid phases at 120 K with their intensities as integrated Area.

Units: Energies (E) in cm^{-1}

Integrated intensity (I) in $km.mol^{-1}$

Treat Calculated	IR intensity	Experiment (120 K +Ar)	Area	The difference between Calculated &observed
6101.34	1.51458081	6045.918	0.443	55.42222085
4686.86	0	4650.987	0.1745	35.86964414
4690.78	0.11428644	4658.87981	0.2603	31.90375095
4365.15	0	4321.6	0.08	43.54641818
4364.72	1.04326485	4337.23253	1.489	27.4908061
4287.8	0.50693576	4254.734	0.53795	33.06387631
4293.33	0	4230.84	0.071	62.48873106
4004.26	0.0823138	4031.315	0.088	-27.05362654
4005.21	0	4030.332	0.037	-25.11720212
3964.26	0	3957.654	0.008	6.602280951
3965.44	1.01452595	3958.514	0.28346	6.928102566
3948.47	0.01453676	3921.903	0.682	26.56715485
3949.54	0	3922.987	0.01265	26.55079156
3868.35	0	3890.086	0.0324	-21.73527672
3870.79	0.02593723	3891.363	0.11575	-20.57409241
3460	0	3437.572	0.1503	22.42506056
3461.2	0.03102451	3437.759	0.15665	23.44275204
3345.31	0.00685107	3385.313	0.13749	-40.00097861
3346.6	0	3333.983	0.0123	12.6131649
3321.9	0.01500374	3322.094	0.27516	-0.190534266
3323.16	0	3326.074	0.112	-2.915192121
2836.09	0	2885.11	0.115	-49.01897855
2760.35	0.49456295	2762.649	0.41853	-2.30357562
2479.77	0.00070249	2554.81	0.043	-75.04248333
2451.41	0.5681533	2455.656	0.33484	-4.24392129
2422.96	0	2433.432	0.0122	-10.47666059
2412.93	0.08347288	2428.989	0.05822	-16.05752789
2340.79	0	2359.94	0.0232	-19.15395465
2175.46	0.00535836	2167.467	0.055	7.991279402
2127.4	0	2122.023	0.0134	5.379709497
2107.49	0.39609145	2076.872	0.41548	30.62002966
2099.39	0	2070.34	0.0121	29.05288789
2050.81	0.06010448	2040.743	0.1084	10.07192086
2039.18	0	2030.875	0.0023	8.306156711
2030.01	0	2022.864	0.0032	7.148391931
1964.78	0.00558917	1963.106	0.02859	1.67031272
1929.47	0	1930.876	0.0112	-1.404198801

1816.77	0.28007836	1819.312	0.24499	-2.53893711
1793.57	0.16989927	1801.308	0.1985	-7.73890378
1765.94	0.00363745	1799.952	0.18798	-34.01234877
1746.47	0	1778.87	0.0123	-32.39808352
1694.06	0.3267756	1704.416	0.74668	-10.35461806
1671.81	6.53701471	1658.072	5.65677	13.74082598
1629.27	0	1639.876	0.0012	-10.61073163
1623.06	0	1629.465	0.0012	-6.408908129
1609.47	0.00014611	1619.381	0.12056	-9.909219724
1545	0.02775529	1552.547	0.12665	-7.551538855
1508.31	0.01777126	1516.628	0.08039	-8.317529476
1484.68	0.02133926	1493.743	0.03245	-9.06156453
1432.77	0	1440.876	0.0209	-8.103558108
1407.71	0	1416.8765	0.0234	-9.162236632
1260	0.00811053	1260.072	0.05406	-0.071979687
1212.11	0	1210.086	0.0526	2.019340778
1198.67	0.76608819	1204.438	0.74306	-5.771970855
1145.9	0	1162.23513	0.511	-16.33716956
1122.54	0	1140.986	0.023	-18.44395824
1123.52	0	1141.986	0.0123	-18.46868452
1097.42	0.24283464	1092.12	0.136	5.299308456
1078.14	0	1079.91	0.0122	-1.766748259
1074.73	0.14875057	1070.317	0.16181	4.416766311
1055.87	0	1050.432	0.0032	5.439853326
1009.26	0.04174285	1018.684	0.09977	-9.428641605
985.34	0.82404171	989.6663	0.42452	-4.326003984
592.748	0.01139981	-	-	-
567.069	0.0032016	-	-	-
458.067	0	-	-	-

Table 17: Corrected calculated frequencies by scaling factor and experiment values both in solid phases.

Overtones Observed frequencies	Calculation	Corrected
6156.43	6171.471	6135.563598
6173.82	6227.508	6191.274559
3139.566	3182.303	3163.787441
2521.822	2550.816	2535.974615
2400.66	2395.548	2381.610009
1805.1048	1819.451	1808.864908
1743.1818	1734.234	1724.143725
1676.3024	1691.436	1681.594737
1551.222	1554.339	1545.295407
711.784	711.4	707.2608692
481.374	482	479.1955847
434.614	435.551	433.0168384

Table 18: The overtones for observed frequencies, calculated anharmonic energies and the corrected frequencie